

WHIRLING RESPONSE AND
STABILITY OF FLEXIBLY MOUNTED,
RING-TYPE FLYWHEEL SYSTEMS.

CHEN, LIANG-CHU TIMOTHY
DEGREE DATE: 1978

University
Microfilms
International

19960220 144

DISTRIBUTION STATEMENT A

Approved for public release
Distribution Unlimited

PLASTEC 33703

DISCLAIMER NOTICE



**THIS DOCUMENT IS BEST
QUALITY AVAILABLE. THE
COPY FURNISHED TO DTIC
CONTAINED A SIGNIFICANT
NUMBER OF PAGES WHICH DO
NOT REPRODUCE LEGIBLY.**

Date: 9/9/95 Time: 3:26:40PM

Page: 1 Document Name: untitled

DTIC DOES NOT HAVE THIS ITEM

-- 1 - AD NUMBER: D428577
-- 5 - CORPORATE AUTHOR: OKLAHOMA UNIV NORMAN SCHOOL OF AEROSPACE
-- MECHANICAL AND NUCLEAR ENGINEERING
-- 6 - UNCLASSIFIED TITLE: WHIRLING RESPONSE AND STABILITY OF FLEXIBLY
-- MOUNTED, RING-TYPE FLYWHEEL SYSTEMS.
--10 - PERSONAL AUTHORS: CHEN, T. L. C.; BERT, C. W.;
--11 - REPORT DATE: NOV , 1978
--12 - PAGINATION: 122P
--14 - REPORT NUMBER: RR-OU-AMNE-78-6
--15 - CONTRACT NUMBER: EY-76-C-04-0789
--18 - MONITOR ACRONYM: SAND
--19 - MONITOR SERIES: 78-7073
--20 - REPORT CLASSIFICATION: UNCLASSIFIED
--21 - SUPPLEMENTARY NOTE: ALSO AVAILABLE AS UNIVERSITY MICROFILMS
-- INTERNATIONAL DISSERTATION, ORDER NO. 7908816.
--22 - LIMITATIONS (ALPHA): APPROVED FOR PUBLIC RELEASE; DISTRIBUTION
-- UNLIMITED. AVAILABILITY: NATIONAL TECHNICAL INFORMATION SERVICE,
-- SPRINGFIELD, VA. 22161. SAND-78-7073.
--33 - LIMITATION CODES: 1 24

Went
BOOK REPRINT RECD FROM TRACOR

DATE RECD: 2/6/80

PER YOUR ORDER: DS

Joe - Please return to Marie
COMMENTS: for correction
of field 45.
DS

A NOTE ABOUT THE REPRODUCTION OF ILLUSTRATIONS

Dear Customer:

The enclosed book was printed by xerography, an advanced printing technology allowing the production of a single copy or as many copies as required, on demand.

The xerographic process was developed primarily to reproduce all-line copy, i.e. the average printed page containing text and diagrams or simple line drawings.

Some halftone illustrations reproduce well by xerography but many do not. If your book contains halftone illustrations, the clarity of which is vital to the book's usefulness, photographic reproductions (silverprints) of such pages are available at the cost of \$1.50 per page (with a minimum of \$6.00 per order.)

The bottom of this sheet is an order form on which you may order the silverprints you require. Please be sure to fill in all of the information called for so your order can be processed without delay. All orders for silverprints must be accompanied by a check or money order covering full payment.

----- TEAR ALONG DOTTED LINE -----

Send order and payment to: Silverprint—Order Entry
University Microfilms International
300 North Zeeb Road, Ann Arbor, MI 48106 USA
18 Bedford Row, London WC1R 4EJ, England

Date _____

Book Order Number _____

Total number of pages ordered _____

Author _____

\$1.50 per page = total _____

Title _____

Plus State & Local Taxes _____

Or if tax exempt enter your tax exemption number here _____

Provide silverprints for the following page numbers:

TOTAL AMOUNT ENCLOSED _____

_____ ; _____ ; _____ ; _____ ; _____ ;

_____ ; _____ ; _____ ; _____ ; _____ ;

_____ ; _____ ; _____ ; _____ ; _____ ;

Your telephone number should we need to contact you regarding your order

Please complete the address label below.

Do not write in this space

SHIP TO: Name _____

Address _____

_____ ZIP _____

**This is an authorized facsimile
and was produced by microfilm-xerography
in 1980 by
UNIVERSITY MICROFILMS INTERNATIONAL
Ann Arbor, Michigan, U.S.A.
London, England**

INFORMATION TO USERS

This was produced from a copy of a document sent to us for microfilming. While the most advanced technological means to photograph and reproduce this document have been used, the quality is heavily dependent upon the quality of the material submitted.

The following explanation of techniques is provided to help you understand markings or notations which may appear on this reproduction.

1. The sign or "target" for pages apparently lacking from the document photographed is "Missing Page(s)". If it was possible to obtain the missing page(s) or section, they are spliced into the film along with adjacent pages. This may have necessitated cutting through an image and duplicating adjacent pages to assure you of complete continuity.
2. When an image on the film is obliterated with a round black mark it is an indication that the film inspector noticed either blurred copy because of movement during exposure, or duplicate copy. Unless we meant to delete copyrighted materials that should not have been filmed, you will find a good image of the page in the adjacent frame.
3. When a map, drawing or chart, etc., is part of the material being photographed the photographer has followed a definite method in "sectioning" the material. It is customary to begin filming at the upper left hand corner of a large sheet and to continue from left to right in equal sections with small overlaps. If necessary, sectioning is continued again—beginning below the first row and continuing on until complete.
4. For any illustrations that cannot be reproduced satisfactorily by xerography, photographic prints can be purchased at additional cost and tipped into your xerographic copy. Requests can be made to our Dissertations Customer Services Department.
5. Some pages in any document may have indistinct print. In all cases we have filmed the best available copy.

University
Microfilms
International

300 N. ZEEB ROAD, ANN ARBOR, MI 48106
18 BEDFORD ROW, LONDON WC1R 4EJ, ENGLAND

7908816

CHEN, LIANG-CHU TIMOTHY
WHIRLING RESPONSE AND STABILITY OF FLEXIBLY
MOUNTED, RING-TYPE FLYWHEEL SYSTEMS.

THE UNIVERSITY OF OKLAHOMA, PH.D., 1978

University
Microfilms
International

300 N. ZEEB ROAD, ANN ARBOR, MI 48106

THE UNIVERSITY OF OKLAHOMA
GRADUATE COLLEGE

WHIRLING RESPONSE AND STABILITY OF FLEXIBLY
MOUNTED, RING-TYPE FLYWHEEL SYSTEMS

A DISSERTATION
SUBMITTED TO THE GRADUATE FACULTY
in partial fulfillment of the requirements for the
degree of
DOCTOR OF PHILOSOPHY

By
LIANG-CHU TIMOTHY CHEN
Norman, Oklahoma

1978

WHIRLING RESPONSE AND STABILITY OF FLEXIBLY
MOUNTED, RING-TYPE FLYWHEEL SYSTEMS

Approved By

Charles W. Bert

J. Narasimha Reddy

Daniel M. Egle

Franklin J. Cypert

William A. Huff

DISSERTATION COMMITTEE

ACKNOWLEDGMENTS

The author is indebted to his adviser, Dr. Charles W. Bert, for his guidance and suggestions throughout this work. The inspiration, encouragement, and foundation provided by Professor Bert are sincerely appreciated.

The author also wishes to express his sincere thanks to Dr. F. J. Appl, Dr. D. M. Egle, Dr. W. N. Huff, and Dr. J. N. Reddy for their valuable time and constructive comments.

Helpful assistance and comments provided by Chris Kocay are also acknowledged.

The support of the Department of Energy through a contract from Sandia Laboratories, Albuquerque, New Mexico, is acknowledged.

Appreciation for the understanding and patience of his wife, Mei-Ling, can hardly be expressed.

ABSTRACT

The scarcity and rising cost of petroleum have motivated international interest in developing hybrid automobiles using flywheels for mechanical energy storage. Rim-type composite-material flywheels are promising designs for such developments. These flywheels significantly differ from turbine/compressor systems in two respects. First, the flywheel rim attachment to its hub is very flexible, for both translation and tilting. Secondly, these flexibilities depend upon rotational speed through centrifugal stiffening. In this investigation, free whirling, stability, and forced whirling are examined for these flywheel systems. The numerical results presented here are most directly applicable to the Sandia single-rim systems currently under development. However, the present analyses can be extended to other flywheel designs within the broad category of the rim type.

In the free-whirling analysis, predicted critical speeds are encountered in the design operating speed range. Practical ways to increase such critical speeds are suggested.

Effects of material internal damping on the stability of the system are incorporated through adopting complex moduli in the formulation. It is found that the adverse effect of internal damping on the onset of instability can be overcome by providing an adequate external damper up to a considerably high speed.

Forced whirling excited by unbalance and initial tilt of rim element is studied. Minimum external damping is determined such that the maximum response does not exceed a permissible value.

TABLE OF CONTENTS

	Page
ACKNOWLEDGMENTS	iii
ABSTRACT	iv
LIST OF TABLES	vii
LIST OF FIGURES	viii
NOMENCLATURE	x
Chapter	
I. INTRODUCTION	1
1.1 Historical Background	1
1.2 Description of the Sandia Band-Supported, Rim-Type Flywheel	3
1.3 General Hypotheses	5
II. FREE WHIRLING OF THE UNDAMPED SYSTEM	10
2.1 The Gyroscopic Action of a Rotor	10
2.2 Formulation of the Equations of Motion for the Undamped Flywheel System	11
2.3 Numerical Results	16
III. STABILITY ANALYSIS	28
3.1 Internal Damping in the Shaft and Bands	28
3.2 Formulation of the Equations of Motion for Damped System	32
3.3 Stability Criterion	33
3.4 Numerical Results	34
IV. FORCED WHIRLING.	41
4.1 Formulation	41
4.2 Numerical Results	44
V. COMPARISON WITH EXPERIMENTAL RESULTS	53
VI CONCLUDING REMARKS AND SUGGESTIONS FOR FURTHER RESEARCH.	56
REFERENCES	58

TABLE OF CONTENTS (Cont'd)

APPENDICES	Page
A DERIVATION OF ROTOR BASIC EQUATIONS INCLUDING GYROSCOPIC EFFECT	61
B INTERACTION BETWEEN THE RIM AND BANDS	64
C DETERMINATION OF IN-PLANE BAND STIFFNESS	69
D DETERMINATION OF OUT-OF-PLANE BAND STIFFNESS	76
E DERIVATION OF THE COMPLIANCE COEFFICIENTS	83
E.1 Turbine Shaft	83
E.2 Flywheel Shaft	86
F CALCULATION OF THE VISCOUS DAMPING COEFFICIENT FOR THE DAMPER IN THE SANDIA SPIN TEST FACILITY.	91
G COMPUTER PROGRAM DOCUMENTATION AND LISTING	92

LIST OF TABLES

TABLE		Page
1.1	Material Properties of the Composite Materials Used in the Sandia Thick-Ring Flywheel.	8
2.1	Mass and inertia parameters for Systems A and B	17
DI	Boundary Conditions for Out-of-Plane Bending of Bands. .	78

LIST OF FIGURES

Figure		Page
1.1	Schematic diagram of the Sandia flywheel system, as installed in the Sandia-Livermore spin-test facility. .	4
1.2	Side elevation of one half of the Sandia thick-ring flywheel	6
1.3	Plan view of one quarter of the Sandia thick-ring flywheel	7
2.1	Mode identification for System A: The number denotes the mode number and the suffixes F and R denote the forward and retrograde precessional branches, respectively	19
2.2	Mode identification for System B: The number denotes the mode number and the suffixes F and R denote the forward and retrograde precessional branches, respectively	20
2.3	Effects of increasing flywheel-shaft area moment of inertia and band angle ϕ on critical speeds $(\Omega_{cr})_{12}$ and $(\Omega_{cr})_{24}$	24
2.4	Effects of decreasing hub diametral mass moment of inertia I_{mh} and increasing band angle ϕ on critical speeds $(\Omega_{cr})_{12}$ and $(\Omega_{cr})_{24}$	25
2.5	Effects of increasing I_s and ϕ simultaneously on critical speeds $(\Omega_{cr})_{12}$ and $(\Omega_{cr})_{24}$	26
2.6	Effects of Increasing ϕ , I_s , I_π , and I_B simultaneously on critical speeds $(\Omega_{cr})_{12}$ and $(\Omega_{cr})_{24}$	27
3.1	Hysteresis loop of material under tension and compression	29
3.2	(a) Configuration of an overhung flywheel-shaft system; (b) Cross-sectional view of shaft	31
3.3	Effects of external viscous damping coefficient C_d on the onset of instability	35
3.4	Effects of increasing I_s and ϕ on the stability . .	37
3.5	Effects of decreasing ϕ and I_s simultaneously on the stability.	38

LIST OF FIGURES (Cont'd.)

Figure		Page
3.6	Effects of increasing $\bar{\phi}$ and I_s simultaneously on the stability	39
3.7	Effects of increasing $\bar{\phi}$, I_s , I_T , and I_R simultaneously on critical speeds $(\Omega_{cr})_{12}$ and $(\Omega_{cr})_{24}$	40
4.1	Ratios of translational amplitude to rim eccentricity for $C_d = 0, 3$, and 5 lb-sec/in	45
4.2	Ratios of tilt amplitude to rim eccentricity for $C_d = 0, 3$, and 5 lb-sec/in	46
4.3	Ratios of translational amplitude to rim initial tilt for $C_d = 0, 3$, and 5 lb-sec/in	47
4.4	Ratios of tilt amplitudes to rim initial tilt for $C_d = 0, 3, 5$ lb-sec/in.	48
4.5	Ratio of hub translational amplitude to rim eccentricity	49
4.6	Ratio of hub translational amplitude to rim initial tilt	51
4.7	Hub translational amplitude versus rotational speed	52
A1	Reference axes of a whirling rotor	62
B1	Side elevation of one half of the Sandia Thick-ring flywheel.	65
B2	A typical 30-degree repeating segment of rim and bands, and its schematic model.	67
C1	In-plane translation of the rim relative to the hub.	70
C2	Schematic diagrams showing that the bands of System B have been twisted by an angle of $\pi/2$ at the end attached to the hub.	73
D1	Schematic diagram depicting behavior of a set of two bands behaving as a double beam with compressive column action in the top beam and tensile tie-bar action in the bottom beam.	77
E1	Schematic loading diagram for the turbine shaft.	83

NOMENCLATURE

A	cross-sectional area of the rim
A_b	cross-sectional area of a single band
A_1, \dots, A_4	constants appearing in equations (D-4)
a_o, a_1	axial distances defined in Fig. E1
B	ratio of turbine-shaft inside diameter to outside diameter
B_1, \dots, B_4	constants appearing in equations (D-4)
$[B_1], [B_2]$	matrices defined in equation (2.15)
b	one half of the axial length of rim cross section
b'	one half of the axial length of hub
C_d, c	viscous damping coefficient in damper or damper clearance
E	elastic modulus of rim in circumferential direction
E_b	elastic modulus of band along its length
E_s	elastic modulus of shaft
e	eccentricity of a rotor
e_r	eccentricity of rim
F	force applied on shaft or damper
F_e, F'_e	respective elastic and hysteresis forces on shaft

NOMENCLATURE (Cont'd.)

$F_r, F_h,$ F_d, F_t	centrifugal forces of rim, hub, damper and turbine, respectively
F_x, F_y	respective x and y components of F
F_o	a dummy force
f_R	rim centrifugal body force per unit length
G	transverse shear modulus
\vec{H}	angular momentum vector
$I(x)$	distribution of rectangular area moment of inertia of band along the length of a twisted band
I_B, I_T	area moments of inertia in bearing and turbine shafts respectively
I_1, I_2	major and minor rectangular area moments of inertia of band
I_m	Mass moment of inertia of a rotor about its diametral axis
$I_{mr}, I_{mh},$ I_{md}, I_{mt}	mass moments of inertia about the diametral axis for rim, hub, damper, and turbine, respectively
i	$\sqrt{-1}$
J_m	mass moment of inertia of a rotor about the axis of revolution
$J_{mr}, J_{mh},$ J_{md}, J_{mt}	mass moment of inertia about the axis of revolutions for the rim, hub, damper, and turbine, respectively

NOMENCLATURE (Cont'd.)

K	transverse shear correction coefficient given by equation (E-10) for turbine shaft or translational flexural stiffness constant of shaft
K_{bip}	total in-plane stiffness of the bands
K_{bop}	total out-of-plane tilting stiffness of the bands
$[K_{ij}]$	inverse of $[\alpha_{ij}]$
K_{br}	radial stiffness of band, defined in the second of equations (B-9)
K_{θ}	tangential stiffness of rim defined in the first of equations (B-9)
k	tie-bar parameter $(P/E_b I_1)^{1/2}$
k_A, k_B	respectively defined as $(P_A/E_b I_2)^{1/2}$ and $(P_B/E_b I_2)^{1/2}$
k_b	in-plane flexural stiffness of a single band
k_s	integrated in-plane stiffness due to variation of axial tension in the bands
k'_b	tilting stiffness of a set of two bands
L	radial length between hub outside surface and rim inside surface
L_B, L_E	lengths defines in Fig. 1.1
L_H, L_T	
L_b	band unsupported span length
L_s	length of flywheel shaft
L_u, L_l	respective upper and lower portions of flywheel shaft

NOMENCLATURE (Cont'd.)

M	inertial couple
M_{AL}, M_{BL}	bending moments at the outer ends of the top and bottom bands when tilted
$M_r, M_h,$ M_d, M_t	inertia moments of the rim, hub, damper, and turbine, respectively
$[M_{ij}]$	inertia matrix
M_m	tilting moment carried by membrane stresses in a single band set
M_o	a dummy moment
m	mass in general
$m_h, m_r,$ m_d, m_t	mass of hub, rim, damper, and turbine, respectively
$[N_{ij}]$	gyroscopic-action matrix
N^o	circumferential normal force in rim due to steady centrifugal action
N_{fc}	circumferential normal force due to free centrifugal action
P	total tension force in a single band or pressure on the damper
P_A, P_B	total forces in individual top and bottom bands, respectively, when rim is tilted (see Fig. D1)
P_{Aj}, P_{Hj}	axial force in band set and component force in band set, acting parallel to displacement r_c
P_{bc}, P'_{bc}	centrifugal forces in bands

NOMENCLATURE (Cont'd.)

P_c, P_i	centrifugally induced and initial-winding tension in a single band
\bar{P}	integrated average of $P_{bc} \cos \phi$ given in equation (B-13)
P_H	total resultant force acting parallel to displacement r_c
$\{\bar{p}_i\}$	$\omega\{q_i\}$
Q	in-plane transverse shear force in rim
$\{Q_j\}$	generalized force column vector
$\{q_i\}$	generalized displacement column vector
R	radius to the centroid of the rim cross section
R'	$R \cos \phi - b \sin \phi$
R_h	outside radius of hub
R_i	inside radius of rim
r	shaft translation in plane of rotation
r_C	translational displacement of the rotor mass center
r_c	displacement of the flywheel rim relative to the hub
$r_r, r_h,$ r_d, r_t	translation in-plane of rotation for rim, hub, damper, and turbine, respectively

NOMENCLATURE (Cont'd.)

r_1	arbitrary radial position on band
t	time
U	total strain energy
u	radial displacement of arbitrary point on rim
u_{AL}, u_{BL}	in-plane (horizontal) displacements of top and bottom bands, respectively, relative to hub
u_b, u_{bo}	radial displacement of band in general and at its point of attachment to the rim
u_f	in-plane displacement of band along its length
u_o	radial displacement of edge of rim segment
u_{rc}	radial displacement of rim due to centrifugal action
V	transverse shear force in turbine shaft
w^A, w^B	vertical displacements of top and bottom bands at an arbitrary position x .
w_{AL}, w_{BL}	vertical displacements of end of top and bottom bands, respectively, relative to hub
x, y	translational displacements of a rotor associated with coordinate system xyz
x	position along band
xyz	fixed coordinate system defined in Fig. A1
$\bar{x}, \bar{\bar{x}}$	$\pi(L_b - x)/2L_b$ and $\pi x/2L_b$, respectively
$[\alpha_{ij}]$	generalized compliance matrix

NOMENCLATURE (Cont'd)

α_i	compliance coefficients
γ_b, γ_s	respective band and shaft loss tangents
ϵ_b, ϵ	radial strain in band and damper eccentricity ratio, respectively
θ	angular position on circumference of rim or damper
θ_o	angle defined in Fig. B1
ν	major Poisson's ratio
ρ, ρ_b	material density of rim and band, respectively
ϕ	out-of-plane tilting angle of rim
$\phi_r, \phi_h,$ ϕ_d, ϕ_t	tilting slopes of rim, hub, damper, and turbine, respectively
ϕ_x, ϕ_y	respective x and y components of ϕ
ϕ_o, ϕ_{or}	initial tilt in general and initial tilt in rim, respectively
$\bar{\phi}$	angle between band length direction and rim in-plane
ψ_1, ψ_2	angles defined in Fig. C1
μ	oil viscosity
Ω, Ω_{cr}	respective rotational and critical speeds
$(\Omega_{cr})_{ij}$	critical speed associated with the ith order and jth mode

NOMENCLATURE (Cont'd.)

ω natural frequency

$\hat{()}$ complex quantity of ()

CHAPTER I

INTRODUCTION

1.1. Historical Background

The scarcity and rising cost of petroleum have motivated international interest in conservation of petroleum. In view of the large automotive use of petroleum, an important means of accomplishing this could be by introduction of hybrid automobiles using flywheels for mechanical energy storage. Most of the flywheels developed to date have been rather heavy and rigid ones constructed of materials that are essentially homogeneous and isotropic, such as steel. However, with the continuing development of improved filamentary composite materials, there is considerable promise in the use of such advanced materials for flywheel. The primary motivation for this promise is the high strength-to-weight values for these materials, since the energy storage per unit weight can easily be shown to be directly proportional to this material parameter [1]. Another advantage is the less catastrophic nature of the failure of such flywheels; this can result in reduction of the weight of the containment system which surrounds the flywheel.

The current national effort to conserve petroleum as an energy source and the current high percentage of petroleum being used in automobiles motivated Congress to pass the Electric and Hybrid Vehicle Research, Development and Demonstration Act of 1976 (P. L. 94-413). Subsequently ERDA*

* Energy Research and Development Administration, which was merged into the the Department of Energy on October 3, 1977.

established its Electric and Hybrid Vehicle Demonstration Project [2]. In the future, such a vehicle is a prime candidate for application of composite-material flywheels, and the Department of Energy is mounting a significant research and development program in this area, as attested by many papers presented at the 1975 and 1977 Flywheel Technology Symposia [3, 4]. Activities of Sandia Laboratories in this area were reported as early as 1974 [5], and a major workshop on hybrid vehicles was held in 1976 [6].

Numerous configurations of filamentary-material flywheels have been proposed and some have been built and tested. Many of these have been assessed in a recent report [7] to ERDA. It suffices to mention here the following general classes of configurations:

1. Matrixless designs such as the radial brush [8] and loose-fiber-ring-types
2. Disk types, either filament-wound circumferentially [9] or laminated [10]
3. Rim types, either simple or multiple, as proposed by the Posts [11]
4. Shell types

The inherent flexibility of composite-material flywheels makes them potentially vulnerable to dynamic problems [12] which differ from those previously encountered in more rigidly mounted metallic rotors such as those in compressors and turbines. In this investigation, the dynamic phenomenon of the whirling mode, recognized as one of the most catastrophic ones associated with rotating machinery [13-16], is carefully examined.

To the best of presently available knowledge, the only previous

analysis concerning the whirling dynamics of rim-type flywheels existing in the literature was due to McKinnon [17]. He considered a two-mass system having three degrees of freedom: hub tilting, hub translation and rim tilting. He did not consider the radial flexibility of the connector with which the flywheel rim is attached to the hub. Also, only free whirling analysis was covered in [17].*

In the present work, free whirling, forced whirling, and stability analyses are studied for a four-mass, eight degree-of-freedom system believed to be the most appropriate model to describe the Sandia flywheel [18].

Since the research reported here was conducted in support of an experimental single-thick-ring flywheel undergoing research at Sandia Laboratories, the numerical results presented here are most directly applicable to that configuration. However, with the use of appropriate values of stiffnesses, masses and the dimensions, many of the analysis described would be applicable to other flywheel designs within the broad category of the rim type.

1.2 Description of the Sandia Band-Supported, Rim-Type Flywheel

The Sandia Laboratories experimental flywheel prototype (see Fig. 1.1), for which the analyses presented here are intended to be applied, consists of a thick rim of circumferentially wound graphite-epoxy attached to a central aluminum hub by means of radially wound bands of aramid-epoxy. The hub is attached to the turbine through a relatively flexible steel flywheel shaft. In turn, the turbine is supported by a steel turbine shaft

* It is noted that some program errors were found in [17].

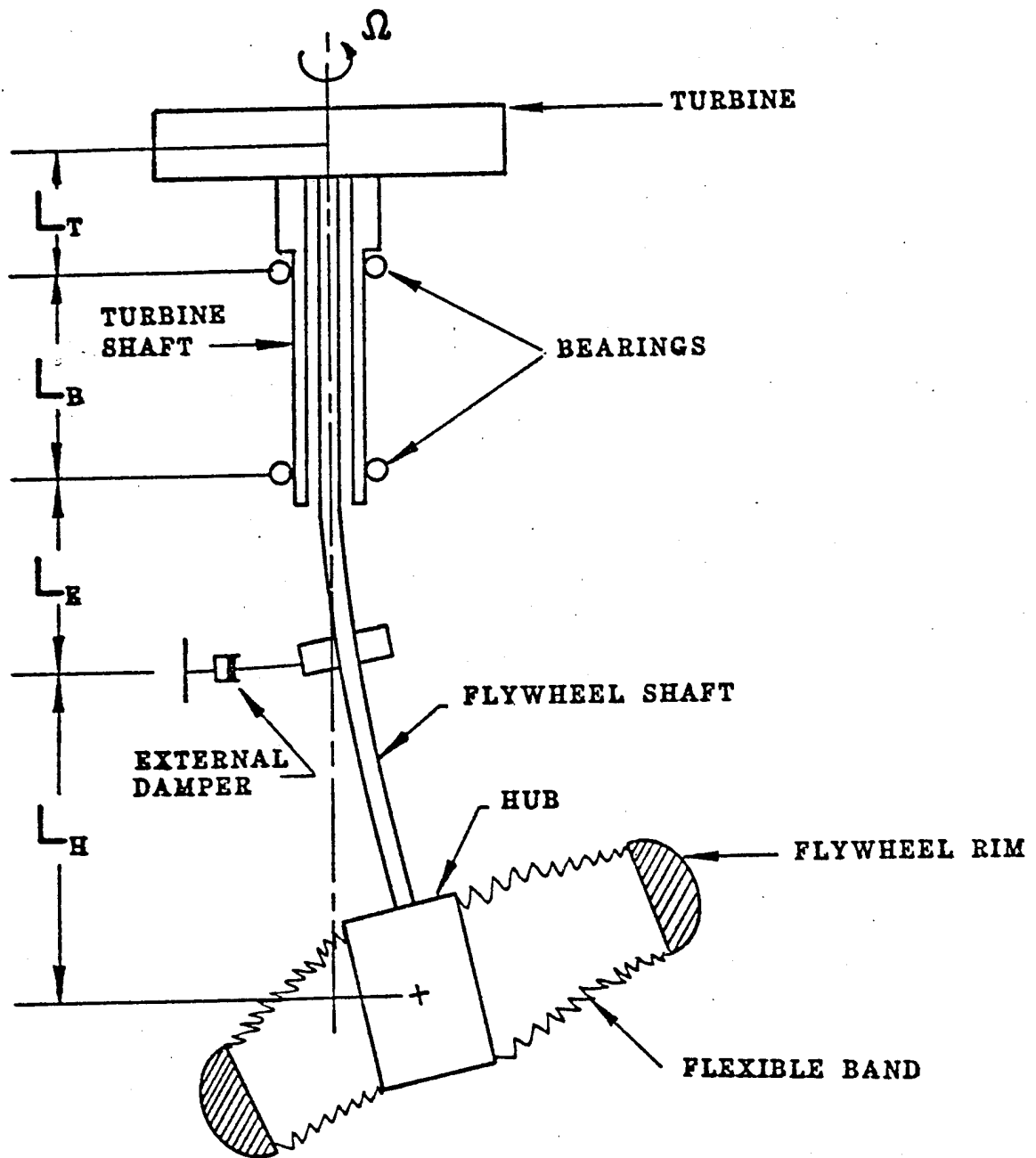


Fig. 1.1. Schematic diagram of the Sandia flywheel system, as installed in the Sandia-Livermore spin-test facility.

on a set of ball bearings. An external damper is located between the lower bearing and hub on the flywheel shaft. The side and plan views of the flywheel are shown in Figures 1.2 and 1.3. It can be seen that the ring is semi-elliptic in cross section and the bands are uniformly rectangular in cross section.

The elastic, strength, and density properties of the composite materials used in the rim and bands of the Sandia flywheel systems are listed in Table 1.1.

In [18], Reedy presented an analysis and predicted that the design energy storage goal of 0.56 kwh (22.4 watt-hr/lb) is achieved at a rotational speed of 32,000 rpm and that the governing material strength is reached at 39,850 rpm.

1.3. General Hypotheses

In all of the analyses presented here, the following engineering assumptions are made:

1. No statistical distributions of imperfections are considered, i.e. all eccentricities are assumed to be unique values. If sufficient statistical information were to become available, the approach recently introduced by Boyce and Kozik [19] could be used.
2. The bearings are assumed not only to have the same stiffness in any diametral plane, but also to act as simple supports.
3. All rotating components are assumed to be axisymmetric in cross section and stiffness properties.
4. All nonlinear effects are neglected (potential sources of nonlinearity include large deflections, bearing stiffness nonlinearities,

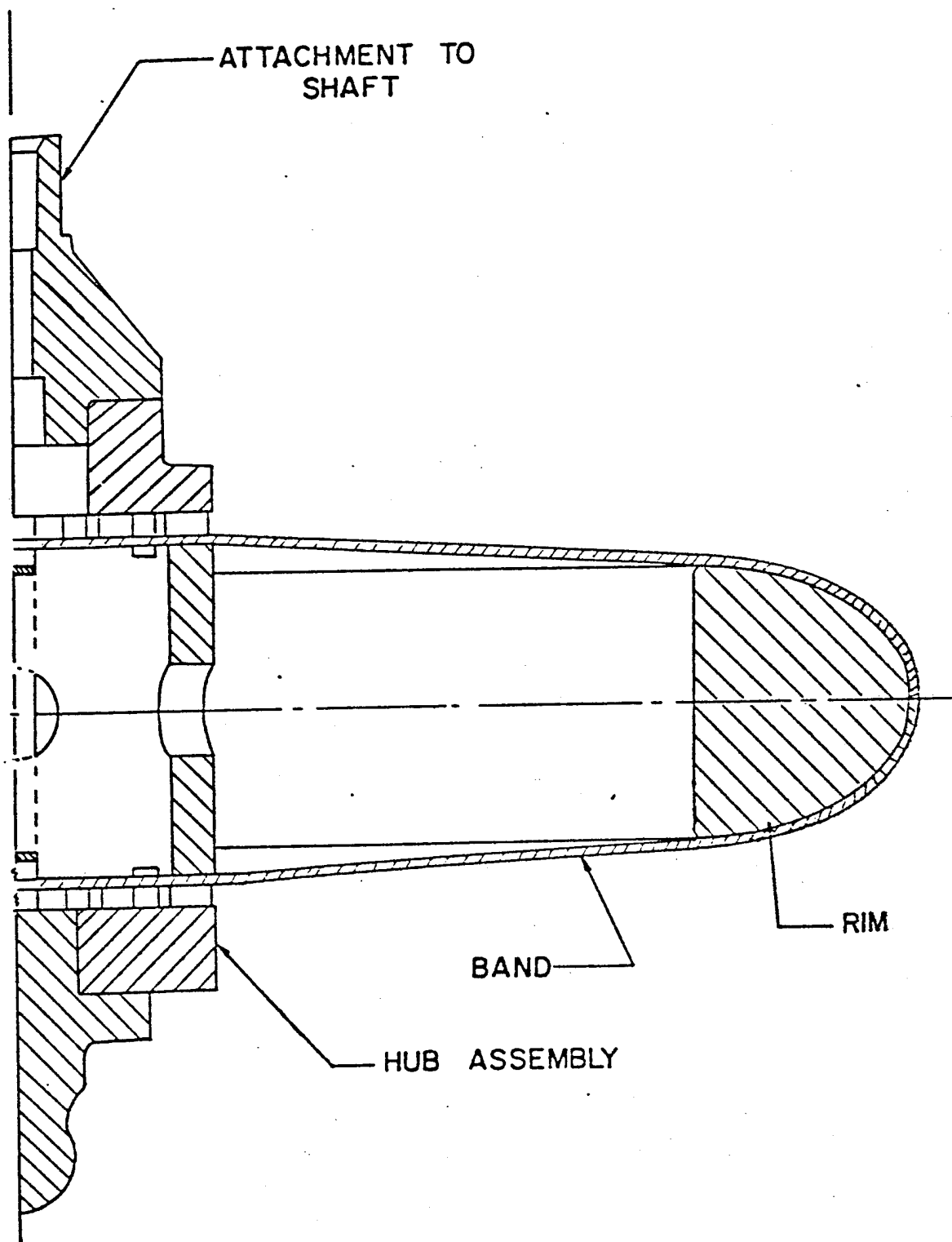


Fig. 1.2 Side elevation of one half of the Sandia thick-ring flywheel (System A).

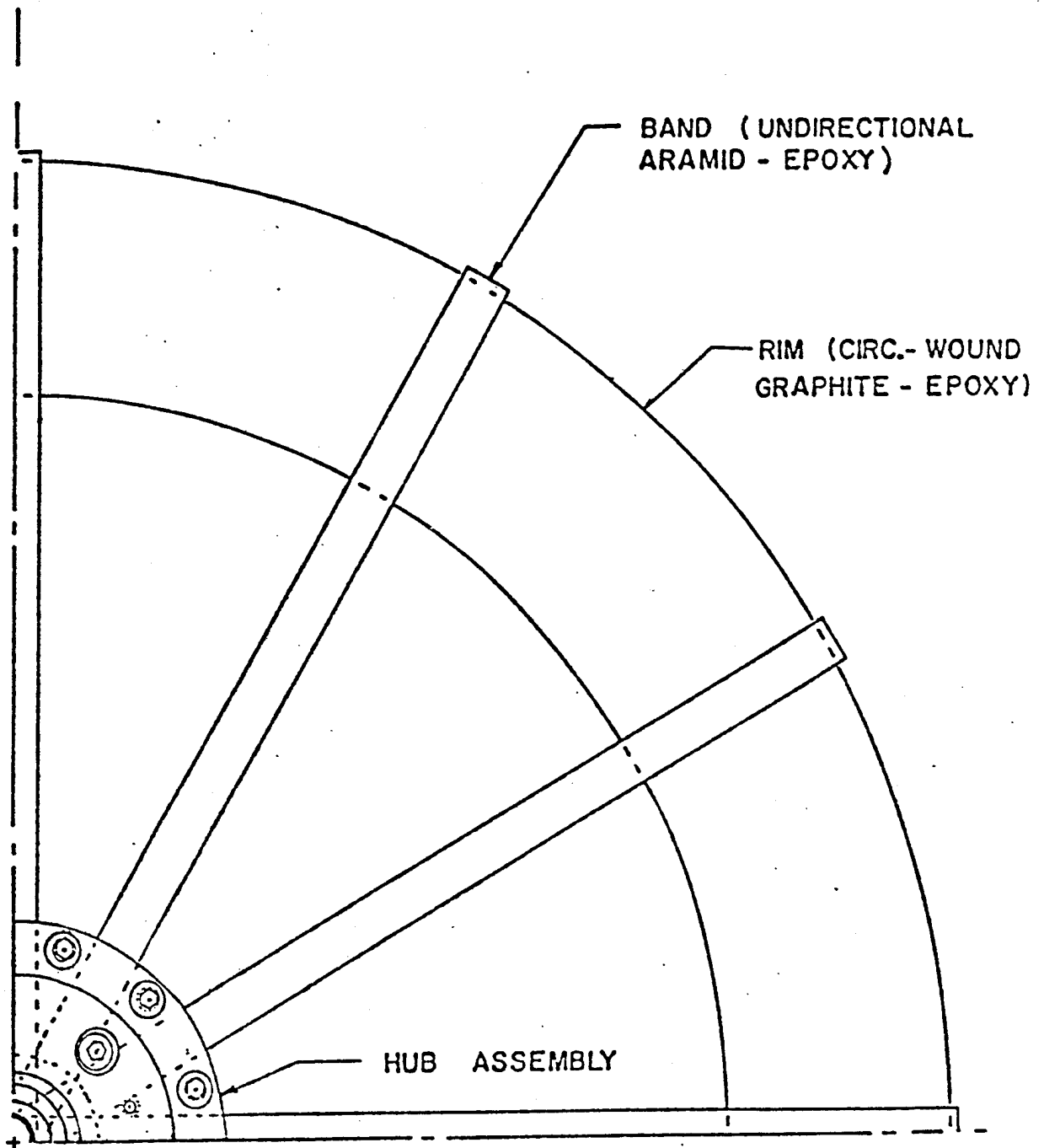


Fig.1.3 Plan view of one quarter of the Sandia thick-ring flywheel (System A).

Table 1.1. Material Properties of the Composite Materials
Used in the Sandia Thick-Ring Flywheel

Property	Units	Rim Material [*]	Band Material ^{**}
Young's modulus in fiber direction(L)	ksi	18.0	11.0
Transverse Young's modulus	ksi	1.28	0.71
Major Poisson's ratio (LT)	—	0.27	0.34
Minor Poisson's ratio (TL)	—	0.019	0.022
Shear modulus, LT axes	ksi	0.85	0.3
Tensile strength in fiber directions	ksi	220	200
Transverse tensile strength	ksi	4.8	2.3
Shear strength, LT axes	ksi	8.0	2.9
Specific weight	pci	0.054	0.050

* Hercules Type AS graphite fibers in epoxy matrix.

** du Pont Kevlar 49 aramid fibers in epoxy matrix.

bearing clearances and material nonlinearities.)

5. All temperature effects are neglected.

6. Although the flywheel shaft is vertical, it is assumed that the pendulum effect is small.

7. The shafts and bands are relatively flexible and of relatively low mass such that they can be modeled as discrete, massless flexible elements.

8. The flywheel rim, flywheel hub, and turbine disk are assumed to be rigid so that they can be considered to be discrete rigid masses.*

9. The system rotates at a constant angular velocity.

* It was shown in [20] that the rim has relatively high frequencies. Therefore it is justified that the rim element can be treated as a rigid one.

CHAPTER II

FREE WHIRLING OF THE UNDAMPED SYSTEM

2.1 The Gyroscopic Action of a Rotor

When a shaft carrying a rigidly attached rotor, overhung with respect to its supports, is rotated at constant speed, the centrifugal force produced by an eccentricity, regardless of how small the eccentricity is, causes the disk to tilt with respect to the axis of rotation. This tilting action, in turn, produces a gyroscopic couple about the diametral axis of the disk. The sense of the gyroscopic couple is such that it effectively stiffens the shaft at the speeds associated with forward precession and reduces the effective stiffness at the speeds associated with retrograde (or backward) precession. This gyroscopic effect on rotor whirling was first investigated by Stodola [21] in 1918, see also [22].

Let us consider a rotor which is pivotally mounted to a shaft rotating at an angular velocity of Ω as shown in Figure A.1. The following relationship can be obtained based on a system of fixed coordinates x, y, z (see Appendix A for detailed derivation of equations (2.1)).

$$F_x = -m \ddot{x} \quad (2.1a)$$

$$F_y = -m \ddot{y} \quad (2.1b)$$

$$M_x = -I_m \ddot{\phi}_x - J_m \Omega \dot{\phi}_y \quad (2.1c)$$

$$M_y = -I_m \ddot{\phi}_y + J_m \Omega \dot{\phi}_x \quad (2.1d)$$

Here $(\dot{}) \equiv \partial()/\partial t$; t is time; x and y are displacements of the rotor center respectively in the directions of x and y ; F_x and F_y are the forces applied on

the shaft respectively in x and y directions due to centrifugal action of the rotor; m is the mass of the rotor; I_m and J_m are the mass moments of inertia of the rotor about its respective axial and diametral directions; ϕ_x and ϕ_y are the angles of rotation of the rotor in the respective xz and yz planes; M_x and M_y are the moments applied on the shaft respectively in the xz and yz planes. It is noted that small deflections and angles were assumed in the derivation of equation set (2.1), i.e. higher order effects were neglected.

If complex notation is adopted, the following relations can be obtained:

$$F = -m \ddot{r} \quad (2.2a)$$

$$M = -I_m \ddot{\phi} + i J_m \Omega \dot{\phi} \quad (2.2b)$$

where

$$F \equiv F_x + i F_y \quad (2.3a)$$

$$M \equiv M_x + i M_y \quad (2.3b)$$

$$r \equiv x + i y \quad (2.3c)$$

$$\phi \equiv \phi_x + i \phi_y \quad (2.3d)$$

and $i = \sqrt{-1}$. It is noted that the gyroscopic effect was brought into the formulation through the second terms on the right hand side of equation (2.2b).

2.2 Formulation of the Equations of Motion for the Undamped Flywheel

System

In the case of the Sandia thick-rim flywheel (see Figure 1.1), the flywheel rim is connected to the hub by means of relatively flexible

bands, in contrast to the usual situation for overhung compressor disks which customarily are rigidly attached to the shaft. Furthermore, the flywheel hub has an appreciable mass and has a diametral mass moment of inertia which is larger than its axial mass moment of inertia ($J_{mh}/I_{mh} = 0.218$). This is the opposite of the case of the rim for which $J_{mr}/I_{mr} = 1.965$; therefore, the inertia couples for the rim and hub will act in opposite directions in the range of $0.218 < \omega/\Omega < 1.965$. For all of the above reasons, it is apparent that the rim and hub have to be considered as two different masses rather than a single disk. A few analyses of multi-mass disk-shaft have appeared in the literature; see for instance, [23], [24], [25] and [13] (pp. 225-230). Unfortunately, however, these analyses are all applicable only to the case when the flexible members connect to ground. In the case of the Sandia flywheel mounted in the spin-test facility, one flexible member (the bands) connects to an otherwise free mass (the flywheel rim).

In the whirling analysis, each rotor has two generalized displacements associated with translation (r) and rotation (ϕ). In the case of the Sandia flywheel as depicted schematically in Fig. 1.1, there are eight generalized displacements $\{q_i\} = (r_r, \phi_r, r_h, \phi_h, r_t, \phi_t, r_d, \phi_d)^T$. Here and hereafter the subscripts r, h, t , and d refer to the rim, hub turbine, and external damper respectively. The compliance equations can be written in matrix form as follows:

$$\{q_i\} = [\alpha_{ij}]\{Q_j\} \quad ; \quad i, j = 1, 2, \dots, 8 \quad (2.4)$$

Here the generalized forces are $\{Q_j\} = (F_r, M_r, F_h, M_h, F_t, M_t, F_d, M_d)^T$ and the α_{ij} are the compliances. Due to the nature of the connection

between rim and hub as well as the necessary symmetry of the array as required by Maxwell's reciprocal principle, some of the compliance terms are repeated in the array, which can then be written as follows:

$$[\alpha_{ij}] = \begin{bmatrix} \alpha_{11} & \alpha_{12} & \alpha_{33} & \alpha_{12} & \alpha_{15} & \alpha_{16} & \alpha_{17} & \alpha_{18} \\ \alpha_{12} & \alpha_{22} & \alpha_{12} & \alpha_{44} & \alpha_{25} & \alpha_{66} & \alpha_{27} & \alpha_{28} \\ - & - & - & - & - & - & - & - \\ \alpha_{13} & \alpha_{12} & \alpha_{33} & \alpha_{12} & \alpha_{15} & \alpha_{16} & \alpha_{17} & \alpha_{18} \\ \alpha_{12} & \alpha_{44} & \alpha_{12} & \alpha_{44} & \alpha_{25} & \alpha_{66} & \alpha_{27} & \alpha_{28} \\ - & - & - & - & - & - & - & - \\ \alpha_{15} & \alpha_{25} & \alpha_{15} & \alpha_{25} & \alpha_{55} & \alpha_{25} & \alpha_{57} & \alpha_{58} \\ \alpha_{16} & \alpha_{66} & \alpha_{16} & \alpha_{66} & \alpha_{25} & \alpha_{66} & \alpha_{67} & \alpha_{68} \\ - & - & - & - & - & - & - & - \\ \alpha_{17} & \alpha_{27} & \alpha_{17} & \alpha_{27} & \alpha_{57} & \alpha_{67} & \alpha_{77} & \alpha_{78} \\ \alpha_{18} & \alpha_{28} & \alpha_{18} & \alpha_{28} & \alpha_{58} & \alpha_{68} & \alpha_{78} & \alpha_{88} \end{bmatrix} \quad (2.5)$$

$$\begin{aligned} \text{with } \alpha_{11} &= \alpha_{33} + 1/K_{bip} \\ \alpha_{22} &= \alpha_{44} + 1/K_{bop} \end{aligned} \quad (2.6)$$

Here K_{bip} is the band stiffness to resist relative in-plane translation between rim and hub, while K_{bop} is the band stiffness to resist relative out-of-plane rotation between rim and hub. The values of K_{bip} and K_{bop} increase not only with the initial tension in the bands but also with

rotational speed due to the centrifugal stiffening effect. Detailed derivations of K_{bip} and K_{bop} are presented in Appendices C and D. Derivation of α_{ij} as given in equation (2.5) is presented in Appendix E.

Inverting equation (2.4), one obtains the following relation:

$$\{Q_i\} = [K_{ij}]\{q_j\} \quad ; \quad i, j = 1, 2, \dots, 8 \quad (2.7)$$

where $[K_{ij}]$ is the stiffness matrix and is defined as follows:

$$[K_{ij}] = [\alpha_{ij}]^{-1} \quad (2.8)$$

Use of equation (2.2) in equation (2.7), the following relationships are obtained:

$$\left\{ \begin{array}{l} -m_r \ddot{r}_r \\ -I_{mr} \ddot{\phi}_r + i J_{mr} \Omega \dot{\phi}_r \\ -m_h \ddot{r}_h \\ -I_{mh} \ddot{\phi}_h + i J_{mh} \Omega \dot{\phi}_h \\ -m_t \ddot{r}_t \\ -I_{mt} \ddot{\phi}_t + i J_{mt} \Omega \dot{\phi}_t \\ -m_d \ddot{r}_d \\ -I_{md} \ddot{\phi}_d + i J_{md} \Omega \dot{\phi}_d \end{array} \right\} = [K_{ij}] \left\{ \begin{array}{l} r_r \\ \phi_r \\ r_h \\ \phi_h \\ r_t \\ \phi_t \\ r_d \\ \phi_d \end{array} \right\} \quad (2.9)$$

Assuming that the system whirls in a normal mode with whirling frequency ω , one seeks the following solutions:

$$\{q_i\} = \{\bar{q}_i\} e^{i\omega t} \quad ; \quad i = 1, 2, \dots, 8 \quad (2.10)$$

where \bar{q}_i is the amplitude of q_i .

Substituting equation (2.10) into equation (2.9), one obtains the following homogeneous linear algebraic equation set.

$$\{[M_{ij}]\omega^2 - [N_{ij}]\omega - [K_{ij}]\} \{\bar{q}_i\} = 0 \quad (2.11)$$

where $[M_{ij}]$ and $[N_{ij}]$ are 8×8 matrices with zero elements except for the following elements:

$$\begin{aligned} M_{11} &= m_r & ; & & M_{22} &= I_{mr} & ; & & M_{33} &= m_h & ; \\ M_{44} &= I_{mh} & ; & & M_{55} &= m_t & ; & & M_{66} &= I_{mt} & ; \\ M_{77} &= m_d & ; & & M_{88} &= I_{md} & ; & & & & \\ N_{22} &= J_{mr} \Omega & ; & & N_{44} &= J_{mh} \Omega & ; & & N_{66} &= J_{mt} \Omega & ; \\ N_{88} &= J_{md} \Omega & & & & & & & & & \end{aligned} \quad (2.12)$$

Equation (2.11) is referred to as a generalized eigenproblem [26, 27]. Such a problem can be reduced to the standard-type eigenproblem by using the following definition:

$$\{\bar{p}_i\} \equiv \omega \{\bar{q}_i\} \quad (2.13)$$

Using equation (2.13) in equation (2.11), one obtains the following equation

$$\begin{bmatrix} [0] & [I] \\ [B_2] & [B_1] \end{bmatrix} \begin{Bmatrix} \{\bar{q}_i\} \\ \{\bar{p}_i\} \end{Bmatrix} = \omega \begin{Bmatrix} \{\bar{q}_i\} \\ \{\bar{p}_i\} \end{Bmatrix} \quad (2.14)$$

where $[0]$ and $[I]$ are respectively 8×8 zero and unitary matrices, and $[B_1]$, $[B_2]$ are defined as follows:

$$\begin{aligned} [B_1] &\equiv [M]^{-1} [N] \\ [B_2] &\equiv [M]^{-1} [K] \end{aligned} \quad (2.15)$$

Equation (2.14) is one of the standard eigenproblem. Thus, its frequency ω can be solved, at each rotational speed Ω , by using any existing eigenproblem computer program.

2.3 Numerical Results

The numerical values of the various mass and inertia parameters for two different composite-material flywheel systems are listed in Table 2.1. Each of the two systems have the same rim, which is constructed of hoop-wound graphite-epoxy composite material and is designed to achieve an energy-storage capacity of 0.56-kwh at 31,500 rpm.

System A has flat-band-type spokes of aramid-epoxy unidirectional composite material and is shown in Fig. 1.2. There are six complete bands, i.e. the bands are located 30 degrees apart around the circumference. The bands are wound with an initial tension of 360 lb and pass through and are bonded to slots in the hub.

System B differs from System A primarily in the fact that System B has spokes which are wound flat on to the rim but undergo a 90-degree twist to be wound on to axially oriented pins at the hub. This twist and a lower initial winding tension in the bands (90 lb for System B) results in higher-in-plane compliance of the bands. However, the tilting compliance is smaller.

Solving the eigenvalue problem which is represented by equation (2.14) one can obtain modal frequencies as a function of the rotational speed. Plots of these relationships for

Table 2.1. Mass and inertia parameters for Systems A and B

Quantity	Symbol	Units	System	
			A	B
Rim mass	m_r	lb-sec ² /in	0.043	0.043
Hub mass	m_h	" "	0.0235	0.0258
Turbine mass	m_t	" "	0.020	0.020
Rim mass moment of inertia about its axis	J_{mr}	lb-in-sec ²	3.215	3.215
Hub mass moment of inertia about its axis	J_{mh}	" "	0.054	0.074
Turbine mass moment of inertia about its axis	J_{mt}	" "	0.067	0.067
Rim mass moment of inertia about a centroidal diameter	I_{mr}	" "	1.636	1.636
Hub mass moment of inertia about a centroidal diameter	I_{mh}	" "	0.247	0.238
Turbine mass moment of inertia about a centroidal diameter	I_{mt}	" "	0.040	0.040

Systems A and B are shown in Figures 2.1 and 2.2. These figures are plotted in log-log form in order to get them on the paper. All eight modes, with forward and retrograde branches for each, are shown for completeness. It should be mentioned that the retrograde branches correspond to negative rotating speeds, i.e., the direction of rotation of the whirling is a direction opposite to the direction of the running speed.

The intersections of the ω vs. Ω curves with straight lines of the form $\omega = n\Omega$ determine the so-called critical speeds (Ω_{cr}) which correspond to the values of running speed Ω at which dynamic instability may take place. The value $n(= \omega/\Omega)$ is called the order of the critical speed and it is usually either a positive or negative integer or its reciprocal. Lines corresponding to $n = \pm 1$ and $n = \pm 2$ are shown in Figures 2.1 and 2.2.

Critical speeds of positive orders are always associated with forward precession, in which the whirling phenomenon takes place in the same direction as the shaft rotation. In contrast, critical speeds of negative orders are always associated with retrograde precession, in which the whirling phenomenon travels in a direction opposite to the direction of shaft rotation.

There does not appear to be any unanimity concerning which orders of critical speeds are the most critical ones. For example, Stodola [21, 22], Biezeno and Grammel [13], and Hartog [14] emphasize the first order ($n = 1$). Also ref. [13] claims that backward-precession critical speeds are less dangerous than forward-precession ones. However, Yamada [28] observed experimentally retrograde as well as forward critical speeds of orders up to 8. Recently Thomson et al. [29] reported on

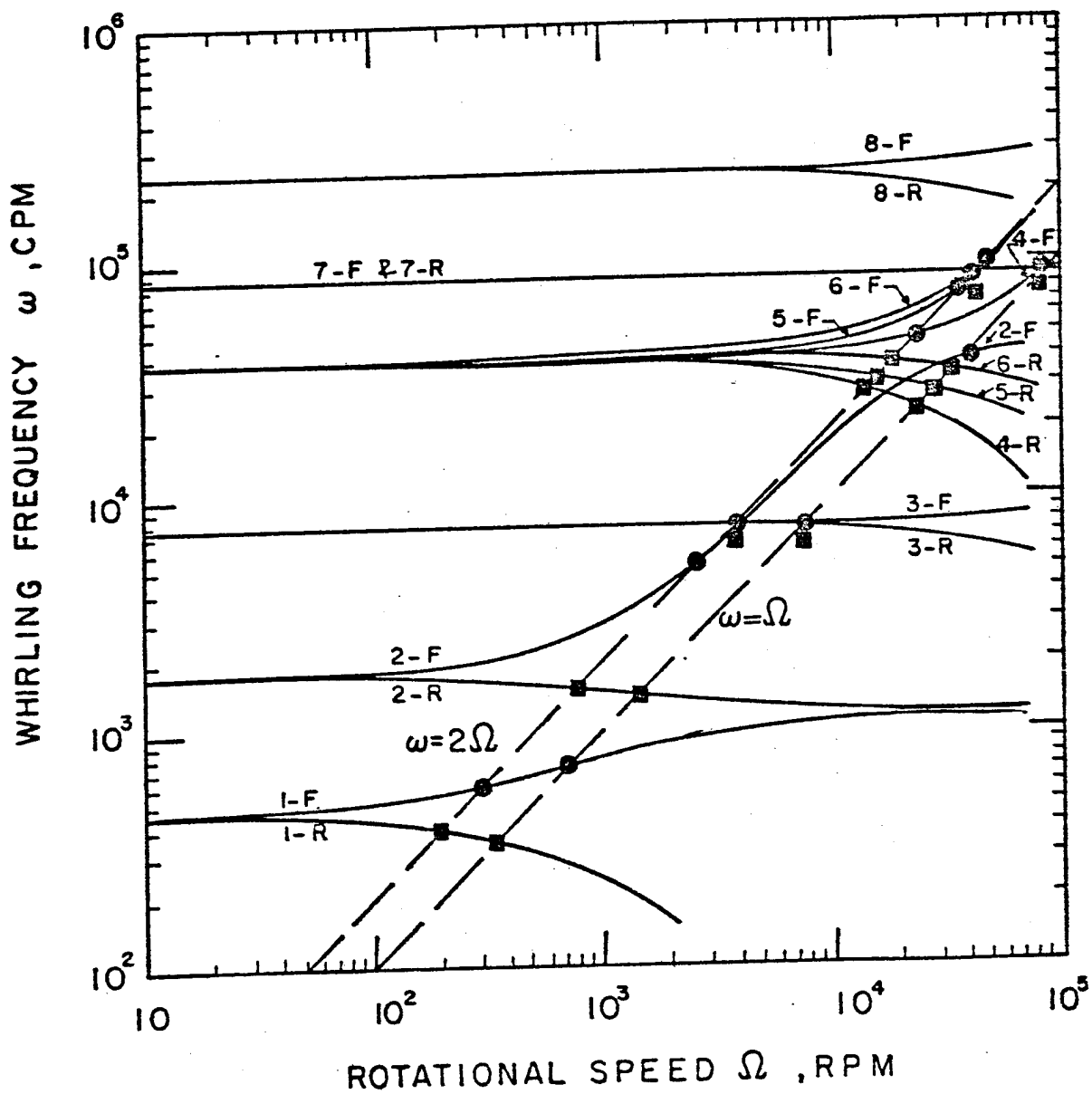


Fig. 2.1 Mode identification for System A: the number denotes the mode number and the suffixes F and R denote the forward and retrograde precessional branches, respectively.

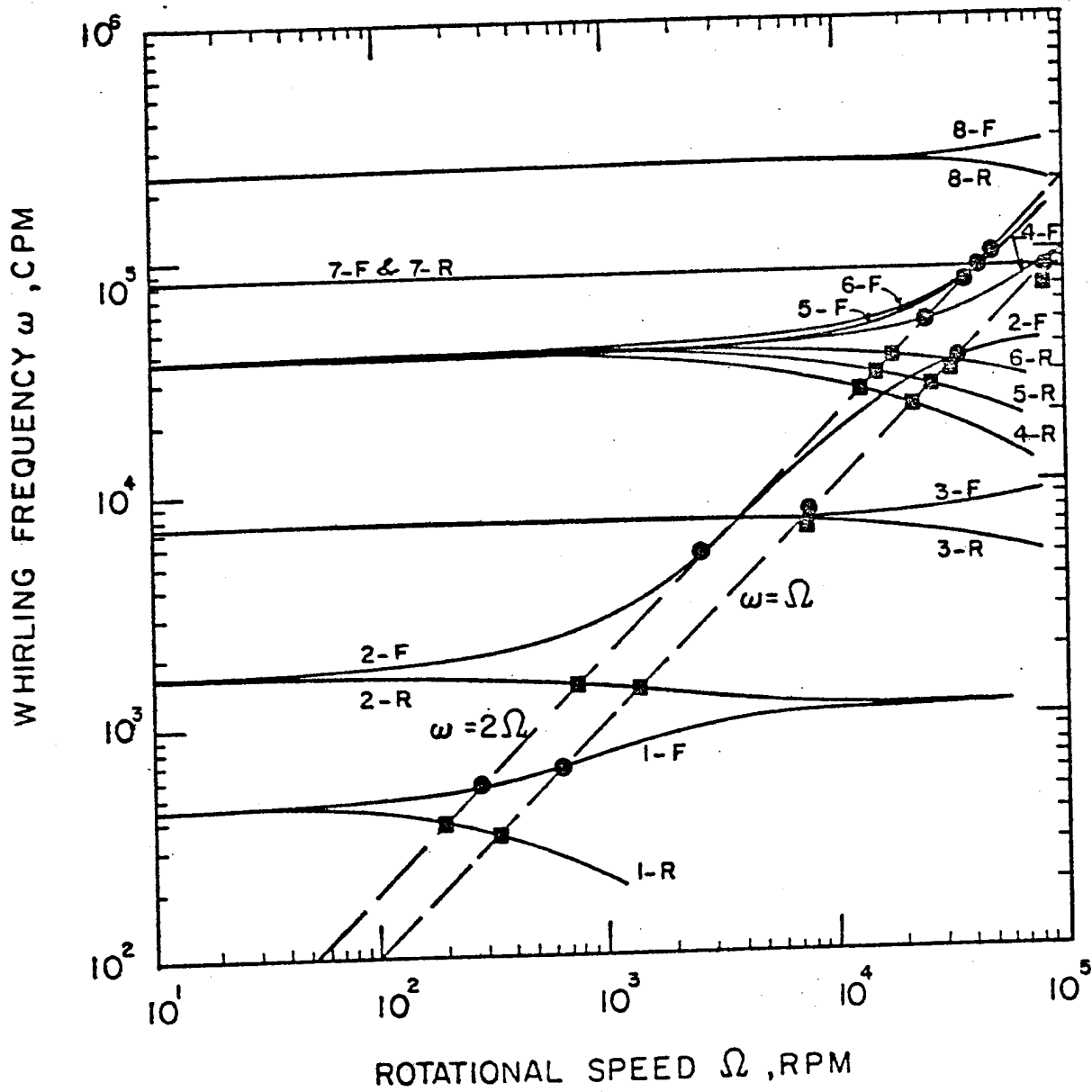


Fig. 2.2 Mode identification for System B: the number denotes the mode number and the suffixes F and R denote the forward and retrograde precessional branches, respectively.

experiments with single-mass flywheel systems. They had difficulty detecting the lower whirl phenomena, although they did detect one first-order, lower mode critical speed. For the upper mode they detected critical speeds of retrograde orders 1, 2, 3, and 5, on one system and 1 and 3 on the other, as well as forward orders 2, 3, 4, and 5 on both systems.

It is noted that in Figure 2.1 there are shown twenty-two first and second-order critical speeds in the rotational speed range up to 50,000 rpm: nine forward and thirteen retrograde. According to the reasoning of [13] and [14], the most important critical speeds would be the 1st-order forward ones at about 700, 7,600, and 38,100 rpm. In contrast, the experience of [17] and [29] suggest that higher mode forward critical speeds of second-order are most dangerous. It is noted that the amplitude ratios ϕ_r/ϕ_h and r_r/r_h increase rapidly as the running speed approaches the fourth-mode, second-order forward critical speed (approximately 24,200 rpm). This is consistent with comparison between the present results and the experimental results in [31] as discussed in Chapter V, which suggests that perhaps the second forward critical speed at the fourth mode is the most important one for System A.

The curious triple-curvature behavior (two inflection points) of the second-mode forward branch in the proximity of the fourth-mode forward branch (i. e. in the vicinity of $\omega = 45,000$ cpm, $\Omega = 23,000$ rpm) is reminiscent of the curve veering phenomenon discussed by Leissa [30] and was also found by McKinnon [17], who reported that an experimental wheel failed in the vicinity of these conditions.

The major differences in System B as compared to System A are smaller out-of-plane band compliance and larger hub mass and axial moment

of inertia (m_h , I_{mh}). Again there are twenty-two first- and second-order critical speeds up to 50,000 rpm: nine forward and thirteen retrograde as shown in Fig. 2.2. The first forward critical speeds are of 700, 7,600, and 38,100 rpm, while the most important one for the second-order forward critical speeds is approximately 24,300 rpm. It appears that the calculated fourth-mode, second-order forward critical speed of 24,200 rpm was not associated with the excessive amplitudes, during spin tests (see Chapter V), in the vicinity of 29,000-30,000 rpm. The most important critical speed is less certain. However, there is a distinct possibility that it could be a first-order forward one at the second mode.

One of the objectives in designing the flywheel systems is either to eliminate the critical speeds, if possible, in the operating speed range or to move them beyond the ~~maximum~~ operating speed. In the Sandia System A and B designs, the two most dangerous critical speeds are the first order forward one at the second mode, $(\Omega_{cr})_{12}$, and the second-order forward one at the fourth mode, $(\Omega_{cr})_{24}$. In view of the nearly identical performance of Systems A and B in Figures 2.1 and 2.2, it is practically sufficient to present numerical results for only one system since these results are applicable to another system with an error of less than 0.5%.

Practical ways to increase $(\Omega_{cr})_{12}$ are (1) to increase the area moment of inertia of the flywheel shaft I_s , (2) to decrease the

* Physically, only flexural rotatory stiffness is needed since $(\Omega_{cr})_{12}$ is associated with the flywheel-shaft tilting mode. However, the most practical way to increase the flexural rotatory stiffness is to increase the shaft moment of inertia, which in turn increases the flexural translational and coupling stiffnesses of the shaft.

hub's diametral mass moment of inertia, and (3) to increase the angle of the bands with respect to the plane of the rim, $\bar{\phi}$. Effects of increasing both I_s and $\bar{\phi}$ on $(\Omega_{cr})_{12}$ and $(\Omega_{cr})_{24}$ are presented in Fig. 2.3. It is seen that (1) $(\Omega_{cr})_{24}$ is unaffected, (2) $(\Omega_{cr})_{12}$ is increased by approximately 3% for each one-degree increase in $\bar{\phi}$, and (3) $(\Omega_{cr})_{12}$ is increased by approximately only 1% when I_s is doubled. Effects of decreasing I_{mh} and increasing $\bar{\phi}$ on $(\Omega_{cr})_{12}$ and $(\Omega_{cr})_{24}$ are shown in Fig. 2.4. The first two results for Fig. 2.3 given above remain applicable. Also, $(\Omega_{cr})_{12}$ is increased by approximately 18% when I_{mh} is reduced to 80% of the original. Critical speed $(\Omega_{cr})_{24}$ remains unchanged for the above two cases and for the case even when I_s and $\bar{\phi}$ are increased simultaneously as shown in Fig. 2.5. In order to increase critical speed $(\Omega_{cr})_{24}$, it is necessary to increase the area moments of inertia of the flywheel shaft and turbine shaft as well as the angle $\bar{\phi}$ simultaneously as shown in Fig. 2.6. When the foregoing three parameters are doubled simultaneously, critical speed $(\Omega_{cr})_{24}$ is increased from 24,200 rpm to 31,800 rpm as can be seen in Fig. 2.6.

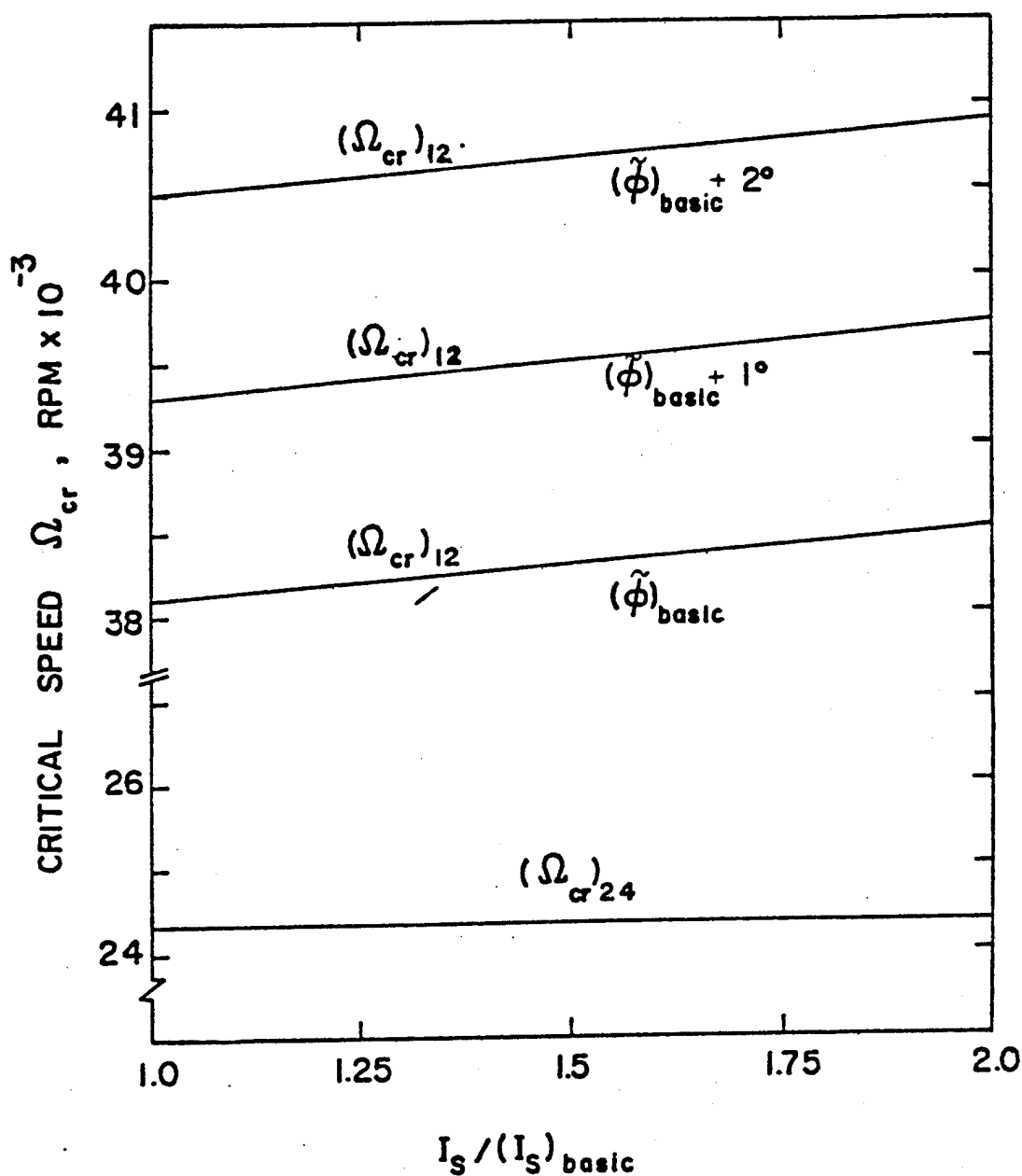


Fig. 2.3 Effects of increasing flywheel-shaft area moment of inertia and band angle $\tilde{\phi}$ on critical speeds $(\Omega_{cr})_{12}$ and $(\Omega_{cr})_{24}$.

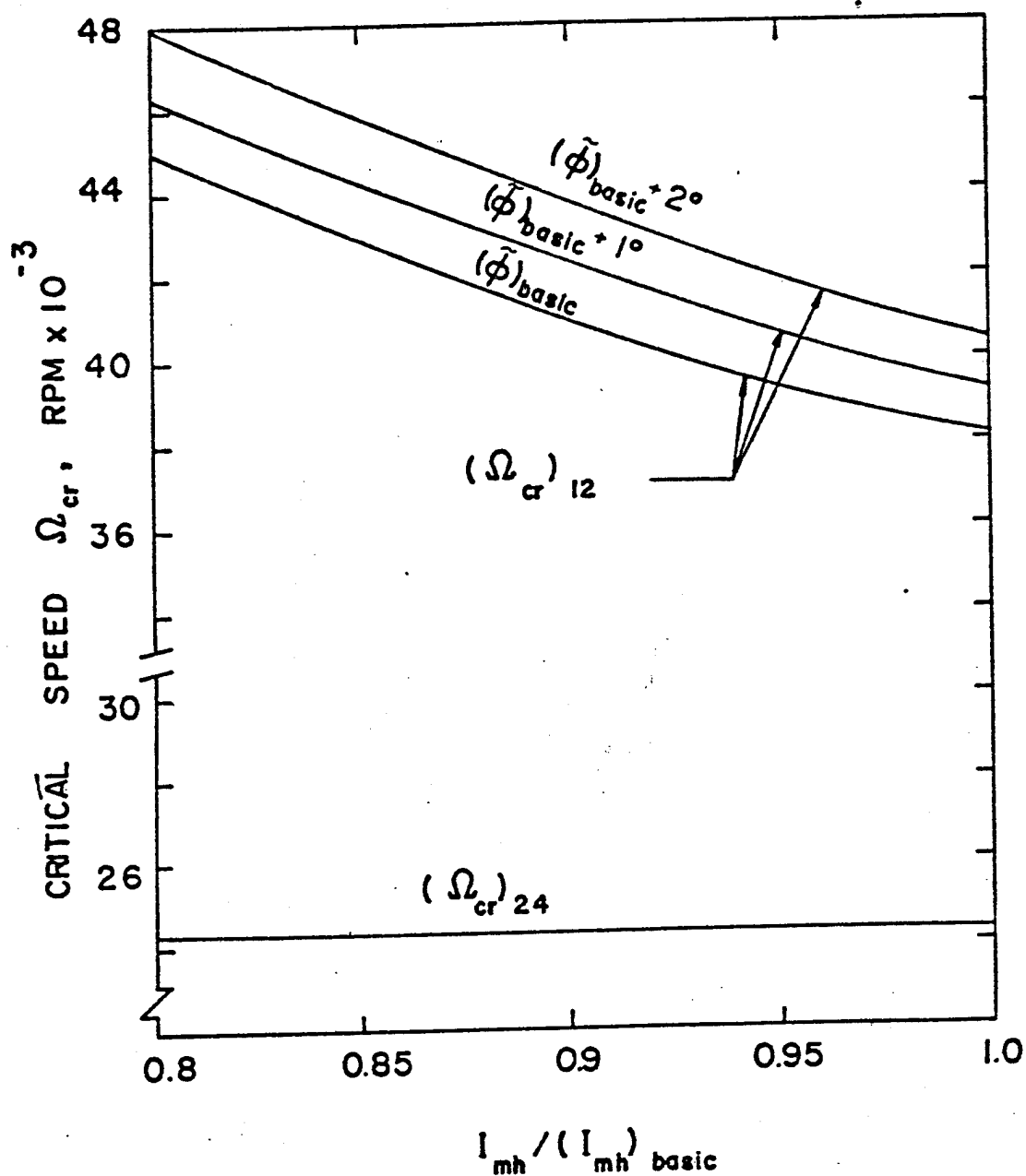


Fig. 2.4 Effects of decreasing hub diametral mass moment of inertia I_{mh} and increasing band angle $\tilde{\phi}$ on critical speeds $(\Omega_{cr})_{12}$ and $(\Omega_{cr})_{24}$.

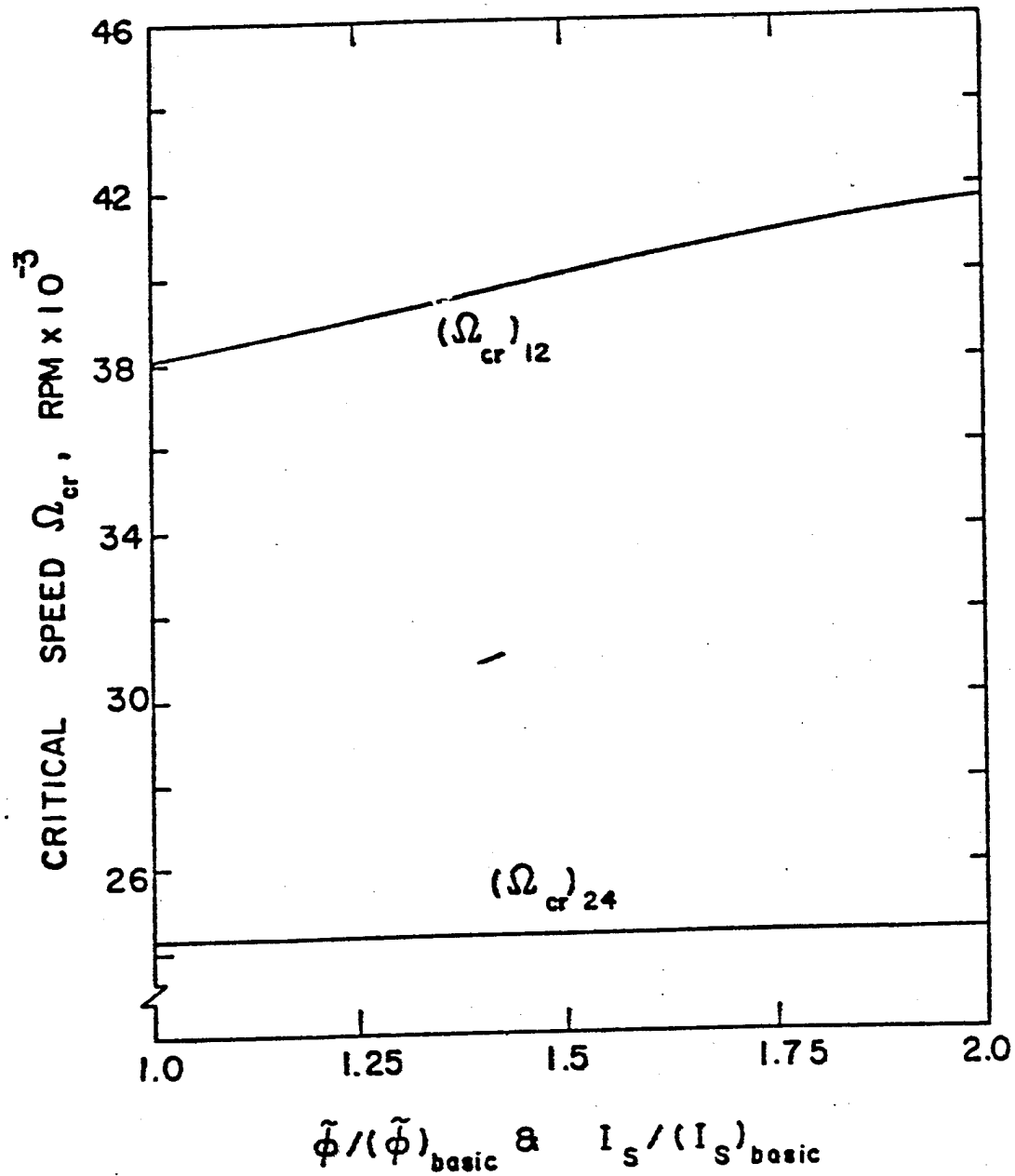


Fig. 2.5 Effects of increasing I_s and $\bar{\phi}$ simultaneously on critical speeds $(\Omega_{cr})_{12}$ and $(\Omega_{cr})_{24}$.

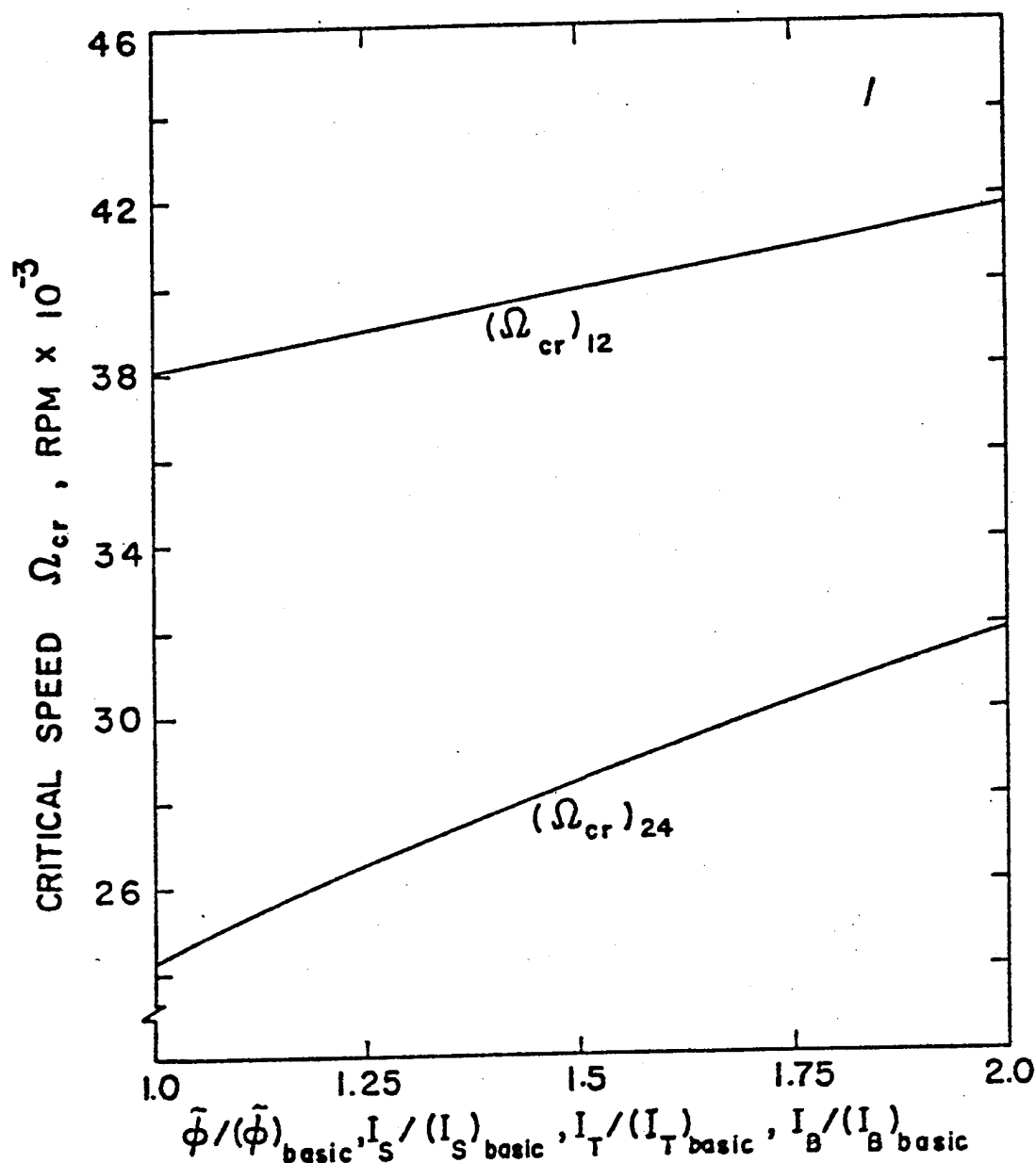


Fig. 2.6 Effects of Increasing $\tilde{\phi}$, I_S , I_T , and I_B simultaneously on critical speeds $(\Omega_{cr})_{12}$ and $(\Omega_{cr})_{24}$.

CHAPTER III

STABILITY ANALYSIS

3.1 Internal Damping in the Shaft and Bands

As in ordinary (non-rotating) vibratory systems, internal friction (damping) is always present in rotating shafts if the whirling speed is different from the shaft rotational speed. This internal friction has the effect of resisting shaft motion and causes dissipation of energy. It has been well known that internal damping has the effect of reducing the amplitude of a non-rotating vibrating system and thus stabilizes such a system. In rotating machinery, however, if the rotational speed is above the lowest first-order critical speed, a peculiar phenomenon sometimes can be observed, i. e., the amplitude of whirling vibration gradually builds up and finally leads to an unstable motion. To explain this kind of phenomenon, the imperfection of shaft elastic properties must be considered.

There have been two approaches used in the literature to describe internal damping: the viscous type [32, 33] and the hysteresis type [29, 33]. The former is incorporated in a similar way as in the simple spring-mass-dashpot system where the friction force is proportional to the velocity and thus the energy dissipation is proportional to the frequency. This characteristic, however, is not typical of most shaft materials where the dissipation is of the hysteresis type and nearly independent of the frequency. Qualitative measurements of internal damping were first carried out by Kimball [34]. He loaded an end-supported shaft and observed an additional deflection, besides the elastic deflection, in a direction normal to the loading when the shaft was set in rotation. He also observed that this additional

deflection is independent of the rotational speed and is linearly dependent on the elastic deflection, provided that the elastic deflection is not too large. In other words, the ratio of this additional deflection to the elastic deflection is equal to a constant within the limitation of linear theory.

Experiments with tension and compression show that even at very low stress levels, materials are not perfectly elastic. This inelastic behavior is reflected in the hysteresis loop as shown in Figure 3.1. The elastic behavior is represented by the straight line AOA, while the width of the loop depends on the stress level applied in the experiment. Under steady-state conditions, the loop is stabilized as an ellipse with the enclosed area equal to the amount of energy per unit volume dissipated per cycle due to hysteresis.

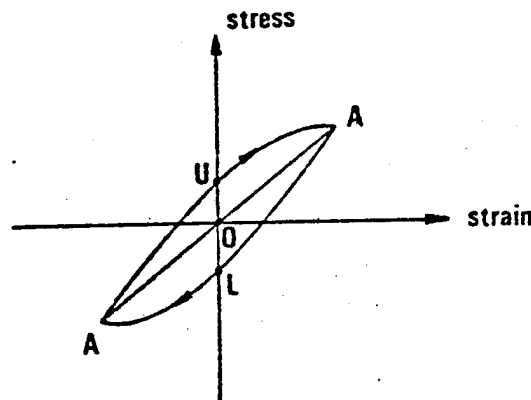


Fig. 3.1 Hysteresis loop of material under tension and compression.

Consider an overhanging flywheel-shaft system which is deflected

by a force F_e as shown in Figure 3.2. The system has a rotational speed Ω , and a whirling speed ω . In order to be consistent with the right-hand coordinate system xyz , Ω and ω should be positive for the directions shown in Fig. 3.2(b). For the case $\Omega > \omega$, any specific fiber in the shaft rotates counterclockwise. When the outside fiber moves inside through rotation, it is subjected to a stress variation from compression to tension and thus the upper portion of the stress-strain curve (curve AUA) as shown in Fig. 3.1 should be used. Using the same argument one can conclude that the lower portion (curve ALA) of Fig. 3.1 should be used to describe the inside fiber when it moves outside. Since the upper portion has a higher stress level compared to the lower portion, an additional force F'_e as shown in Fig. 3.2(b) is generated. The ratio of F'_e to F_e is equal to a constant, γ_s^* , under the limitation of linear theory. Since F'_e lags F_e by an angle of -90° , the total force \hat{F} can be written in complex form as follows:

$$\hat{F} = F_e - i F'_e = (1 - i \gamma_s) F_e \quad (3.1)$$

Noting that $F_e = Kr$ (K is the elastic stiffness and is proportional to the Young's modulus E_s), one can bring the internal damping into the formulation by replacing E_s used in the previous chapter with a complex modulus

$$\hat{E}_s = (1 - i \gamma_s) E_s \quad ; \quad \Omega > \omega \quad (3.2)$$

* The constant, γ_s , is usually called loss tangent.

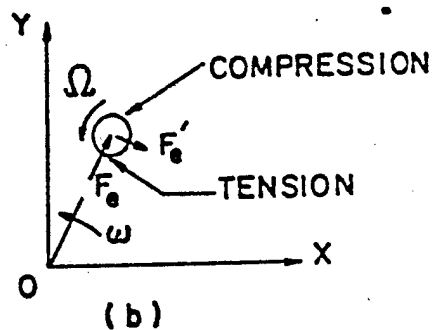
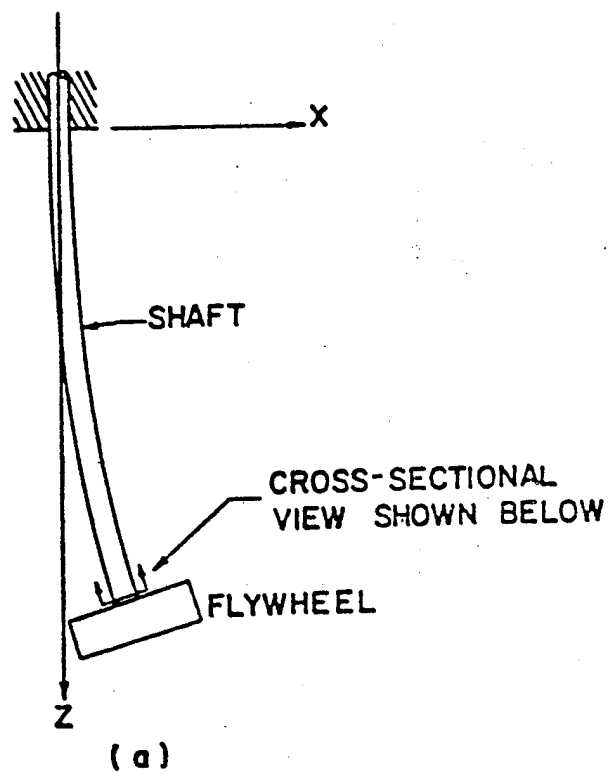


Fig. 3.2 (a) Configuration of an overhung flywheel-shaft system;
(b) Cross-sectional view of shaft.

With a similar argument, one obtains the following complex modulus for $\Omega < \omega$

$$\hat{E}_s = (1 + i \gamma_s) E_s \quad ; \quad \Omega < \omega \quad (3.3)$$

The flywheel shaft shown in Fig. 3.2 can also be bent by applying a moment on it. For such a case, one may use the same philosophy to reach the same conclusions as given in equations (3.2) and (3.3). It is noted that the results obtained above can be applied to a rotating shaft under any kind of supports.

In the Sandia flywheel system, the band material is Kevlar 49 aramid/epoxy. Since composite materials with polymeric constituents usually exhibit more internal damping than do the common metallic materials, one would expect that the bands exhibit appreciable internal damping. Although the geometric configuration for the bands is different than that in the shaft, a similar conclusion can be obtained. Thus the following equations should be used to bring the internal damping in the bands into the analysis.

$$\hat{E}_b = (1 - i \gamma_b) E_b \quad ; \quad \Omega > \omega \quad (3.4)$$

$$\hat{E}_b = (1 + i \gamma_b) E_b \quad ; \quad \Omega < \omega \quad (3.5)$$

3.2 Formulation of the Equations of Motion for the Damped System

In the Sandia flywheel system, an external damper is located between the lower bearing and hub on the flywheel shaft. The external force acting on the flywheel shaft at the position where the external damper located is

$$F_d = -m_d \ddot{r}_d - C_d \dot{r}_d \quad (3.6)$$

Here C_d is the viscous damping coefficient.

Using the complex moduli in the shaft and band materials as given in the previous section in conjunction with equation (3.6), for the external damper, one can formulate the damped flywheel system in a similar way to that presented for the undamped system in Chapter II. Assuming that the system whirls in a normal mode with a solution form of $\{q_1\} = \{\bar{q}_1\}e^{i\omega t}$, one obtains the following characteristics equation similar to equation (2.11)

$$\{[M]\omega^2 - [N]\omega - [\hat{K}]\}\{\bar{q}_1\} = 0 \quad (3.7)$$

where $[M]$ and $[N]$ are 8×8 matrices with zero elements except for the elements defined in equation (2.12) and $N_{77} = i C_d \Omega$; $[\hat{K}]$ is the complex version of stiffness matrix $[K]$ given in equation (2.8).

Using the same transformations as given in equation (2.13), one obtains the following equation

$$\left[\begin{array}{c|c} [0] & [I] \\ \hline [M]^{-1} [\hat{K}] & [M]^{-1} [N] \end{array} \right] \begin{Bmatrix} \{\bar{q}_1\} \\ \{\bar{p}_1\} \end{Bmatrix} = \omega \begin{Bmatrix} \{\bar{q}_1\} \\ \{\bar{p}_1\} \end{Bmatrix} \quad (3.8)$$

3.3 Stability Criterion

Perhaps the most popular stability criterion used in the literature for linear analyses is the Routh-Hurwitz criterion. However, in view of the large numbers of degrees of freedom considered here, application of this criterion by expansion of the determinant would be

extremely laborious. Here, the Routh concept is used directly by numerically determining the complex roots of equation (3.8). Using an existing routine*, one can compute the whirling frequencies for a given rotational speed Ω . In general, the whirling frequencies are complex numbers, i.e. $\omega = \omega_R + i\omega_I$. Thus, the solution can be written as $\{q_i\} = \{\bar{q}_i\}e^{-\omega_I t} e^{i\omega_R t}$. The quantity ω_R is the damped frequency; while the quantity $-\omega_I$ is the growth factor. It is noted that if $-\omega_I > 0$, the amplitude will grow with time exponentially and the system will become unstable. On the contrary if $-\omega_I < 0$, the system is in a stable condition. The computing procedure for predicting the onset of unstable motion is to start with a given suitable rotational speed Ω and compute all the frequencies then increase a small amount of Ω and repeat the computation until at least one of the growth factors becomes positive.

3.4 Numerical Results

As in the preceding chapter, the numerical results presented here are applicable to both Systems A and B since their differences are less than 0.5%. Values of γ_s and γ_b are assumed to be 0.005 and 0.0172 respectively. Effects of the external viscous damping coefficient C_d on the onset of instability are shown in Fig. 3.3. If $C_d = 0$, the onset of instability occurs at the lowest first-order forward critical speed. Only a small amount of C_d (less than 0.25 lb-sec/in) is required to stabilize unstable motion associated with the first and third modes for

* Detailed programs are present in Appendix F.

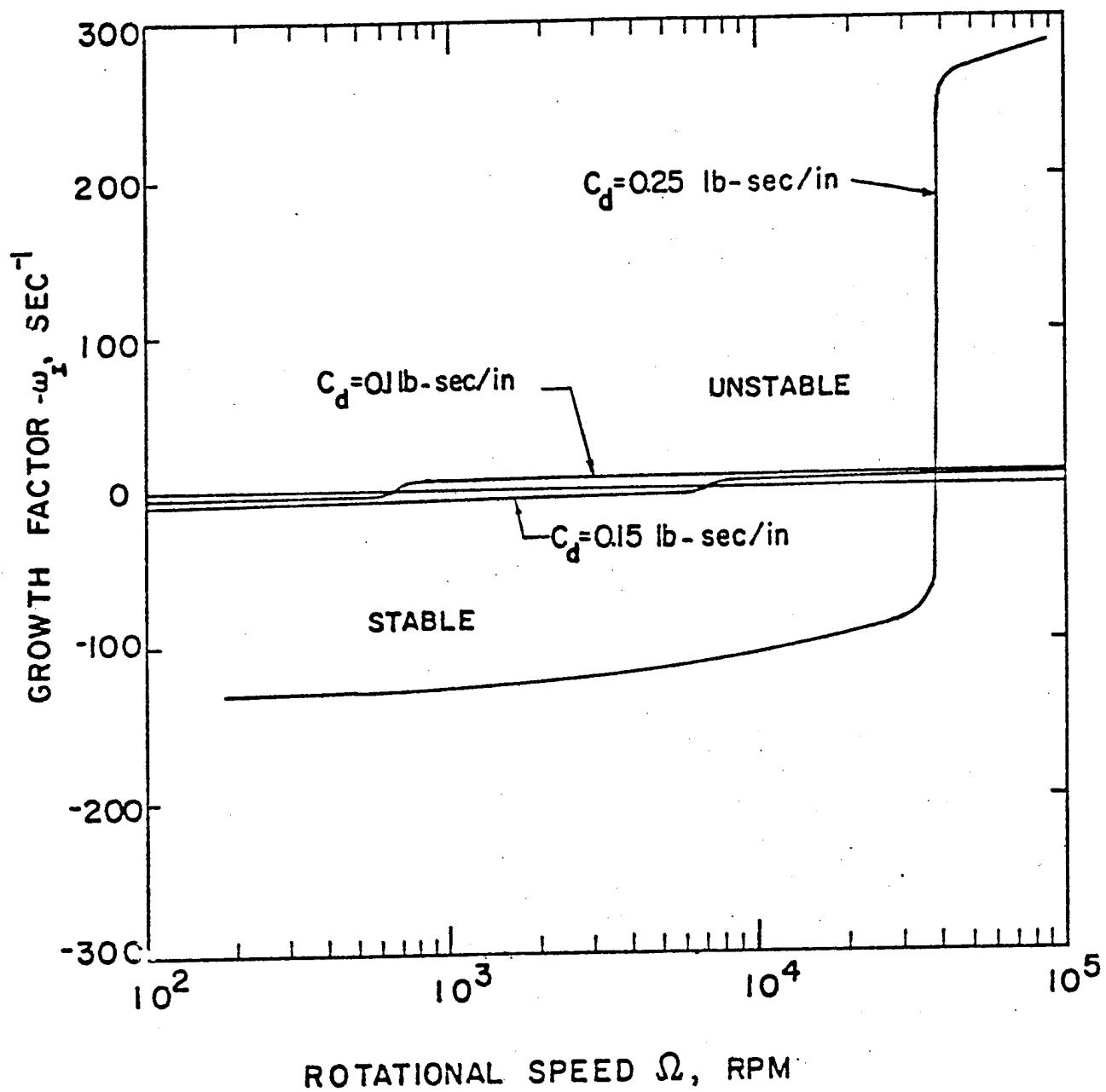


Fig. 3.3 Effects of external viscous damping coefficient C_d on the onset of instability.

$\Omega > \omega$. When the value of C_d is greater than approximately 0.2 lb-sec/in, the onset of instability jumps up to 38,100 rpm. Increasing the value of C_d has very little effect on increasing the onset of instability beyond 38,100 rpm. This implies that a considerable amount of external damping is required in order to stabilize the system associated with the second forward mode. Alternatively, this onset can be brought up to a fairly high rotational speed by (1) increasing the flywheel-shaft area moment of inertia (Fig. 3.4), (2) reducing the diametral mass moment of inertia of the hub (Fig. 3.5), (3) increasing the flywheel-shaft area moment of inertia and band angle $\tilde{\phi}$ simultaneously (Fig. 3.6), or (4) increasing the flywheel-shaft and turbine-shaft area moments of inertia as well as the angle $\tilde{\phi}$ (Fig. 3.7). However, the most convenient and practical ways to increase the speed at which such unstable onset occurs in the spin-test set-up are the first three or their combination.

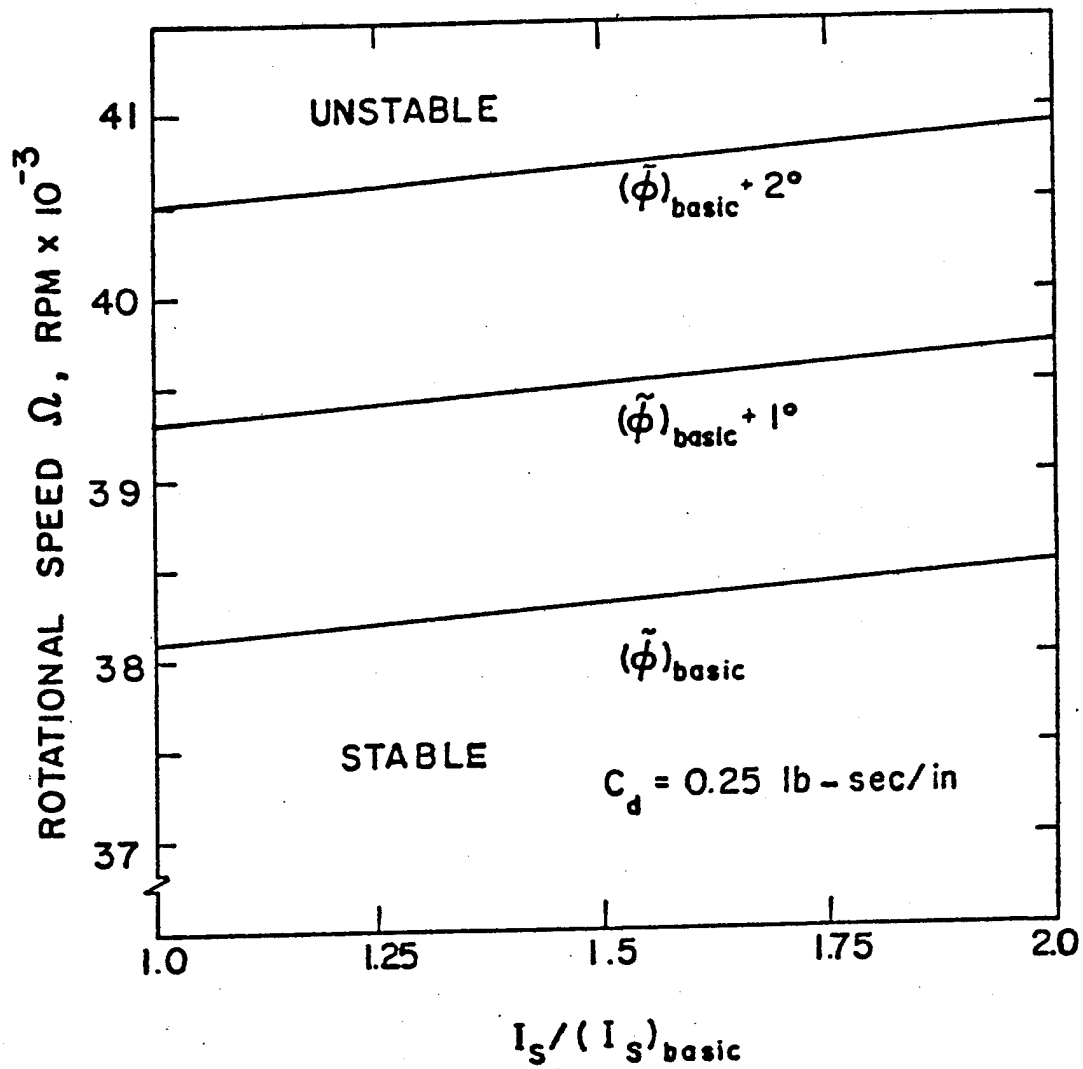


Fig. 3.4 Effects of increasing I_S and ϕ on the stability.

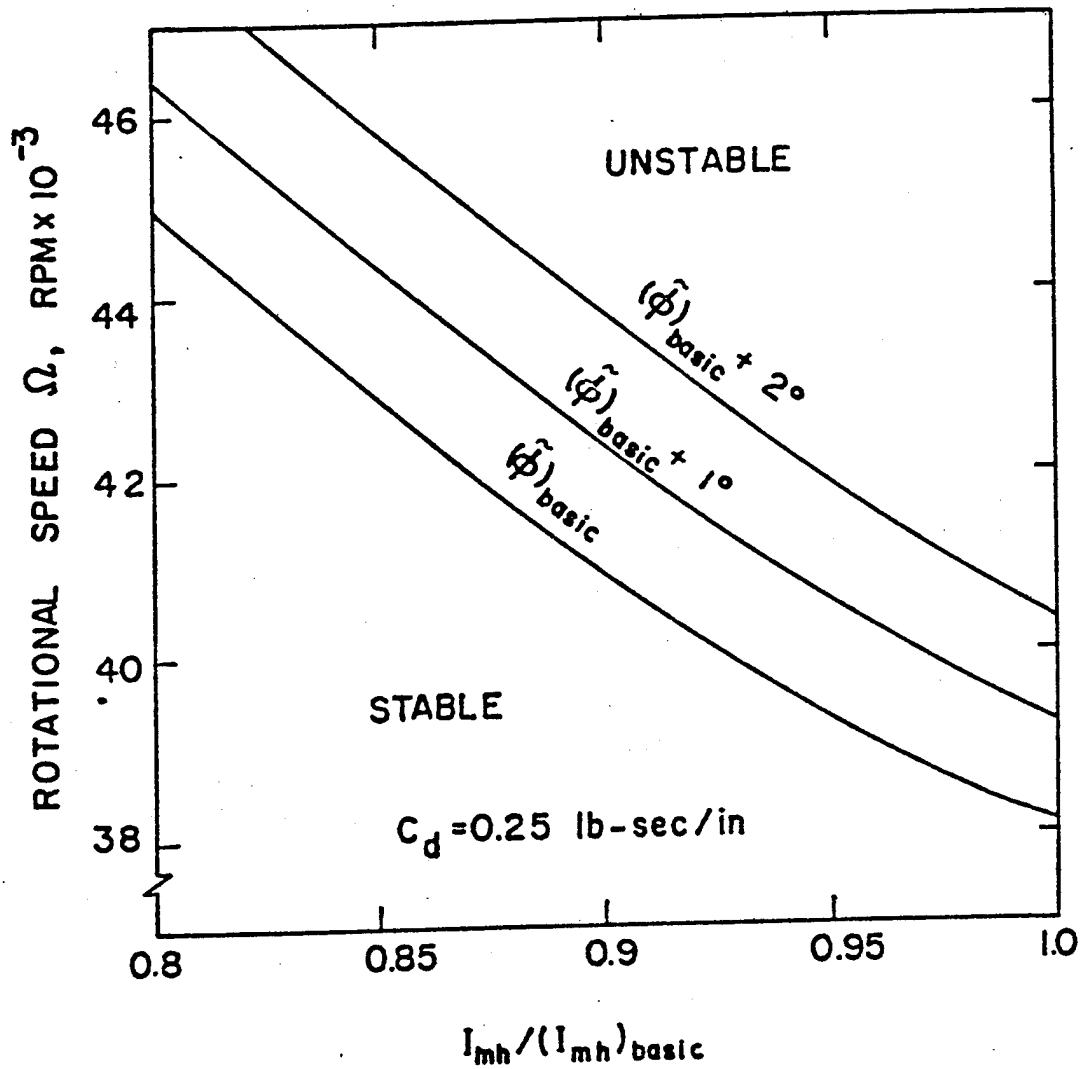


Fig. 3.5 Effects of decreasing I_{mh} and increasing ϕ on the stability.

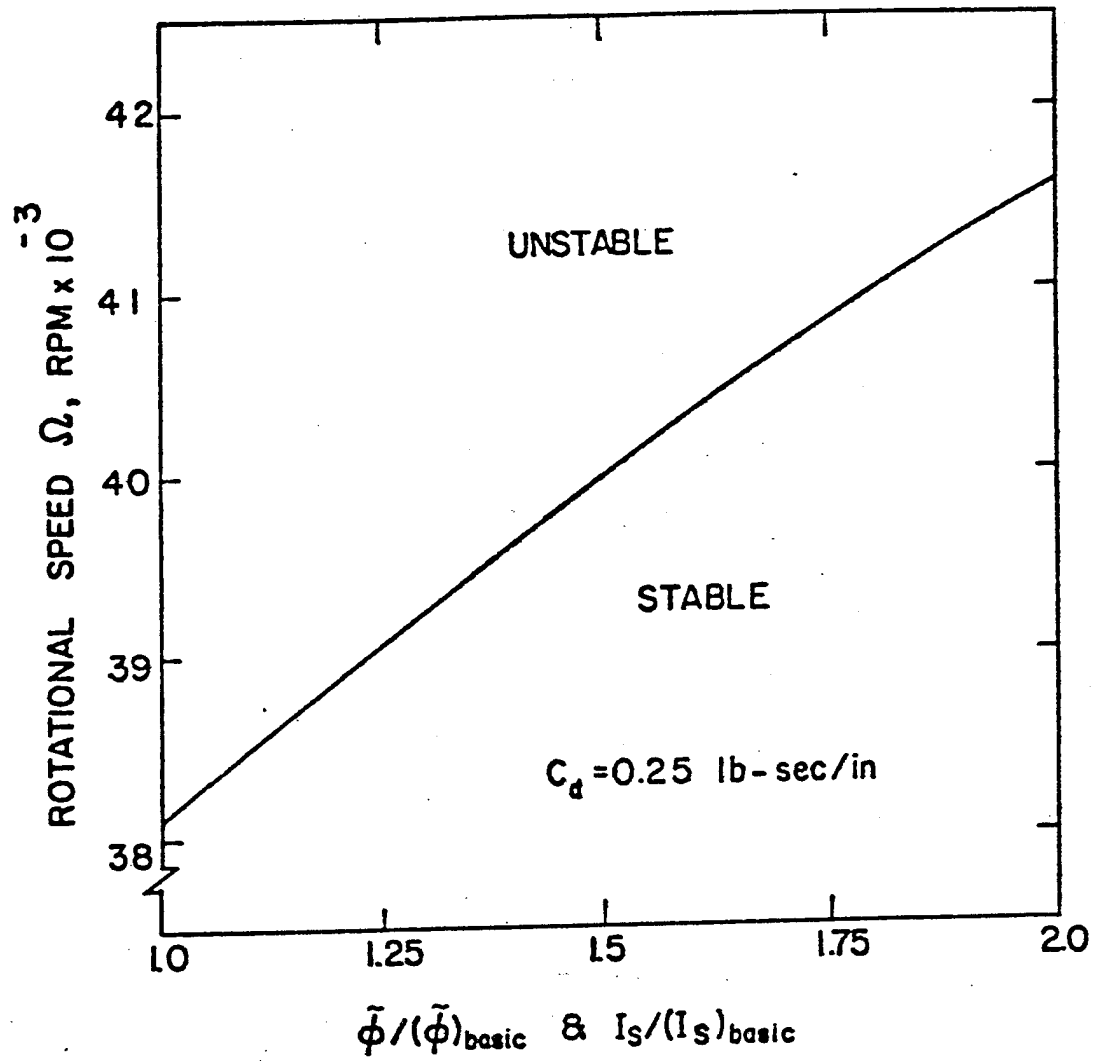


Fig. 3.6 Effects of increasing $\tilde{\phi}$ and I_s simultaneously on the stability.

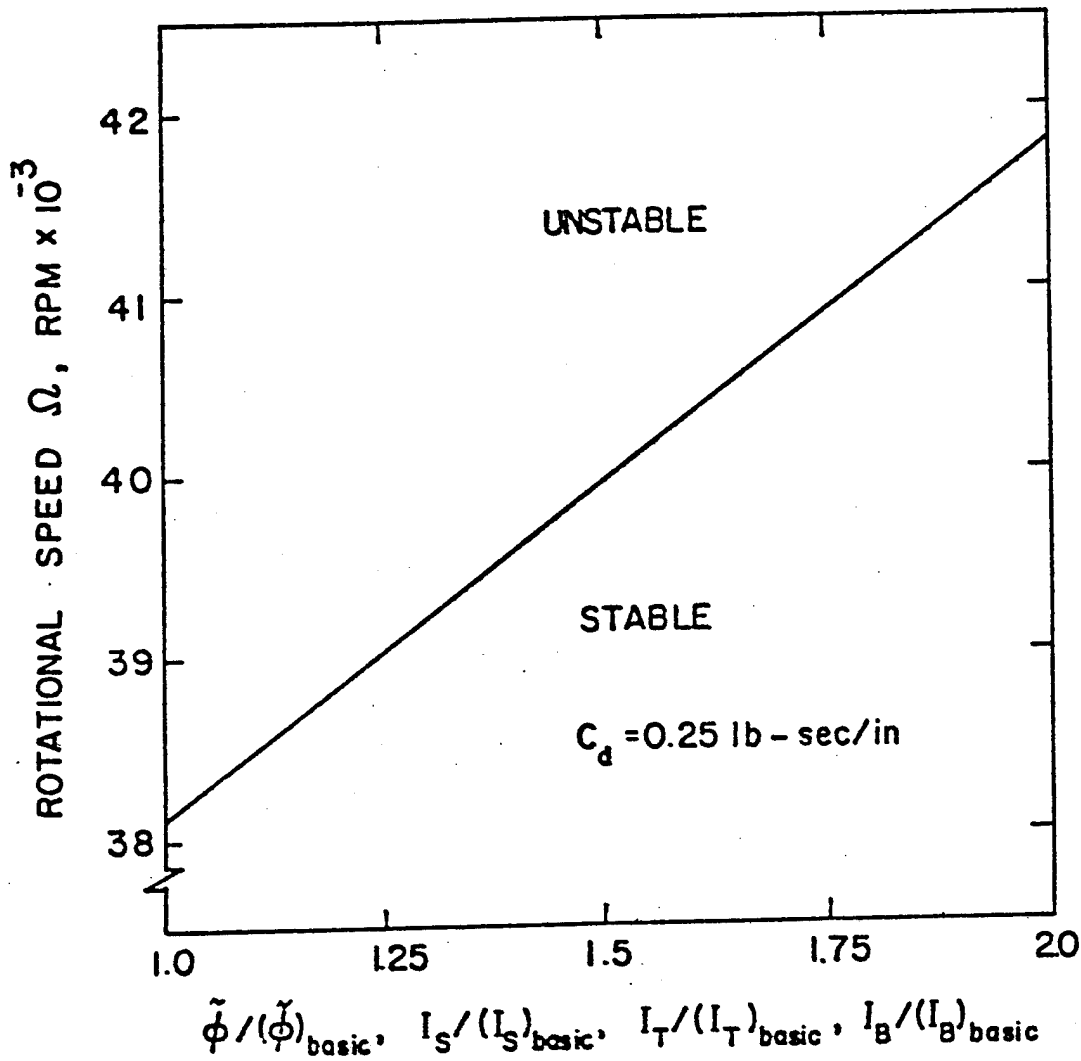


Fig. 3.7 Effects of increasing $\tilde{\phi}$, I_S , I_T , and I_B simultaneously on critical speeds $(\Omega_{cr})_{12}$ and $(\Omega_{cr})_{24}$.

CHAPTER IV

FORCED WHIRLING

4.1 Formulation

Although the rotors used for high-speed flywheels can be well balanced in today's technology, it is not possible to eliminate the initial unbalance completely. This initial unbalance (eccentricity) causes resonance in the neighborhood of first-order critical speeds. In the absence of damping and at a fixed running speed, the resonance response will build up and finally cause the failure of the system no matter how small the initial unbalance is. Another source of excitation for first-order critical whirling is unavoidable initial tilt of the flywheel. For reasons stated in the preceding chapter, no hysteresis damping is produced at the first-order forward critical speeds. In order to reduce the response amplitudes, there must be some external damper installed in the flywheel system. In the Sandia flywheel system, there is an external damper located on the flywheel shaft as shown in Fig. 1.1. This external damper not only effectively reduces the response amplitudes, but also is effective in overcoming adverse internal damping to stabilize the system when the operating speed is beyond the lowest first-order critical speed. In the present chapter, the frequency response of the system will be studied. Minimum damping will be determined for a given maximum response allowance.

If a rotor is unbalanced with an eccentricity of e , the translational displacement of the rotor gravity center r_C can be expressed as

$$r_C = r + (me)e^{i\Omega t} \quad (4.1)$$

where m is the rotor mass.

Similarly, the tilting angle of a rotor with an initial tilt ϕ_0 can be written as

$$\phi_C = \phi + \phi_0 e^{i\Omega t} \quad (4.2)$$

It is noted that r and ϕ in the preceding two equations are respective shaft (or bands, if appropriate) translation and slope.

A derivation similar to that for equations (2.2a) and (2.2b) gives the following two equations

$$F = -m\ddot{r}_C \quad (4.3)$$

$$M = -I_m \ddot{\phi}_C + i J_m \Omega \dot{\phi}_C \quad (4.4)$$

where F and M are respective force and moment applied on the shaft.

Inserting equations (4.1) and (4.2) into equations (4.3) and (4.4), respectively, one obtains

$$F = -m\ddot{r} + m\Omega^2 e^{i\omega t} \quad (4.5)$$

$$M = -I_m \ddot{\phi} + i J_m \Omega \dot{\phi} + (I_m - J_m) \phi_0 \Omega^2 e^{i\omega t} \quad (4.6)$$

The shaft at the position where external damper is located receives the following force F_d :

$$F_d = -m_d \ddot{r}_d - C_d \dot{r}_d$$

The compliance equations can be written in matrix form as follows:

$$\{q_i\} = [\alpha_{ij}]\{Q_j\} \quad i, j = 1, 2, \dots, 7 \quad (4.8)$$

where $\{q_i\} \equiv \{r_r, \phi_r, r_h, \phi_h, r_t, \phi_t, r_d, \phi_d\}^T$

$\{Q_j\} \equiv \{F_r, M_r, F_h, M_h, F_t, M_t, F_d, M_d\}^T$

and $\{\alpha_{ij}\}$ are given in Appendix E.

Due to the geometric configuration of the Sandia Flywheel System it is expected that unbalance and initial tilt mostly occur in the rim. In view of this, frequency response excited by such kinds of geometric imperfections are studied. However, such studies could be extended to incorporate similar excitation received from other components, if necessary or important.

Inserting equations (4.5) and (4.6) into equation (4.8), and using the following solution form

$$\{q_i\} = \{\bar{q}_i\} e^{i\Omega t} \quad (4.9)$$

one obtains

$$\{[K_{ij}] + [N_{ij}]\Omega - [M_{ij}]\Omega^2\} \{\bar{q}_i\} = \{f_j\} \quad (4.10)$$

where $[K_{ij}] \equiv [\alpha_{ij}]^{-1}$, $[M_{ij}]$ and $[N_{ij}]$ have zero elements except the following

$$\begin{aligned} M_{11} &= m_r & ; & & M_{22} &= I_{mr} - J_{mr} & ; & & M_{33} &= m_h \\ M_{44} &= I_{mh} - J_{mh} & ; & & M_{55} &= m_t & ; & & M_{66} &= I_{mt} - J_{mt} \\ M_{77} &= m_d & ; & & M_{88} &= I_{md} - J_{md} & ; & & N_{77} &= iC_d, \end{aligned} \quad (4.11)$$

$\{f_j\}$ is the excitation vector and is given below

$$\{f_j\} = \{e_r m_r \Omega^2, \phi_{or} (I_{mr} - J_{mr}) \Omega^2, 0, 0, 0, 0, 0, 0\}^T \quad (4.12)$$

Equation (4.10) is a set of nonhomogeneous linear algebraic equations in terms of the responses.

4.2 Numerical Results

Solving equation(4.10) on an IBM 370, Model 158J digital computer, one obtains the responses as a function of the rotational speeds. The responses induced by rim eccentricity are presented in Figures 4.1 and 4.2 for three different viscous damping coefficients. For $C_d = 0$ (in units of lb-sec/in. hereafter), the amplitudes become unbounded. It is interesting to see that excellent agreements, as far as the first-order critical speeds concerned, are obtained between Figures 4.1, 4.2 and Figure 2.1 of Chapter II. It can be seen that larger responses are obtained in the lowest critical speed compared to that in the two otherwise higher critical speeds. However, the former is less important since the design operating speed is in the range of 8,000 rpm and up. The responses induced by rim initial tilt are presented in Figures 4.3 and 4.4. Again good agreements are obtained between Figures 4.3, 4.4 and Figure 2.1. In contrast to the response curves presented in Figures 4.1 and 4.2, the larger responses occur in the third critical speed.

In the Sandia design, there is a "stop" installed in the system, which limits the hub translation to a maximum of 0.0283 inches. In order to prevent the hub from hitting the "stop", an adequate amount of external damping should be present. According to the information provided by Sandia Laboratories, the maximum rim eccentricity and initial tilt pertinent to their designs are respectively 0.028 inches and 0.15 degrees. In other words, the maximum allowable ratios of the hub translation to rim eccentricity and initial tilt are respectively 1 and 12 in/rad. A plot of the ratio of the hub translational amplitude to rim eccentricity versus rotational speed is shown in Figure 4.5. It can be seen that the minimum amount of

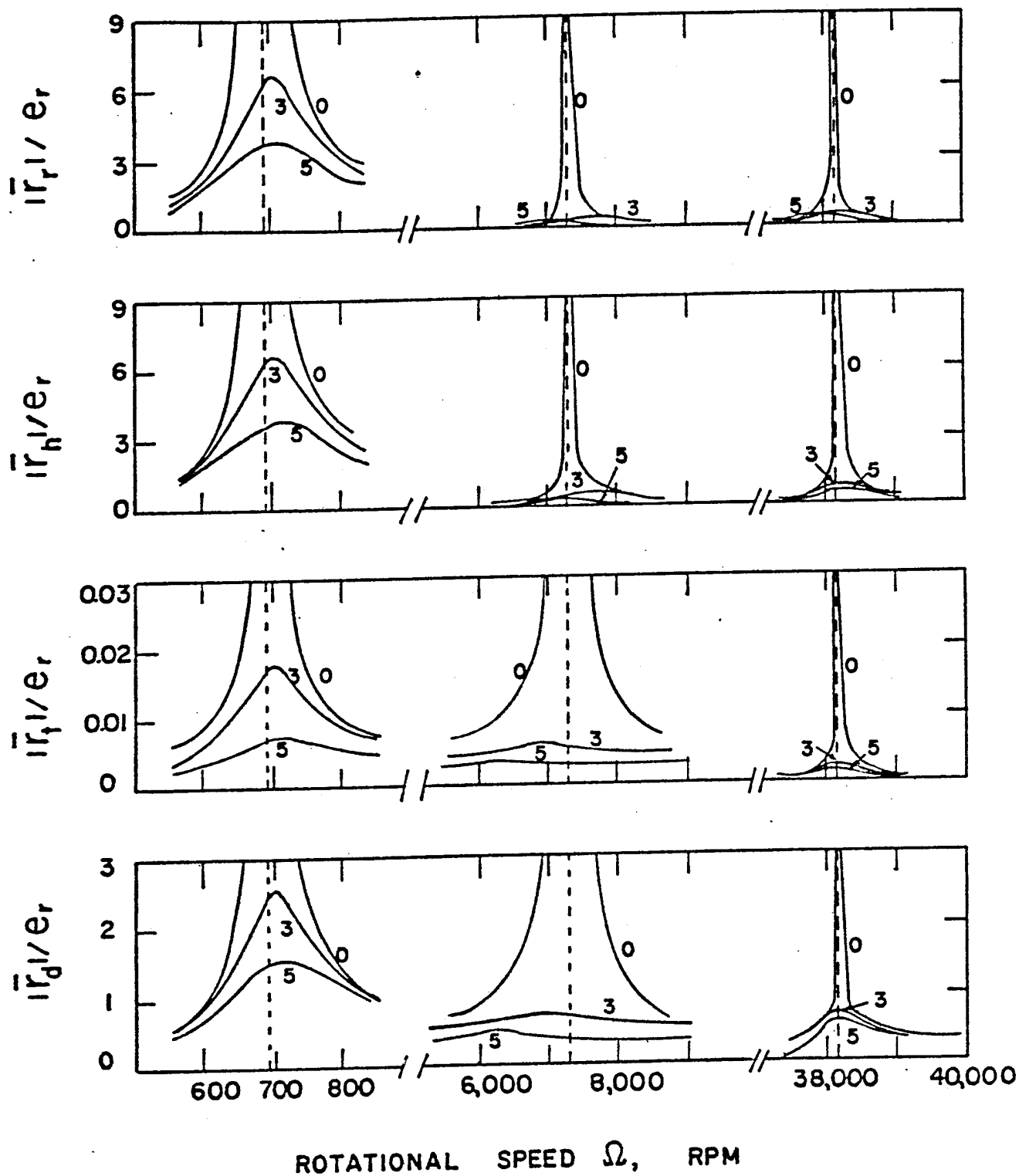


Fig. 4.1 Ratios of translational amplitude to rim eccentricity for $C_d = 0, 3$, and 5 lb-sec/in.

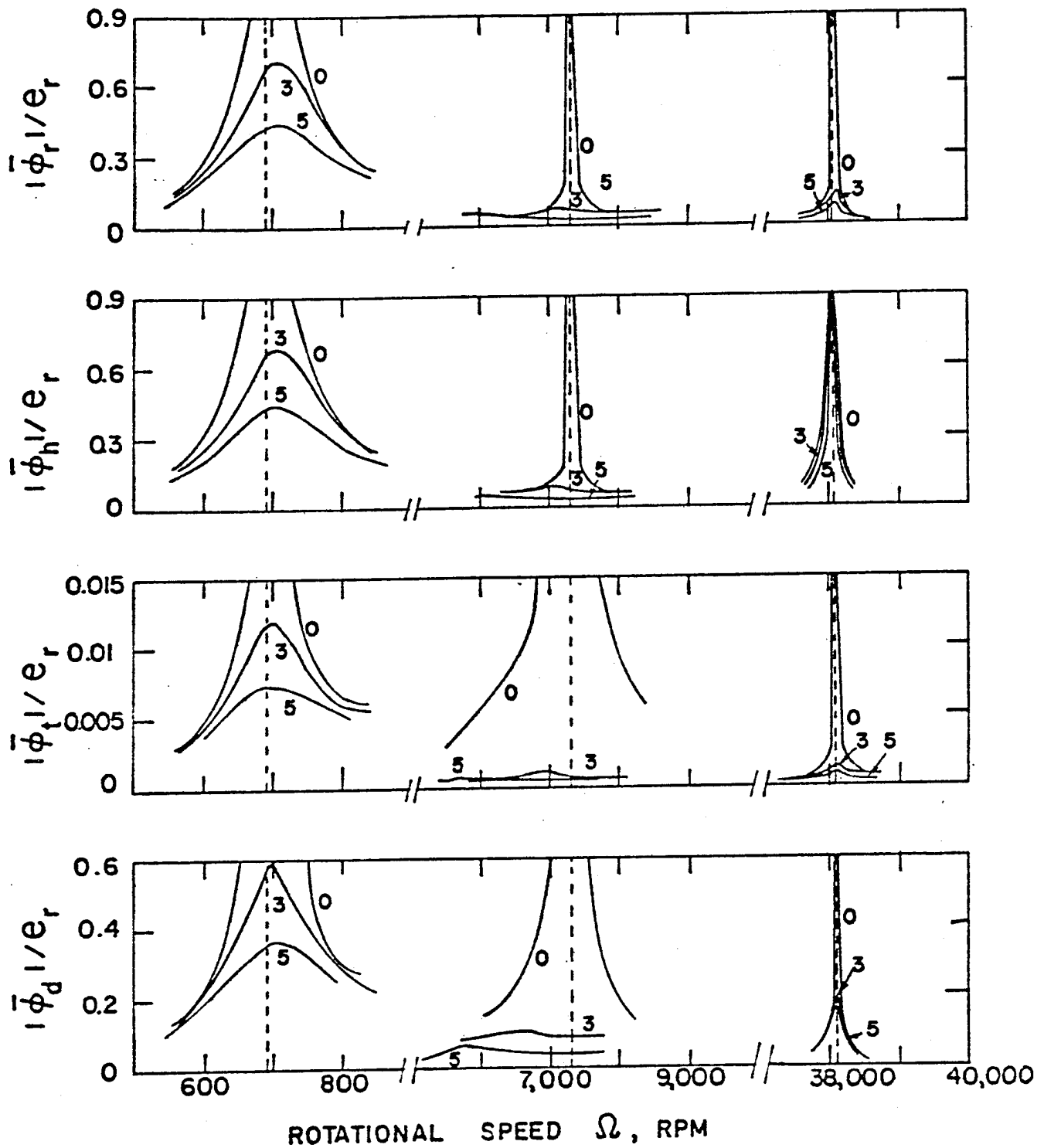


Fig. 4.2 Ratios of tilt amplitude to rim eccentricity for $C_d = 0, 3,$
and 5 lb-sec/in.

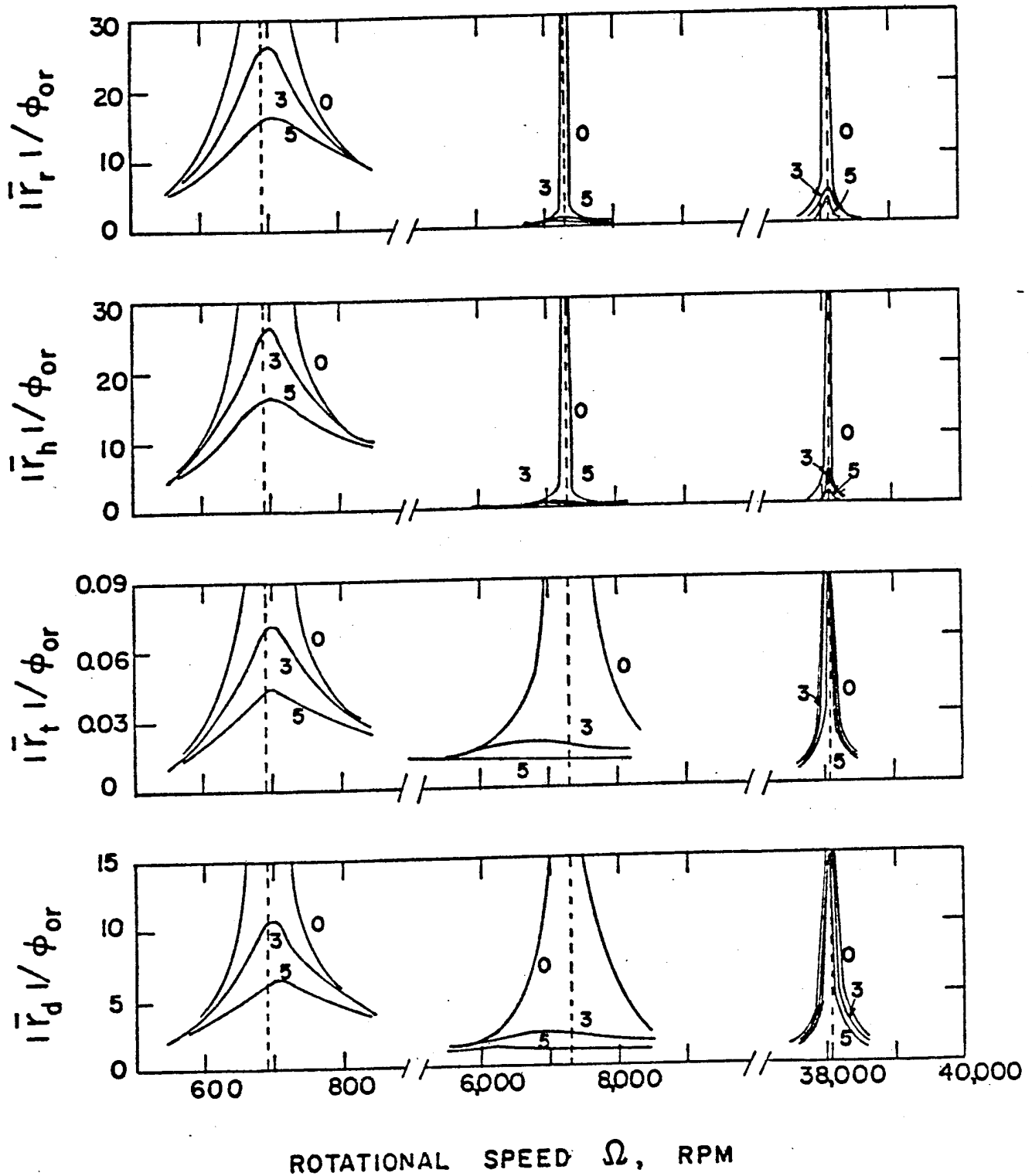


Fig. 4.3 Ratios of translational amplitude to rim initial tilt for

$C_d = 0, 3, \text{ and } 5 \text{ lb-sec/in.}$

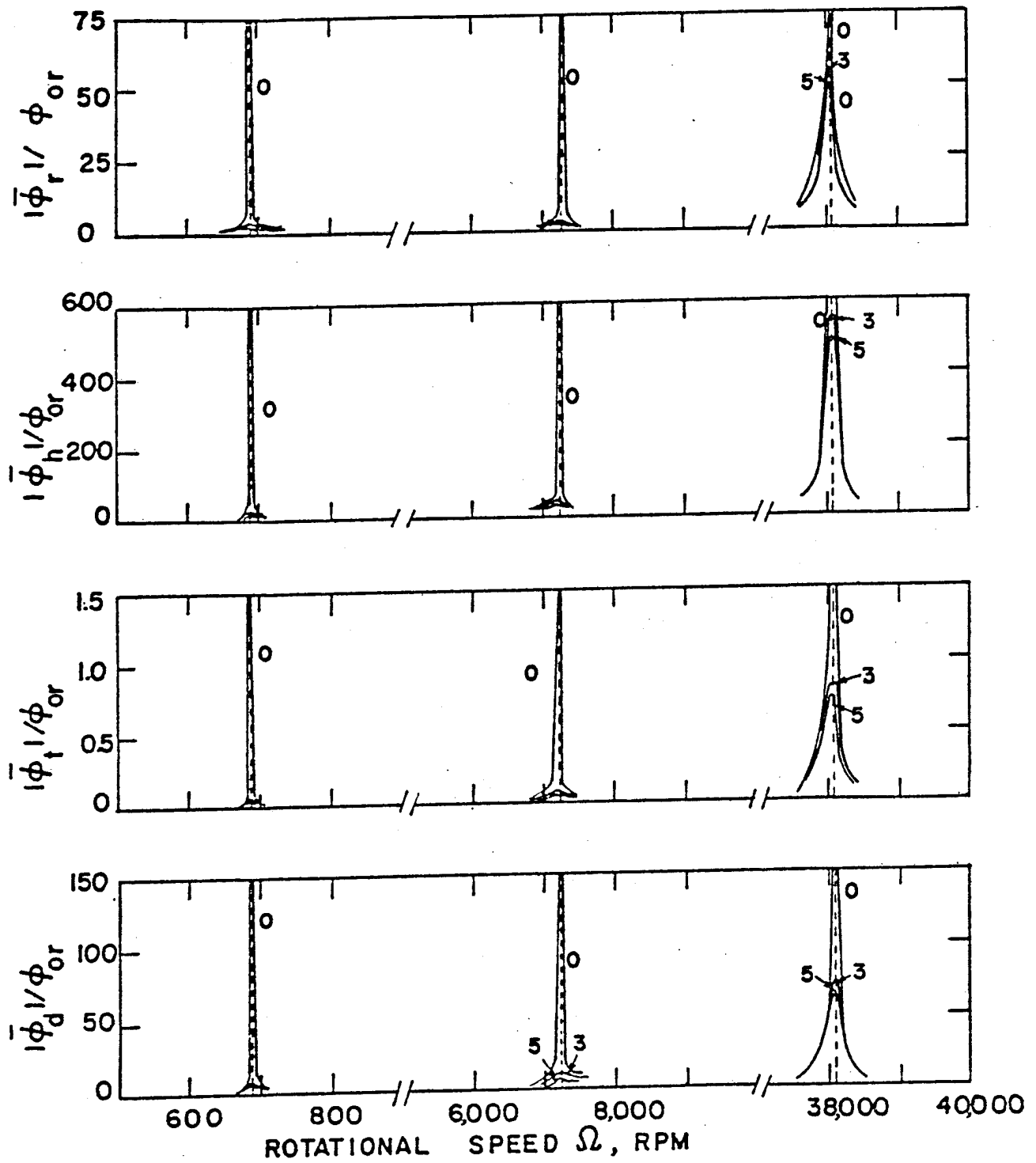


Fig. 4.4 Ratios of tilt amplitudes to rim initial tilt for $C_d = 0$, 3, and 5 lb-sec/in.

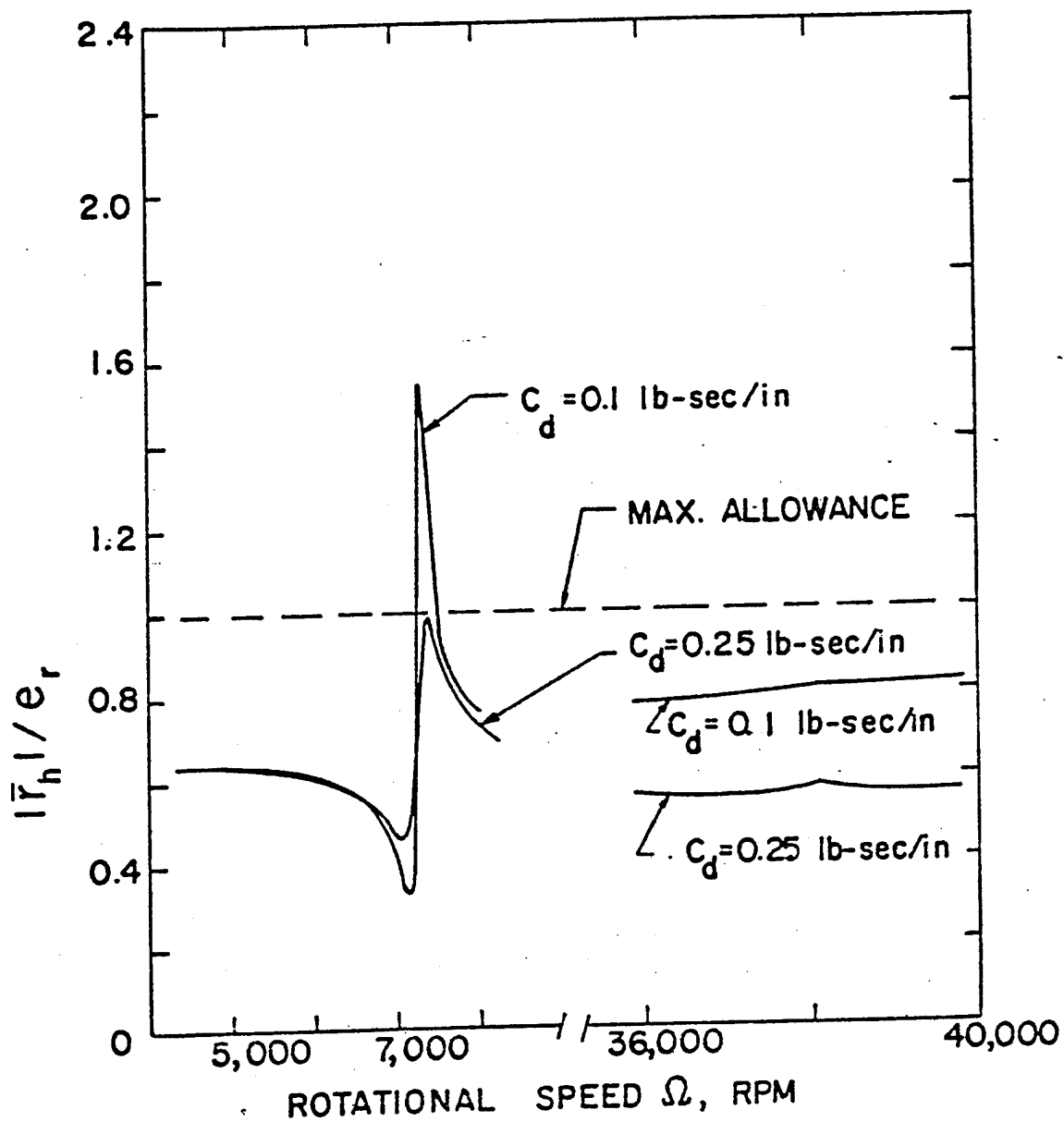


Fig. 4.5 Ratio of hub translational amplitude to rim eccentricity.

viscous damping coefficient required is 0.25 lb-sec/in (as discussed in the preceding chapter, this value is sufficient to maintain a stable motion up to 38,100 rpm). As a check, a plot of the ratio of the hub translational amplitude to rim initial tilt is shown in Figure 4.6. It can be seen that the peak responses for $C_d = 0.25$ lb-sec/in are well below the maximum allowance (12 in/rad). The hub translational responses induced by the rim eccentricity and initial tilt versus rotational speed are given in Figure 4.7. Again, a value of 0.25 lb-sec/in for C_d is sufficient to prevent the hub from hitting the "stop".

A conservative estimation of viscous damping coefficient C_d is presented in Appendix F. Considering the worst case as shown in Figure 4.7. at $\Omega = 38,100$ rpm, the corresponding damper lateral translation is 0.051 in. The damper clearance pertinent to the Sandia spin-test facility is 0.040 in. This gives a value of more than unity for the eccentricity ratio; which is not physically possible, since the eccentricity ratio can not exceed a value of one. However, according to the calculation conducted in Appendix F, the viscous damping coefficient should exceed 0.25 lb-sec/in when $\epsilon \approx 0.65$ or a damper displacement of about 0.026 in. For an eccentricity $\epsilon = 0.9$, Appendix F lists $C_d = 1.3$ lb-sec/in. Since this value is considerably greater than the 0.25 lb-sec/in value on which Fig. 4.7 is based, it is clear that the 0.051-in. damper displacement mentioned above would be considerably reduced for $C_d = 1.3$ lb-sec/in. and there would be no danger of the damper hitting its housing.

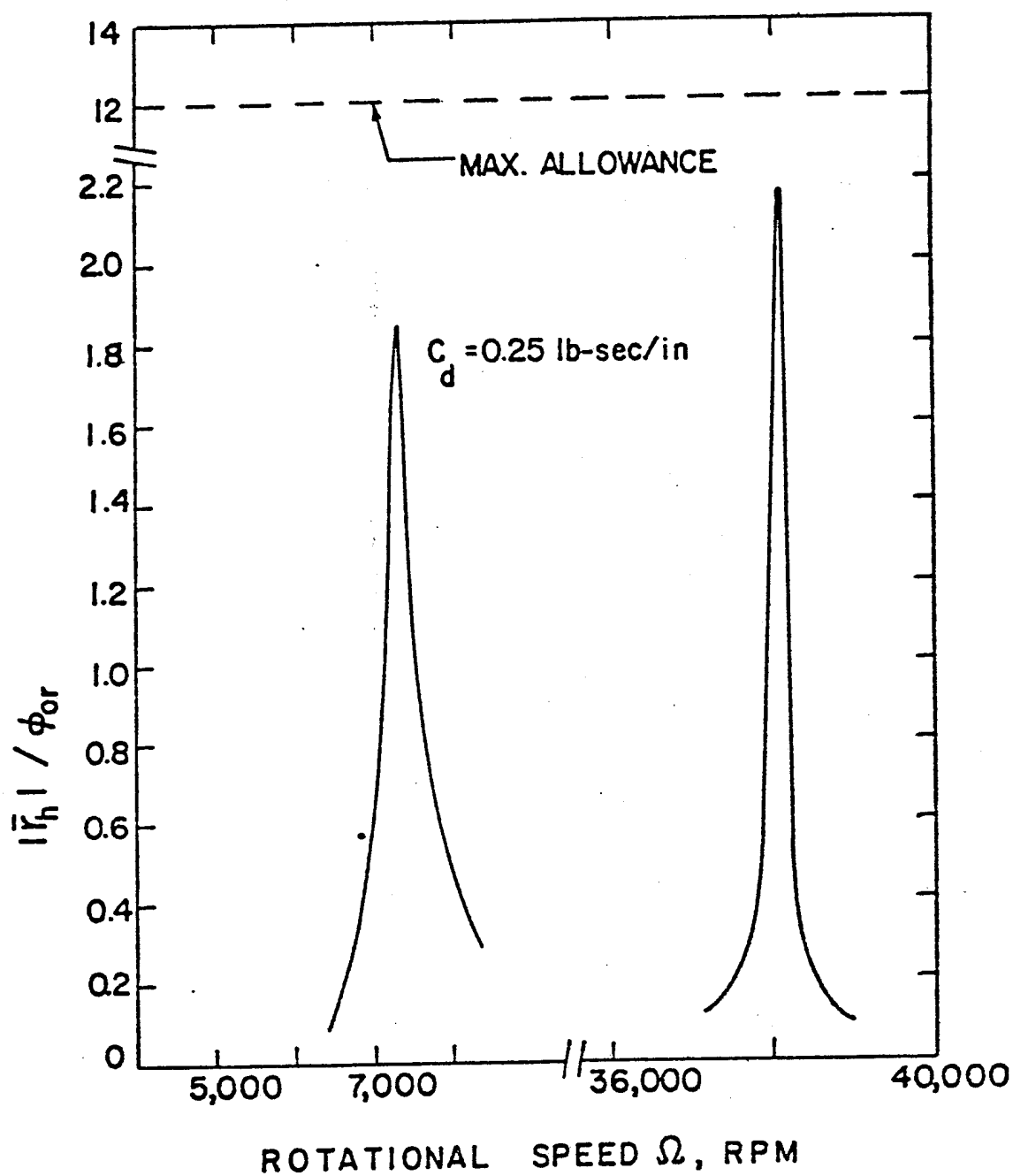


Fig. 4.6 Ratio of hub translational amplitude to rim initial tilt.

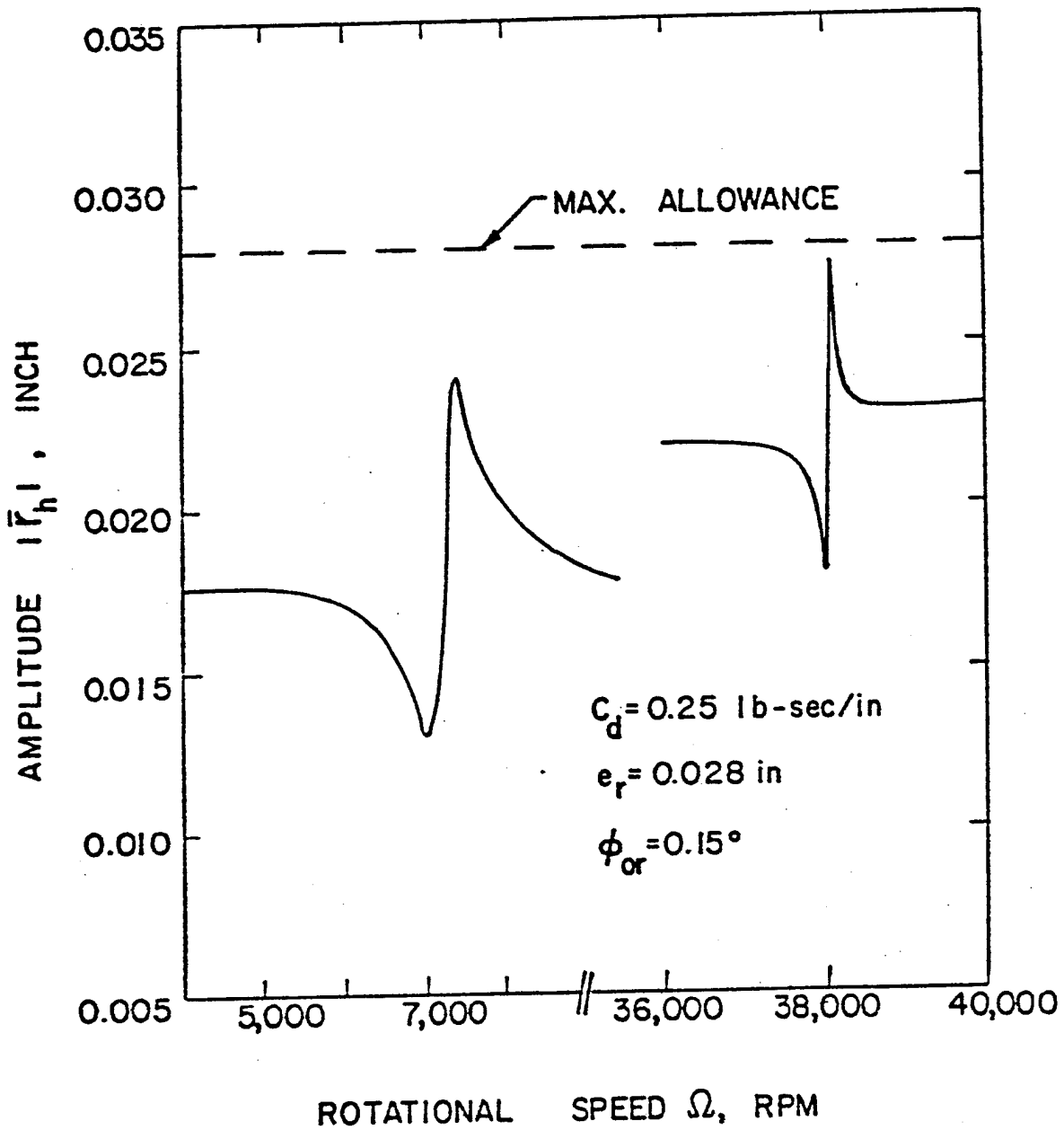


Fig. 4.7 Hub translational amplitude versus rotational speed.

CHAPTER V

COMPARISON WITH EXPERIMENTAL RESULTS

In the spin tests of the two Sandia flywheel systems (denoted here as Systems A and B) tested by Sandia personnel at the Sandia Livermore Laboratory [31], x and y coordinates of the hub position in the horizontal plane were picked up by proximity gages and displayed on an oscilloscope.

The System A flywheel displayed considerable vibrational amplitude in the low-speed range below about 2,000 rpm, but it was possible to accelerate through this speed range. (The excessive amplitude may have been indicative of the predicted critical speeds in the vicinity of 700 and 2,000 rpm.) Starting at about 14,000 rpm, there was a gradually increasing buildup in amplitude which accelerated rapidly starting at 18,000 rpm. Especially sudden increases in amplitude were noted at 20,200 rpm and 20,900 rpm. These sudden jumps while the rotational speed was gradually increased appeared to be indicative of the nonlinear jump phenomenon associated with a "softening" restoring force [35]. It is also possible that these sudden increases were due to any one of these causes: (1) sudden failure of a band, (2) slippage of the bands in the vicinity of the hub, or (3) rapid opening of a delamination in the rim. The flywheel shaft broke due to excessive amplitude when a speed of approximately 22,100 rpm was reached.

By ultrasonic and radiographic means it had been found prior to the spin test that this particular flywheel rim appeared to have some localized areas of fiber buckling. An earlier test of another flywheel of the System A design had achieved 17,900 rpm before the lead balance weights

were thrown off and the test stopped. Surface flaws, but no significant internal flaws, were detected in it prior to test, and post-failure examination showed that it had separated in the vicinity of the surface irregularity.

In summary, it appears that the calculated fourth-mode, second-order forward critical speed of 24,200 rpm for System A is in good agreement with the observed failure due to excessive amplitude at 22,100 rpm. This agreement was surprising, since all of the stiffness values used were calculated ones, some of which were based on boundary condition assumptions which may not have been sufficiently realistic.

The System B flywheel exhibited a generally smoother ride (less vibrational amplitude) than did System A. A possible explanation for this could be the inherently more symmetric stiffness distribution of the band geometry in System B. Pronounced sudden decreases in amplitude, indicative of nonlinear jump phenomena associated with a "hardening" restoring force [35] were observed at approximately 22,000 rpm and 24,800 rpm. There was a gradual increase in amplitude starting at about 27,500 rpm, with sudden increases in amplitude at approximately 29,000 rpm and 30,000 rpm. There was a loud report associated with the first of these, and final failure was at 30,100 rpm. Post-failure examination of this flywheel indicated that the rim still retained its structural integrity, but many of the bands had failed near their attachment to the rim. It is not known which of the following phenomena directly caused failure of these bands: (1) snapping of some of the bands due to excessive steady centrifugal and aerodynamic loads, (2) excessive dynamic mechanical loads resulting from the system dynamics causing the bands to snap, or (3) excessive abrasion due to

rubbing after the flywheel dropped into the spin pit following failure of the reduced-section breakaway shaft. An earlier test of the System B design had displayed dynamic instability at 29,000 rpm and the test was discontinued at that point.

In summary, it appears that the calculated fourth-mode, second-order forward critical speed of 24,250 rpm for System B was not associated with the excessive amplitudes, during spin tests, in the vicinity of 29,000-30,000 rpm. However, there is a calculated first-order forward critical speed for the second mode (associated with flywheel shaft rotary flexibility) at approximately 38,000 rpm. It may be tentatively conjectured that the System A flywheel failed at a second-order critical speed (22,000 rpm) due to stiffness asymmetry of the bands, while System B, could have gotten beyond this speed only to encounter excessive amplitude at the next higher first-order critical speed (30,000⁺ rpm).

CHAPTER VI

CONCLUDING REMARKS AND SUGGESTIONS FOR FURTHER RESEARCH

In this investigation, free whirling, forced whirling, and stability of two rim-type composite-material flywheel systems currently under development and spin test at Sandia Laboratories were studied.

Critical speeds were encountered in the design operating speed range (8,000 rpm to 31,500 rpm). For System A, perhaps the most important critical speed is the second-order forward one at the fourth mode (approximately 24,000 rpm). Practical way to increase such a critical speed beyond the desired maximum operating speed is to increase the band angle and the flywheel-shaft and turbine-shaft area moments of inertia (or to decrease the lengths of the these shafts since the purpose is to increase the shaft rotatory stiffness) simultaneously. For System B, the most important critical speed is less certain. However, there is a distinct possibility that it could be a first-order forward one at the second mode (approximately 38,100 rpm). This critical speed can be moved up by either reducing the hub diametral mass moment of inertia or increasing the flywheel-shaft area moment of inertia (or reducing the length of this shaft).

The adverse effect of material internal damping on the system stability can be overcome by providing an adequate external damper. Only a small value of viscous damping coefficient is required to stabilize the system up to the first critical speed at the second mode. However, a considerable amount of external damping is required to stabilize the system above this critical speed. Alternatively, this onset of instability can be moved up by either reducing the hub diametral mass moment of

inertia or increasing the area moment of inertia (or reducing the length) of the flywheel shaft.

In order to prevent the hub translational motion from hitting the "stop" during forced whirling excited by unbalance and initial tilt, a minimum viscous damping coefficient of 0.25 lb-sec/in is required for the Sandia flywheel designs.

Several new questions have arisen from this research and it is recommended that the following additional research be conducted:

1. In view of the "nonlinear" jump phenomenon observed during spin test, nonlinearity arising from the band action, believed to be the most significant one in the systems investigated, should be examined.
2. There exists a possibility for the band on the compressive side of the bend to buckle in the double-band action associated with rim tilt action relative to the hub.
3. The stacking sequence of bands which causes unsymmetric stiffness distribution circumferentially may be significant to the stability of the system. An investigation on this unsymmetric band stiffness distribution may provide some information pertinent to the excitation for the second-order critical speeds in System A.

REFERENCES

1. Lawson, L. T., "Design and Testing of High Energy Density Flywheels for Application to Flywheel/Heat Engine Hybrid Vehicle Drives", Proceedings of the 6th Intersociety Energy Conversion Engineering Conference, 1971, pp. 1142-1150.
2. "Introduction to the ERDA Electric and Hybrid Vehicle Demonstration Project", Division of Transportation Energy Conservation, ERDA, Mar. 1, 1977.
3. Proceedings of the 1975 Flywheel Technology Symposium, Berkeley, CA, Nov. 10-12, 1975, U. S. Government Printing Office, ERDA 76-85, 1976.
4. Proceedings of the 1977 Flywheel Technology Symposium, San Francisco, CA, Oct. 5-7, 1977, available from National Technical Information Service as CONF-771053.
5. Biggs, F., "Flywheel Energy Systems", Sandia Laboratories, Albuquerque, NM, Report SAND 74-0113, Nov., 1974.
6. Proceedings of the Hybrid Vehicle Interest and Capability Assessment Workshop, Albuquerque, NM, Sept. 22-23, 1976, Sandia Laboratories, SAND 76-0645, Mar., 1977.
7. Rockwell International Space Division, "Economic and Technical Feasibility Study for Energy Storage Flywheels", U. S. Government Printing Office, Report ERDA 76-65, Dec., 1975.
8. U. S. Patent No. 3,698,262, D. W. Rabenhorst, inventor, Oct. 17, 1972.
9. Morganthaler, G. F. and Bonk, S. P., "Composite Flywheel Stress Analysis and Materials Study", Advances in Structural Composites (Proc. 12th. Annual SAMPE Symposium, Oct. 10-12, 1967), Paper D-5.
10. Bert, C. W., "Centrifugal Stresses in Arbitrarily-Laminated, Rectangular-Anisotropic Circular Disks", Journal of Strain Analysis, Vol. 10, Apr., 1975, pp. 84-92.
11. Post, R. F. and Post, S. F., "Flywheels", Scientific American, Vol. 229, No. 6, Dec., 1973, pp. 17-23.
12. Bert, C. W., "Dynamic Problems in Composite-Material Flywheels for Energy Storage in Hybrid Vehicles", oral presentation at the 47th Shock and Vibration Symposium, Albuquerque, NM, Oct. 12-21, 1976.
13. Biezeno, C. B. and Grammel, R., Engineering Dynamics, Vol. III: Steam Turbines, Blackie and Son Ltd., London, 1954.

REFERENCES (Cont'd.)

14. Hartog, J. P. den, Mechanical Vibrations, 4th ed., McGraw-Hill, New York, 1956.
15. Dimentberg, F. M., Flexural Vibrations of Rotating Shafts, transl. from Russian, Butterworth, London, 1961.
16. Loewy, R. G. and Piarulli, V. J., "Dynamics of Rotating Shafts", Shock and Vibration Information Center, Monograph SVM-4, 1969.
17. McKinnon, C. N., Jr., "Rotor Dynamic Analysis", Appendix B of "Evaluation of Selected Drive Components for a Flywheel Powered Commuter Vehicle", LMC Corp., Final Report, Contract EY-76-C-0301164, Phase I, Jun. 30, 1977.
18. Reedy, E. D., Jr., "A Composite-Rim Flywheel Design", SAMPE Quarterly, Vol. 9, No. 3, pp. 1-6.
19. Boyce, L. and Kozik, T. J., "Deterministic and Probabilistic Foundation Forces Resulting from an Unbalanced Turbine", ASME Paper 76-GT-120, Mar., 1976.
20. Bert, C. W. and Chen, T. L. C., "On Vibration of a Thick Flexible Ring Rotating at High Speed", Journal of Sound and Vibration (to be published).
21. Stodola, A., "New Critical Shaft Speeds as Effects of the Gyroscopic Disc-Action", Engineering, Vol. 106, Dec. 13, 1918, pp. 665-666.
22. Stodola, A., Steam and Gas Turbines, Vol. 2, transl. from German, McGraw-Hill, New York, 1927, pp. 1113-1122.
23. Green, R. B., "Gyroscopic Effects on the Critical Speeds of Flexible Rotors", Journal of Applied Mechanics, Vol. 15, Trans ASME, Vol. 70, Dec., 1948, pp. 369-376.
24. Chang, K. T., "Turbomachine Dynamics", Wright Air Development Center, WADC TR 57-611, Document No. AD-151087, Apr., 1958.
25. Blcak, H. F., "Lateral Vibration of Shafts Having Radial Symmetry and Appreciable Gyro-Action", Journal of Mechanical Engineering Science, Vol. 6, Mar. 1964, pp. 53-63.
26. Gourlay, A. R. and Watson, G. A., Computational Methods for Matrix Eigenproblems, John Wiley & Sons, London, 1973, Chapter 14.
27. Pedersen, P. T., "On Self-Excited Whirl of Rotors", Ingenieur-Archiv, Vol. 42, 1973, pp. 267-284.

REFERENCES (Cont'd)

28. Yamada, Y., "On the Critical Speeds of a Rotor System Having an Asymmetrical Disk", Proc. 4th Japan National Congress of Applied Mechanics, 1954, pp. 381-384.
29. Thomson, W. T., Younger, F. C., and Gordon, H. S., "Whirl Stability of the Pendulously Supported Flywheel System", Journal of Applied Mechanics, Vol. 44, Trans. ASME, Vol. 99E, June, 1977 pp. 322-328.
30. Leissa, A. W., "On a Curve Veering Aberration", Journal of Applied Math. and Physics (ZAMP), Vol. 25, 1974, pp. 99-111.
31. Reedy, E. D., Jr. and Street, H. K., "Composite-Rim Flywheels", Sandia Laboratories, Albuquerque, NM, to be published.
32. Gunter, E. J., "Dynamic Stability of Rotor-Bearing Systems", NASA, SP-113, 1966.
33. Lund, J. W., "Some Unstable Whirl Phenomenon in Rotating Machinery", The Shock and Vibration Digest, Vol. 7, No. 6, Naval Research Laboratory, Washington, D. C., Jun., 1975.
34. Kimball, A. L., "Internal Friction Theory of Shaft Whirling", General Electric Review, Vol. 27, No. 4, Apr., 1924, pp. 244-251.
35. Hayashi, C., Nonlinear Oscillations in Physical Systems, McGraw-Hill, New York, 1964, p. 119.
36. Bert, C. W., "Deflections in Stepped Shafts", Machine Design, Vol. 32, No. 32, Nov. 24, 1960, pp. 128-133.
37. Cowper, G. R., "The Shear Coefficient in Timoshenko's Beam Theory", Journal of Applied Mechanics, Vol. 33, Trans. ASME, Vol. 88E, Jun., 1966, pp. 335-340.
38. Bansal, P. N. and Hibner, D. H., "Experimental and Analytical Investigation of Squeeze Film Bearing Damper Forces Induced by Offset Circular Whirl Orbits", Journal of Mechanical Design, Trans. ASME, Vol. 100, No. 3, July 1978, pp. 549-557.

APPENDIX A

DERIVATION OF ROTOR BASIC EQUATIONS INCLUDING GYROSCOPIC EFFECT

Consider an axisymmetric rotor as shown in Fig. A1. The rotor rotates at an rotational speed Ω with respect to axis z_1 which passes through the geometric center C of the rotor. Due to the symmetric nature of the rotor, coordinate system $x_1 y_1 z_1$ coincides with one of the principal axes of the rotor. Thus, the angular momentum \vec{H} of the rotor based on system $x_1 y_1 z_1$ is

$$H_{x_1} = I_m \dot{\phi}_x ; \quad H_{y_1} = I_m \dot{\phi}_y ; \quad H_{z_1} = J_m \Omega \quad (A-1)$$

Here I_m , J_m are mass moments of inertia of the rotor respectively about its diametral and axial directions, ϕ_x and ϕ_y are rotations of the rotor respectively in the xz and yz planes, H_{x_1} , H_{y_1} and H_{z_1} are components of \vec{H} in the $x_1 z_1$, $y_1 z_1$ and $x_1 y_1$ planes, $(\dot{}) = \partial()/\partial t$.

The angular momentum of the rotor based on system $x'y'z'$ can be obtained as follows by resolving the components in equations (A-1) and using the small-angle approximation.

$$\begin{aligned} H_{x'} &= I_m \dot{\phi}_x + J_m \Omega \phi_y \\ H_{y'} &= I_m \dot{\phi}_y - J_m \Omega \phi_x \\ H_{z'} &= J_m \Omega \end{aligned} \quad (A-2)$$

To the first-order approximation (small ϕ_x and ϕ_y), the Euler's equations of motion $\vec{M}_{xyz} = \dot{\vec{H}}_{xyz}$ are applicable and hence the following inertia couples are obtained

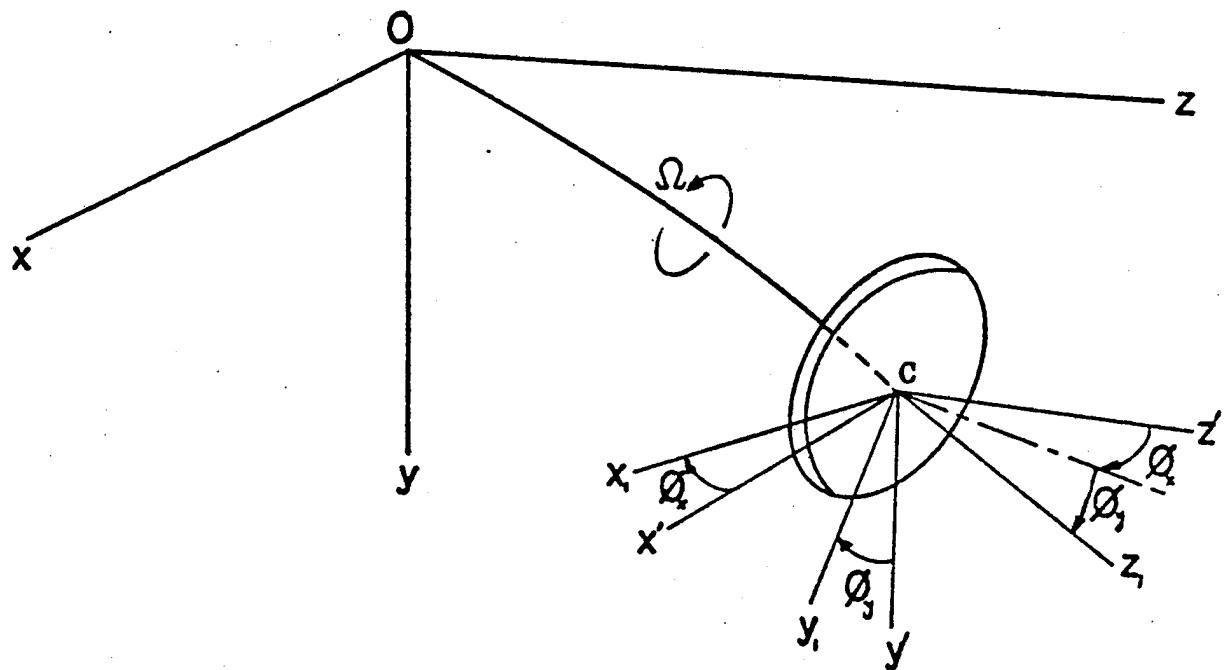


Fig. A1. Reference axes of a whirling rotor.

$$\begin{aligned} M_x &= \dot{H}_x = I_m \ddot{\phi}_x + J_m \Omega \dot{\phi}_y \\ M_y &= \dot{H}_y = I_m \ddot{\phi}_y - J_m \Omega \dot{\phi}_x \\ M_z &= \dot{H}_z = 0 \end{aligned} \tag{A-3}$$

Equations (A-3) represent the inertia couples applied on the rotor. The inertia couples applied on the shaft by the rotor are the reactions received as of equations (A-3). Thus, the nonzero couples applied on the shaft are

$$\begin{aligned} M_x &= -I_m \ddot{\phi}_x - J_m \Omega \dot{\phi}_y \\ M_y &= -I_m \ddot{\phi}_y + J_m \Omega \dot{\phi}_x \end{aligned} \tag{A-4}$$

The first terms on the right-hand sides of equations (A-4) are associated with rotatory inertia, while the second terms are associated with gyroscopic effects.

APPENDIX B

INTERACTION BETWEEN THE RIM AND BANDS

In this analysis, only the additional forces due to centrifugal action are determined. They add to the initial forces due to prestress during winding.

The free centrifugal expansion of a single band is calculated as follows (see Fig. B1 for detailed geometry). First, the centrifugal force developed at any arbitrary radius r_1 is determined by

$$P_{bc} = \int_{r_1}^{R_i} \rho_b A_b \Omega^2 r dr / \cos \bar{\phi} = \frac{1}{2} \rho_b A_b \Omega^2 (R_i^2 - r_1^2) / \cos \bar{\phi} \quad (B-1)$$

where R_i is the rim inside radius; $\bar{\phi}$ is defined in Fig. B1.

Thus, the axial strain of the band at r_1 is

$$\epsilon_b(r_1) = P_{bc} \cos \bar{\phi} / A_b E_b = (P_b \Omega^2 / 2 E_b) (R_i^2 - r_1^2) \quad (B-2)$$

The axial displacement at the outer edge of the band (i.e. at its point of attachment to the rim) is

$$u_{bo} = \int_{R_h}^{R_i} \epsilon_b(r_1) dr_1 = (\rho_b \Omega^2 / E_b) [(R_i^3/3) - (R_i^2 R_h/2) + (R_h^3/6)] \quad (B-3)$$

where R_h is the hub outside diameter.

For the rim, the hoop tension due to free centrifugal action is

$$N_{fc} = \rho A \Omega^2 R^2 \quad (B-4)$$

Thus, the radial displacement of the rim at its centroidal radius R is

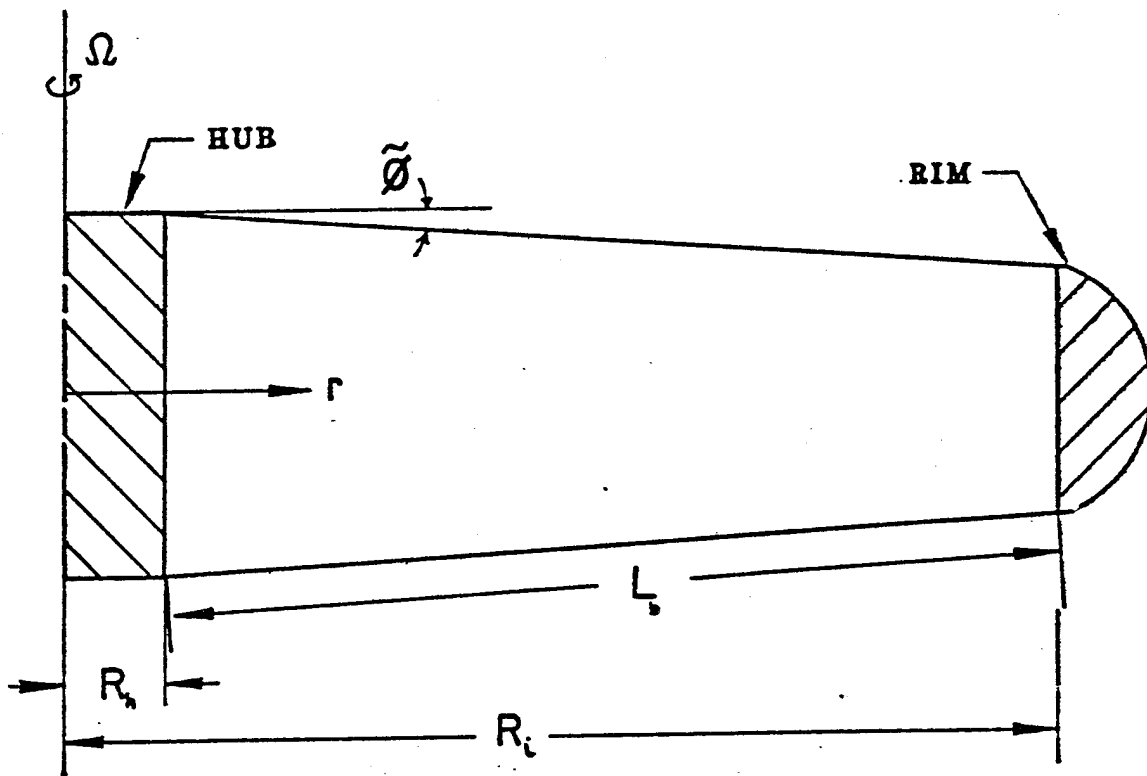


Fig. B1. Side elevation of one half of the Sandia thick-ring flywheel.

$$u_{rc} = \rho_r \Omega^2 R^3 / E \quad (B-5)$$

Comparison of the values of $u_{bo} \cos \phi$ (this is the band radial displacement at the outer edge) and u_{rc} using data pertinent to the present investigation, shows that the latter is greater than the former. Thus, the bands are loaded in tension. To determine the interaction between the two, we consider a typical "repeating section" as shown in Fig. B2.

A summation of radial forces yields the following expression

$$(Rf_R - N^\circ) \sin \theta_o = Q \cos \theta_o \quad (B-6)$$

where $N^\circ \equiv$ circumferential force, $Q \equiv$ shear force, and f_R is the centrifugal body force per unit length given by

$$f_R = \rho A R \Omega^2 \quad (B-7)$$

The elastic boundary conditions at the edges of the segment can be written as

$$N^\circ = K_\theta u_o, \quad Q = \frac{1}{2} K_{br} (u_o - u_{bo} \cos \phi) \quad (B-8)$$

where u_o is the radial displacement of the edge at $\theta = \theta_o$ and the stiffnesses are given by

$$K_\theta = AE/R, \quad K_{br} = (A_b E_b / L_b) \cos^2 \phi \quad (B-9)$$

where L_b is the unsupported span length of the band.

Combining equations (B-3), (B-6) through (B-9), one obtains

the following expression

$$u_o / \Omega^2 = \frac{\rho A R^2 \tan \theta_o + \rho_b A_b \cos^3 \phi [(R_i^3 / 3 - (R_i^2 R_h / 2) + (R_h^3 / 6)] / 2L_b}{(AE/R) \tan \theta_o + (A_b E_b / 2L_b) \cos^2 \phi} \quad (B-10)$$

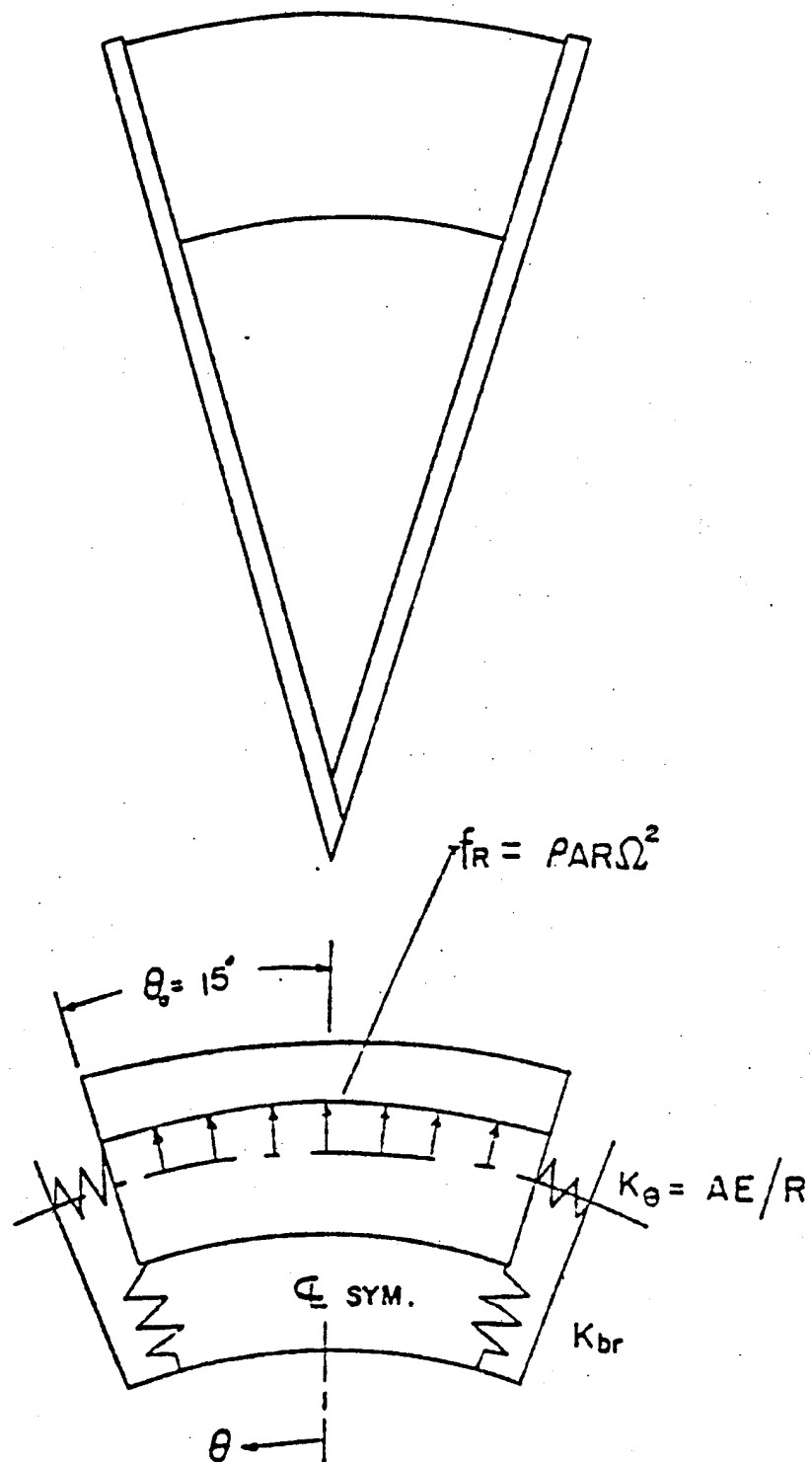


Fig. B2. A typical 30-degree repeating segment of rim and bands, and its schematic model

The additional radial force in a band due to the rim-band interaction is

$$Q = \frac{1}{2} K_{br} (u_o - u_{bo} \cos \bar{\phi}) \quad (B-11)$$

The additional tension in a band due to the rim-band interaction is

$$P_{bc}' = 2 Q \cos \bar{\phi} = K_{br} (u_o - u_{bo} \cos \bar{\phi}) \cos \bar{\phi} \quad (B-12)$$

The total tension in a band is the sum of $P_{bc} \cos \bar{\phi}$ and P_{bc}' . The former varies from zero at the outer edge to a maximum value at the inner edge. The integrated average of $P_{bc} \cos \bar{\phi}$ is

$$\bar{P} = \int_{R_h}^{R_i} \frac{1}{2} \rho_b A_b \Omega^2 (R_i^2 - r_1^2) dr_1 / (R_i - R_h) \quad (B-13)$$

Performing the integration, one can rewrite equation (B-13) as

$$\bar{P} = \rho_b A_b \Omega^2 (2 R_i^3 - 3 R_i^2 R_h + R_h^3) / 6(R_i - R_h) \quad (B-14)$$

Thus, the total centrifugal tension in a band is

$$P_c = \bar{P} + P_{bc}' \quad (B-15)$$

APPENDIX C

DETERMINATION OF IN-PLANE BAND STIFFNESS

A small in-plane displacement r_c (see Fig. C1) of the rim relative to the hub causes each band set (that is, the upper and lower bands which are shown superimposed in the figure) not only to stretch along its axial direction but also to bend in the plane containing the displacement r_c . The former produces the in-plane stretching rigidity; while the latter produces the in-plane flexural rigidity.

The amount stretched in the band set is

$$u_j = r_c \cos(\psi_j + \theta) \cos \bar{\phi} \quad (C-1)$$

where θ is the angle between the displacement direction and the nearest band having additional tension and ψ_j is the angle (measured in the same direction) between that nearest band and the j^{th} band.

Thus the axial force in a band set is

$$P_{Aj} = 2(P_i + P_c + \frac{A_b E_b}{L_b} u_j)$$

or

$$P_{Aj} = 2[P_i + P_c + \frac{A_b E_b}{L_b} r_c \cos(\psi_j + \theta) \cos \bar{\phi}] \quad (C-2)$$

where both P_i and P_c are assumed to have the same value in all directions.

The force component in the direction of the displacement r_c is

$$\begin{aligned} P_{Hj} &= P_{Aj} \cos(\psi_j + \theta) \cos \bar{\phi} \\ &= 2[P_i \cos(\psi_j + \theta) + P_c \cos(\psi_j + \theta) + \frac{A_b E_b}{L_b} r_c \cos^2(\psi_j + \theta) \cos \bar{\phi}] \cos \bar{\phi} \end{aligned} \quad (C-3)$$

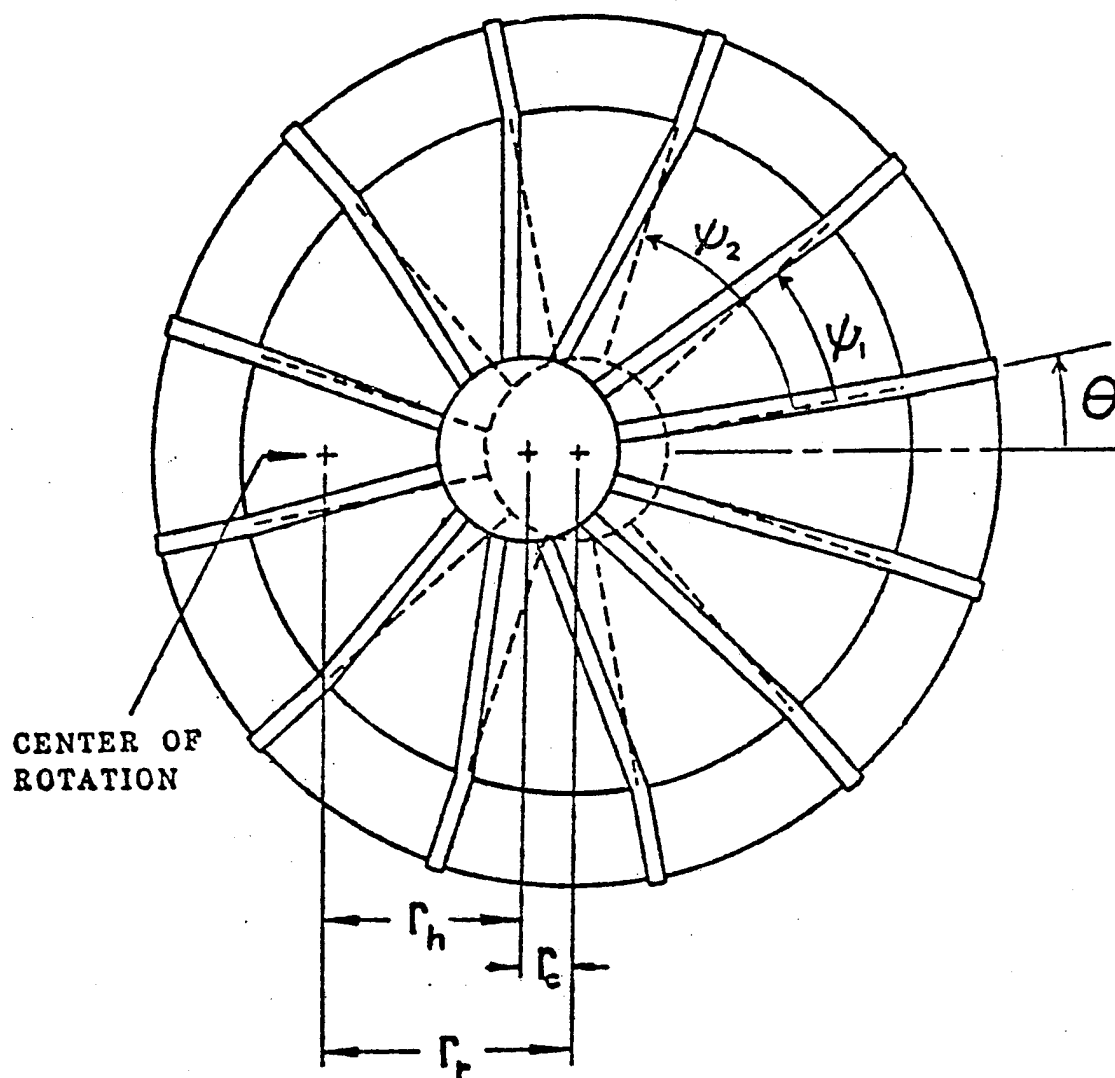


Fig. C1. In-plane translation of the rim relative to the hub.

The resultant restoring force is

$$P_H = \sum_{j=1}^{12} P_{Hj} = 2 \frac{A_b E_b}{L_b} r_c \cos^2 \phi \sum_{j=1}^{12} \cos^2 (\psi_j + \theta)$$

or

$$P_H = 12 \frac{A_b E_b}{L_b} r_c \cos^2 \phi \quad (C-4)$$

Thus, the integrated stiffness due to the variation of axial tension in the bands is

$$k_s = 12 \frac{A_b E_b}{L_b} \cos^2 \phi \quad (C-5)$$

The in-plane flexural rigidity k_b in the bands is the ratio of lateral force, applied on one end of the bands, to the side-sway deflection. Using classical beam-tension bar theory, one obtains

$$k_b = (k^2 \sinh kL_b) [2(1 - \cosh kL_b) + kL_b \sinh kL_b]^{-1} \quad (C-6)$$

where P is the total tension in each band; $k \equiv (P/E_b I_1)^{1/2}$; I_1 is the area moment of inertia of band cross-sectional area about its centroidal axis parallel to the flywheel shaft.

A set of bands parallel to the direction of load application can not carry any flexural load and thus does not contribute to the integrated flexural stiffness. However, a set of bands at 90° to the direction of loading contributes its in-plane flexural rigidity. For any given loading direction, the integrated in-plane flexural rigidity is given by

$$\begin{aligned}
 (k_b)_{\text{integrated}} &= 4[\cos^2 \theta + \cos^2 (30^\circ - \theta) + \cos^2 (30^\circ + \theta) \\
 &\quad + \cos^2 (60^\circ - \theta) + \cos^2 (60^\circ + \theta) + \cos^2 (90^\circ - \theta)] k_b \\
 &= 12 k_b
 \end{aligned}
 \tag{C-7}$$

The total integrated in-plane stiffness is

$$K_{bip} = 12 \left(\frac{A_b E_b}{L_b} \cos^2 \bar{\phi} + k_b \right)
 \tag{C-8}$$

In the Sandia System A flywheel, the average $\bar{\phi}$ is approximately equal to 2.66° . Using equation (C-8), one obtains only 0.2% less stiffness by incorporating the angle $\bar{\phi}$ as compared to the case when it is not incorporated.

For System B, the bands are wound flat on to the rim but undergo a 90-degree twist to be wound on to axially oriented pins at the hub. Bands in such systems are shown in Fig. C2(a). Application of equation (C-8) is not valid unless a modification is carried out. Physically the first term on RHS of equation (C-8), which is associated with stretching in axial direction, is unaffected. However, the second term should be decreased due to reduction of moment of inertia along x .

If the force applied at the right-hand side is Q as shown in Fig. C2(a), the moment distribution is

$$M(x) = -Q(L_b - x)
 \tag{C-9}$$

Using the same philosophy as presented in [36], the translational deflection at the point where Q is applied can be expressed as follows by neglecting the shear flexibility:

$$y_p = \int_0^{L_b} \left[\left(x \frac{\partial M}{\partial Q} \right) / E_b I(x) \right] dx
 \tag{C-10}$$

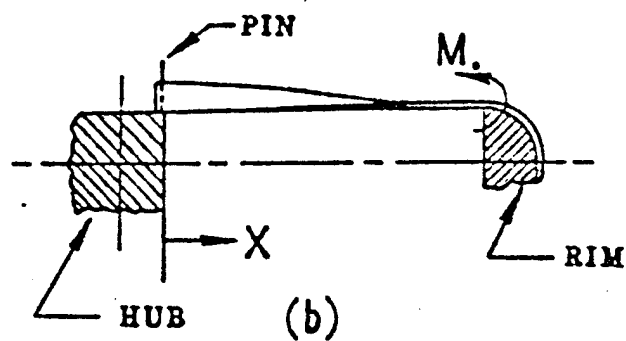
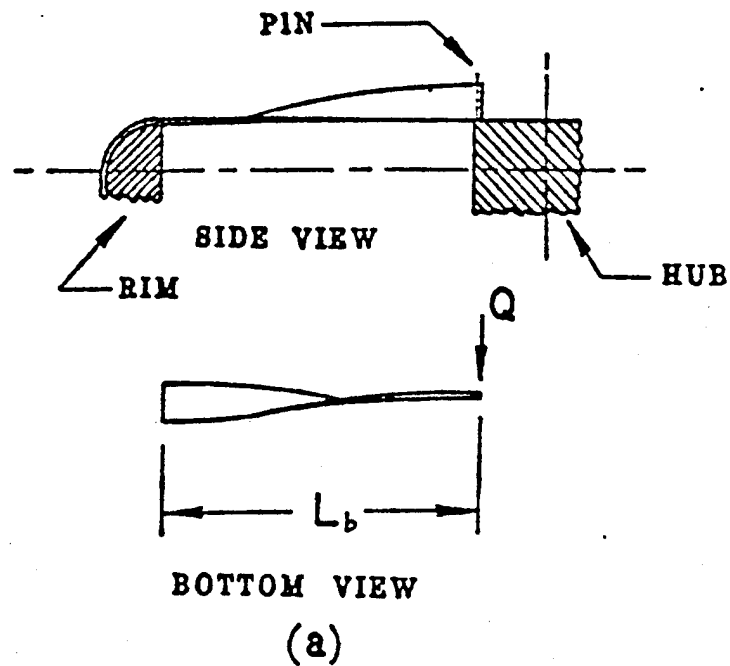


Fig C2. Schematic diagrams showing that the bands of System B have been twisted by an angle of $\pi/2$ at the end attached to the hub.

where $I(x)$ is the moment of inertia at position x .

Assuming that the angle twisted is linearly dependent on x , the following relation can be obtained

$$I(x) = I_1 \cos^2 \bar{x} + I_2 \sin^2 \bar{x} \quad (C-11)$$

where $\bar{x} \equiv \pi x / 2L_b$

Inserting equations (C-9) and (C-11) into equation (C-10), one obtains

$$(y_p/Q)_{\text{twisted}} = \int_0^{L_b} [(L_b - x)^2 / E_b (I_1 \cos^2 \bar{x} + I_2 \sin^2 \bar{x})] dx \quad (C-12)$$

For the case when the bands are not pre-twisted, the value of y_p/Q can be obtained by using the following equation.

$$(y_p/Q)_{\text{nontwisted}} = \int_0^{L_b} [(L_b - x)^2 / E_b I_1] dx \quad (C-13)$$

The ratio of the translational stiffness for the above two different configurations can be obtained as follows:

$$(K_b)_{\text{twisted}} / (K_b)_{\text{nontwisted}} = (y_p/Q)_{\text{nontwisted}} / (y_p/Q)_{\text{twisted}} \quad (C-14)$$

Combining equations (C-8) and (C-14), one can compute K_{bip} by using the following equation

$$K_{bip} = 12 \left(\frac{A_b E_b}{L_b} \cos^2 \phi + \frac{(y_p/Q)_{\text{nontwisted}}}{(y_p/Q)_{\text{twisted}}} k_b \right) \quad (C-15)$$

The numerical value of equation (C-14) pertinent to the Sandia System B design is approximately equal to 0.678. The angle ϕ in system

B is about 2.13° . Using these values in equation (C-15), one finds that the difference of K_{bip} for both Systems A and B is within 0.2%.

APPENDIX D

DETERMINATION OF OUT-OF-PLANE BAND STIFFNESS

To derive an expression for the out-of-plane band stiffness, it is necessary to consider a set of two bands as a double beam with column action on the compression side of the beam and tie-bar action on the tension side. Although there can be some geometric nonlinearity, only a linearized analysis is presented here. Fig. D1 shows schematically, in exaggerated fashion, the geometric relationships involved.

Denoting the upper band as band A and the lower one as band B, one can write the following expressions for the respective horizontal and vertical displacements of the band-to-rim junctions when the rim is tilted through an angle ϕ :

$$\begin{aligned} u_{AL} &= R_i(\cos \phi - 1) - b \sin \phi \approx -b\phi \\ w_{AL} &= R_i \sin \phi + b(\cos \phi - 1) \approx R_i \phi \\ u_{BL} &= R_i(\cos \phi - 1) + b \sin \phi \approx b\phi \\ w_{BL} &= R_i \sin \phi - b(\cos \phi - 1) \approx R_i \phi \end{aligned} \quad (D-1)$$

where the approximations at the right are based on the first-order small-angle assumptions, $\sin \phi \approx \phi$ and $1 - \cos \phi \approx 0$.

The total axial forces in the respective bands are

$$\begin{aligned} P_A &= P_i + P_c + A_b E_b (u_{AL} \cos \bar{\phi} - w_{AL} \sin \bar{\phi}) \phi / L_b \\ &\approx P_i + P_c - A_b E_b (b \cos \bar{\phi} + R_i \sin \bar{\phi}) \phi / L_b \\ P_B &= P_i + P_c + A_b E_b (u_{BL} \cos \bar{\phi} + w_{BL} \sin \bar{\phi}) \phi / L_b \\ &\approx P_i + P_c + A_b E_b (b \cos \bar{\phi} + R_i \sin \bar{\phi}) \phi / L_b \end{aligned} \quad (D-2)$$

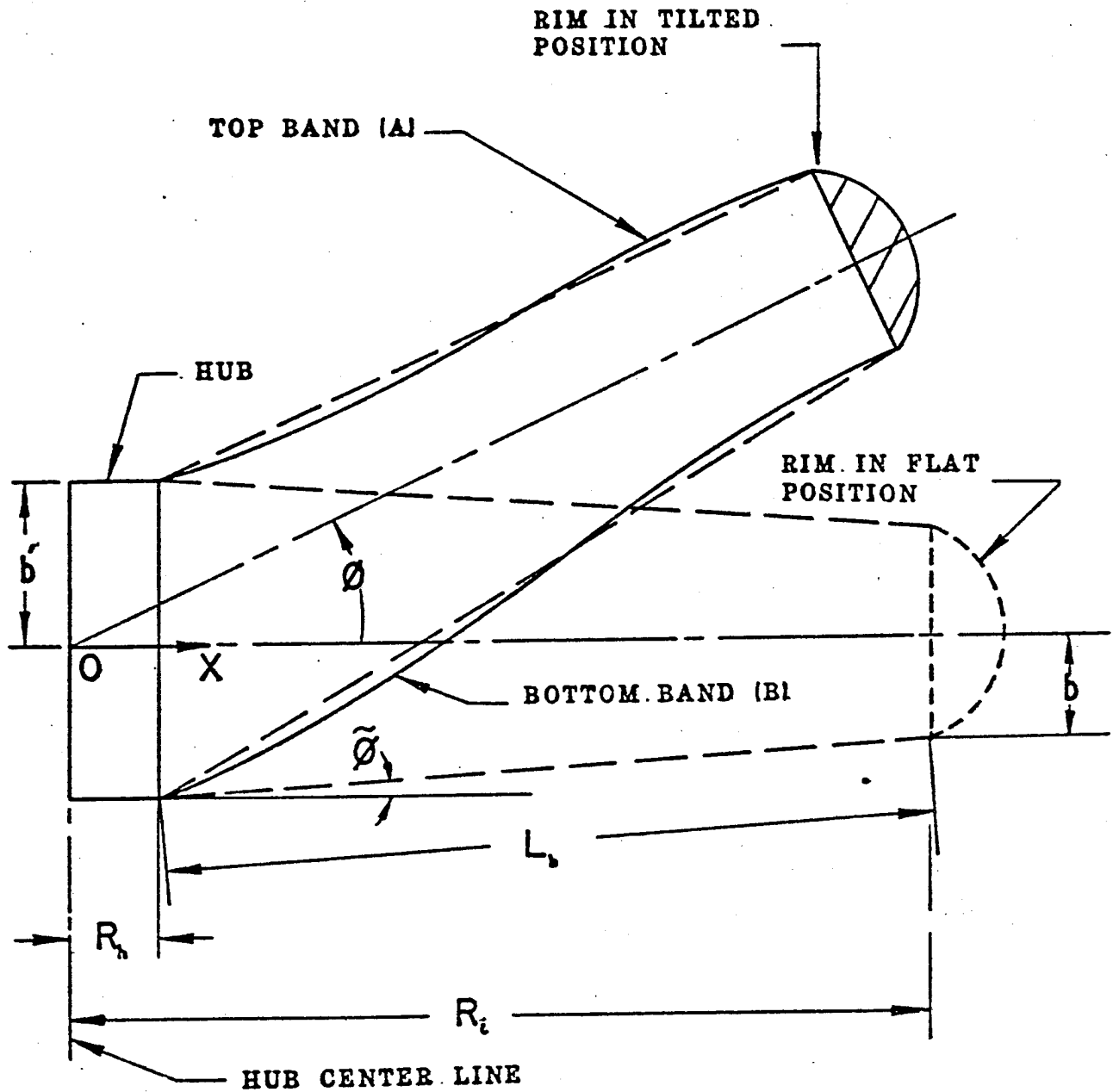


Fig. D1. Schematic diagram depicting behavior of a set of two bands behaving as a double beam with compressive column action in the top beam and tensile tie-bar action in the bottom beam. Rotation takes place about point O.

where $P_1 \equiv$ initial winding tension; $P_c \equiv$ centrifugal tension given in Appendix B.

The governing differential equations are

$$E_b \frac{d^4 w^A}{dx^4} - P_A \frac{d^2 w^A}{dx^2} = 0 \quad (\text{Band A}) \quad (D-3)$$

$$E_b \frac{d^4 w^B}{dx^4} - P_B \frac{d^2 w^B}{dx^2} = 0 \quad (\text{Band B})$$

The boundary conditions are listed in Table D1.

Table D1

Boundary Conditions for Out-of-Plane Bending of Bands

<u>Band</u>	<u>Left End</u>	<u>Right End</u>
A	$w^A(0) = 0$	$w^A(L_b) = w_{AL} \cos \bar{\phi} + u_{AL} \sin \bar{\phi} \approx (R_1 \cos \bar{\phi} - b \sin \bar{\phi}) \phi$
A	$\frac{dw^A(0)}{dx} = 0$	$\frac{dw^A(L_b)}{dx} = \phi$
B	$w^B(0) = 0$	$w^B(L_b) = w_{BL} \cos \bar{\phi} - u_{BL} \sin \bar{\phi} \approx (R_1 \cos \bar{\phi} - b \sin \bar{\phi}) \phi$
B	$\frac{dw^B(0)}{dx} = 0$	$\frac{dw^B(L_b)}{dx} = \phi$

In order to write the appropriate solutions for equations (D-3), it is necessary to know whether P_A and P_B are positive (tensile) or negative (compressive). Due to the initial tension, it turns out that

for the higher rotational speeds of major importance, for small angles, even P_A is tensile while P_B is tensile under any conditions. Thus, the general solutions may be written as

$$w^A(x) = A_1 \cosh k_A x + A_2 \sinh k_A x + A_3 + A_4 x \quad (D-4)$$

$$w^B(x) = B_1 \cosh k_B x + B_2 \sinh k_B x + B_3 + B_4 x$$

where

$$k_A \equiv (P_A/E_b I_2)^{1/2}, \quad k_B \equiv (P_B/E_b I_2)^{1/2}, \quad (D-5)$$

$I_2 \equiv$ Area moment of inertia of the band cross-sectional area about an in-plane axis

Using the boundary conditions to evaluate A_1, \dots, A_4 and B_1, \dots, B_4 , one can write the following results for the bending moments at the ends of the individual bands:

$$M_{AL} = -E_b I_2 \frac{d^2 w^A(L_b)}{dx^2}$$

or

$$M_{AL} = -E_b I_2 k_A^2 \frac{\left(\cosh k_A L_b - \frac{\sinh k_A L_b}{k_A L_b} \right) L_b + (1 - \cosh k_A L_b) R'}{2(1 - \cosh k_A L_b) + k_A L_b \sinh k_A L_b}$$

(D-6)

where $R' \equiv R \cos \phi - b \sin \phi$.

These same expressions hold for M_{BL} if k_A is replaced by k_B .

Since we are interested in the case where $\phi \rightarrow 0$ only, it is

accurate enough to use $P_A \approx P_i + P_c$ in equation (D-6).

In addition to moments M_{AL} and M_{BL} associated with bending of the individual bands about their own centroids, there is a moment carried in the form of membrane stresses in the individual bands. It is given by

$$M_m = b(P_B - P_A) \approx 2 A_b E_b b (b \cos \bar{\phi} + R_i \sin \bar{\phi}) \phi / L_b \quad (D-7)$$

The total moment carried by the double beam is*

$$M = M_m + M_{AL} + M_{BL} \quad (D-8)$$

The tilting stiffness of the double beam is

$$k'_b = M/\phi = 2 A_b E_b b (b \cos \bar{\phi} + R_i \sin \bar{\phi}) / L_b + 2 E_b I_2 k_A^2 \frac{\left(\cosh k_A L_b - \frac{\sinh k_A L_b}{k_A L_b} \right) L_b + (1 - \cosh k_A L_b) R'}{2(\cosh k_A L_b - 1) - k_A L_b \sinh k_A L_b} \quad (D-9)$$

Now it is necessary to consider how the various sets of bands contribute to the stiffness of the band system. For a band located at an angle θ from the normal to the axis about which tilting takes place, the effective angle of tilt is $\phi \cos \theta$. Furthermore, only the $\cos \theta$ component of the moment acts about the axis of tilt. Referring to Fig. C1, one finds that there are a total of two sets of bands at θ , two at $30^\circ - \theta$, two at $30^\circ + \theta$, two at $60^\circ - \theta$, two at $60^\circ + \theta$, and two at $90^\circ - \theta$. Thus, the total out-of-plane stiffness related to band-set

* The moment generated by the shear force where the band is attached to the rim is small and is neglected in equation (D-8).

stiffness k'_b is as follows:*

$$K_{bop} = [2 \cos^2 \theta + 2 \cos^2 (30^\circ - \theta) + 2 \cos^2 (30^\circ + \theta) + 2 \cos^2 (60^\circ - \theta) + 2 \cos^2 (60^\circ + \theta) + 2 \cos^2 (90^\circ - \theta)] k'_b = 6 k' \quad (D-10)$$

It is interesting to note that even up to $\Omega = 32,000$ rpm, K_{bop} is mainly dominated by the membrane action, i.e. M_m as defined in equation (D-7). This term is significantly influenced by the angle $\bar{\phi}$. In the Sandia flywheel System A, the average $\bar{\phi}$ is approximately equal to 2.66° . Using equation (D-9). One obtains 23.6% extra stiffness by incorporating the angle $\bar{\phi}$ as compared to the case when it is not incorporated.

For System B, the bands are twisted as shown in Fig. C2(b). If a moment of M_o , instead of a force Q , is applied at one end, the moment distribution would be

$$M(x) = M_o \quad (D-11)$$

The slope at the point of application of M_o can be deduced from the following equation.

$$(\phi/M_o)_{\text{twisted}} = \int_0^{L_b} [1/E_b (I_2 \cos^2 \bar{x} + I_1 \sin^2 \bar{x})] dx \quad (D-12)$$

where $\bar{x} \equiv \pi(L_b - x)/2L_b$

For the case where the bands are not pretwisted, the value of

* Another contribution to the stiffness is the integrated torsional stiffness in each band. However, its value is very small even for System B which has more torsional stiffness due to pretwisting, and is neglected here.

ϕ/M_o is

$$(\phi/M_o)_{\text{nontwisted}} = \int_0^{L_b} (1/E_b I_2) dx \quad (D-13)$$

Combining equations (D-12) and (D-13), one obtains the following result pertinent to the System B design

$$(\phi/M_o)_{\text{twisted}} / (\phi/M_o)_{\text{nontwisted}} \approx 5.0 \quad (D-14)$$

Thus, the second term in equation (D-9) should be multiplied by 5 in order to incorporate the pretwisted angle of $\pi/2$.

In System B, $\bar{\phi}$ is approximately equal to 2.13° . Thus, one obtains approximately 19% more stiffness by incorporating the angle $\bar{\phi}$ as compared to the case when it is not incorporated.

APPENDIX E

DERIVATION OF THE COMPLIANCE COEFFICIENTS

E.1 Turbine Shaft

The turbine shaft is modeled as a stepped diameter beam simply supported at two stations by ball bearings and loaded by a concentrated overhung force F_o and a moment M_o at the air turbine; see Fig. E1.

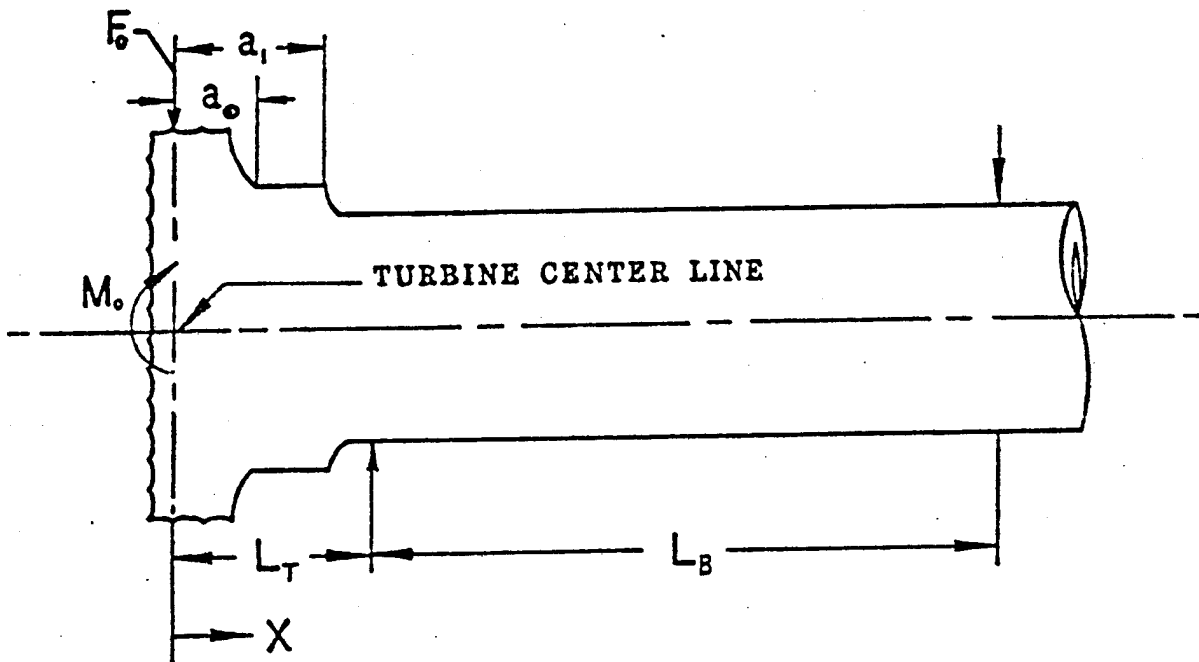


Fig. E1. Schematic loading diagram for the turbine shaft.

The method used here to calculate the turbine shaft deflection is the principle of virtual work (Casigliano's least-work theorem) as used for stepped diameter shafts by Bert [36]. Since the present shaft is relatively short, the additional deflection due to transverse shear is also included here.

From statics, the bending moment and transverse shear force distributions are found to be

$$M(z) = \begin{cases} M_o - F_o z & 0 \leq z \leq L_T \\ \left(\frac{M_o}{L_B} - \frac{F_o L_T}{L_B}\right)(L - z) & L_T \leq z \leq L_{TB} \end{cases} \quad (E-1)$$

$$V(z) = \begin{cases} -F_o & 0 \leq z \leq L_T \\ \frac{F_o L_T}{L_B} - \frac{M_o}{L_B} & L_T \leq z \leq L_{TB} \end{cases}$$

where $L_{TB} \equiv L_T + L_B$, $L_A \equiv$ Length of shaft having area A_T , $L_T \equiv$ overhung distance (between point of load F_o and the closest bearing), $L_B \equiv$ distance between bearings, and $z \equiv$ position measured from point of application of F_o .

The principle of virtual work can be applied to obtain the following expressions for transverse deflection and slope at the point where F_o and M_o are applied:

$$r_o = \frac{\partial U}{\partial F_o} \quad ; \quad \phi_o = \frac{\partial U}{\partial M_o} \quad (E-3)$$

where U is the sum of the flexural and transverse shear strain energies given by

$$U = \int_{a_o}^{L_{TB}} \frac{[M(z)]^2}{2 E_s I(z)} dz + \int_{a_o}^{L_{TB}} \frac{[V(z)]^2}{2 G_s K(z) A(z)} dz \quad (E-4)$$

$A(z)$ is the distribution of cross-sectional area, E_s is Young's modulus, G_s is the shear modulus, $I(z)$ is the distribution of area moment of inertia, $K(z)$ is the distribution of the transverse shear correction factor, a_o is the distance between turbine center to the closest turbine shaft.

Combining the preceding two equations, one obtains

$$r_o = \int_{a_o}^{L_{TB}} \frac{M \frac{\partial M}{\partial F_o}}{E_s I} dz + \int_{a_o}^{L_{TB}} \frac{V \frac{\partial V}{\partial F_o}}{K A G_s} dz \quad (E-5)$$

$$\phi_o = \int_{a_o}^{L_{TB}} \frac{M \frac{\partial M}{\partial M_o}}{E_s I} dz + \int_{a_o}^{L_{TB}} \frac{V \frac{\partial V}{\partial M_o}}{K A G_s} dz \quad (E-6)$$

Inserting the distributions $A(z)$, $I(z)$, $M(z)$, and $V(z)$ appropriate to the present general geometry, as shown in Fig. E1, into equations (E-5), (E-6) and performing integration, one obtains

$$r_o = \alpha_1 F_o + \alpha_2 M_o \quad (E-7)$$

$$\alpha_o = \alpha_2 F_o \quad \alpha_3 M_o \quad (E-8)$$

where α_i 's are the compliances and are defined as

$$\begin{aligned} \alpha_1 &\equiv \frac{a_1^3 - a_o^3}{3 E_s I_{TS}} + \frac{L_T^3 - a_1^3 - L_T^2 L_B}{3 E_s I_{BS}} + \frac{a_1 - a_o}{K_T A_T G_s} + \frac{L_T - a_1 + L_T^2 L_B^{-1}}{K_B A_B G_s} \\ \alpha_2 &\equiv - \left(\frac{a_1^2 - a_o^2}{2 E_s I_{TS}} + \frac{L_T^2 - a_1^2}{2 E_s I_{BS}} + \frac{L_T L_B}{3 E_s I_{BS}} + \frac{L_T L_B^{-1}}{K_B A_B G_s} \right) \\ \alpha_3 &\equiv \frac{a_1 - a_o}{E_s I_{TS}} + \frac{L_T - a_1}{E_s I_{BS}} + \frac{L_B}{3 E_s I_{BS}} + \frac{L_B^{-1}}{K_B A_B G_s} \end{aligned} \quad (E-9)$$

To calculate the transverse shear correction coefficient, which allows for the nonuniform distribution of transverse shear strain through the depth of the shaft, the following expression presented by Cowper [37] is used

$$K = \frac{6(1 + \nu)}{7 + 6\nu + 4(4 + 3\nu)B^2/(1 + B^2)^2} \quad (E-10)$$

where $B \equiv$ inside diameter/outside diameter and ν is Poisson's ratio.

E.2 Flywheel Shaft

The flywheel shaft is essentially supported as a cantilever at its top end by rigid attachment to the turbine shaft. The flywheel shaft is quite flexible in comparison to the turbine shaft and the former is concentrically located inside the latter.

The upper portion of the flywheel shaft has a length of $L_u (= 10 \text{ in.})$ with an area moment of inertia $I_u (= 0.00485 \text{ in}^4)$. The lower portion of the flywheel shaft contains a short, necked-down "breakaway" region of length $L_l (= 1.0 \text{ in.})$ with area moment of inertia $I_l (= 0.002425 \text{ in}^4)$.

Using the method of principle of virtual work as presented in [36], one obtains the following deflection and slope for the hub relative to the turbine.

$$\begin{aligned} r_{h/t} &= \alpha_4 F_h + \alpha_5 M_h \\ \phi_{h/t} &= \alpha_5 F_h + \alpha_6 M_h \end{aligned} \quad (E-11)$$

where F_h and M_h are the force and moment applied on the flywheel shaft at the position where hub located; α_i 's are defined as

$$\begin{aligned} \alpha_4 &\equiv \frac{1}{3 E_s} [(L_u^3/I_u) + (L_s^3 - L_u^3)/I_2] \\ \alpha_5 &\equiv \frac{1}{2 E_s} [(L_u^2/I_u) + (L_s^2 - L_u^2)/I_2] \\ \alpha_6 &\equiv \frac{1}{E_s} [L_u/I_u + (L_s - L_u)/I_2] \end{aligned} \quad (E-12)$$

here $L_s \equiv L_u + L_2 (= 11 \text{ in.})$.

When a force F_h is applied, a force-couple system $F_h, F_h L_s$ is developed on the turbine shaft, which in turn, causes the turbine shaft to have the following deflection and slope at the point where the flywheel shaft is attached to it

$$\begin{aligned} r_t &= \alpha_1 F_h + \alpha_2 L_s F_h \\ \phi_t &= \alpha_2 F_h + \alpha_3 L_s F_h \end{aligned} \quad (E-13)$$

The net deflection and slope for the shaft at the axial position where the hub is located (under the point of application of load F_h) can

be obtained by using equations (E-11) - (E-13)

$$\begin{aligned} r_h &= \alpha_4 F_h + \alpha_1 F_h + \alpha_2 L_s F_h + (\alpha_2 F_h + \alpha_3 L_s F_h) L_s \\ \phi_h &= \alpha_5 F_h + \alpha_2 F_h + \alpha_3 L_s F_h \end{aligned} \quad (E-14)$$

The preceding two equations can be rewritten as

$$\begin{aligned} r_h &= \alpha_{33} F_h \\ \phi_h &= \alpha_{12} F_h \end{aligned} \quad (E-15)$$

where α_{12} and α_{33} are defined as follows

$$\begin{aligned} \alpha_{12} &\equiv \alpha_5 + \alpha_2 + \alpha_3 L_s \\ \alpha_{33} &\equiv \alpha_4 + \alpha_1 + 2 \alpha_2 L_s + \alpha_3 L_s^2 \end{aligned} \quad (E-16)$$

Other compliances can be obtained in a very similar way and are listed below

$$\begin{aligned} \alpha_{44} &\equiv \alpha_6 + \alpha_3 \\ \alpha_{15} &\equiv \alpha_1 + \alpha_2 L_s \\ \alpha_{25} &\equiv \alpha_2 \\ \alpha_{55} &\equiv \alpha_1 \\ \alpha_{66} &\equiv \alpha_3 \\ \alpha_{16} &\equiv \alpha_2 + \alpha_3 L_s \end{aligned} \quad (E-17)$$

The deflection and slope of the flywheel shaft relative to the turbine, at the position where the external damper is located, are given below

when a force F_d is applied there.

$$r_{d/t} = \frac{L_d^3}{3 E_s I_u} F_d \quad (E-18)$$

$$\phi_{d/t} = \frac{L_d^2}{2 E_s I_u} F_d ; \quad L_d \equiv L_s - L_H$$

The deflection and slope of the turbine shaft are

$$r_t = \alpha_1 F_d + \alpha_2 L_d F_d \quad (E-19)$$

$$\phi_t = \alpha_2 F_d + \alpha_3 L_d F_d$$

Combining equations (E-18) and (E-19), one obtains

$$\alpha_{57} \equiv \alpha_1 + \alpha_2 L_d$$

$$\alpha_{67} \equiv \alpha_2 + \alpha_3 L_d$$

$$\alpha_{77} \equiv \frac{L_d^3}{3 E_s I_u} + \alpha_1 + \alpha_2 L_d + (\alpha_2 + \alpha_3 L_d) L_d \quad (E-20)$$

$$\alpha_{17} = \alpha_{37} = \alpha_{77} + \alpha_{27} (L_s - L_d)$$

$$\alpha_{27} = \alpha_{47} = \frac{L_d^2}{2 E_s I_u} + \alpha_2 + \alpha_3 L_d$$

The deflection and slope of the shaft relative to the turbine at the position where the external damper is located is given below (when a moment M_d is applied there).

$$r_{d/t} = \frac{L_d^2}{2 E_s I_u} M_d \quad (E-21)$$

$$\phi_{d/t} = \frac{L_d}{E_s I_u} M_d$$

The moment M_d is transmitted to the turbine and causes the turbine shaft to deflect and rotate the following respective amounts.

$$r_{d/t} = \alpha_2 M_d \quad (E-22)$$

$$\phi_{d/t} = \alpha_3 M_d$$

Thus, the net deflections and slopes for each component can be determined by the preceding two equation sets. The corresponding compliances are given below.

$$\begin{aligned} \alpha_{18} &= \alpha_2 + L_d^2/2 E_s I_u + (\alpha_3 + L_d/E_s I_u) L_H \\ \alpha_{28} &= \alpha_3 + L_d/E_s I_u \\ \alpha_{58} &= \alpha_2 \\ \alpha_{68} &= \alpha_3 \\ \alpha_{78} &= \alpha_2 + L_d^2/2 E_s I_u \\ \alpha_{88} &= \alpha_3 + L_d/E_s I_u \end{aligned} \quad (E-23)$$

APPENDIX F

CALCULATION OF THE VISCOUS DAMPING COEFFICIENT FOR THE DAMPER IN THE SANDIA SPIN-TEST FACILITY

In the Sandia spin-test facility, there is a Barbour Stockwell damper located on the flywheel shaft. The geometric dimensions for this damper are: damper radius = 1.5 in., damper axial length = 2 in. Thus, the total force acting on the damper along the line of centers is

$$F = (1.5)(2.0) \int_0^{2\pi} P(\theta) \cos \theta \, d\theta \quad (F-1)$$

where θ is the circumferential position, and $P(\theta)$ is the total dynamic pressure acting on the damper. A conservative estimate of $P(\theta)$ is the hydrodynamic pressure, i.e., the rate of change of inlet pressure is neglected. Following Bansal and Hibner's work [38], one can write the following expression for the viscous damping coefficient C_d .

$$C_d = \frac{\partial F}{\partial \dot{r}_r} = [6(1.5)^3 \mu / 2c^2] \int_0^{2\pi} \frac{4 \cos^2 \theta - \epsilon \cos 2\theta \cos \theta}{(1 - \epsilon \cos \theta)^2 (2 + \epsilon^2)} \, d\theta \quad (F-2)$$

where μ = oil viscosity $\approx 2.7 \times 10^{-6}$ lb-in/sec²

c = radial clearance of damper ≈ 0.040 in.

ϵ = eccentricity ratio ($|\bar{r}_d|/c$)

Using the data listed above as input and integrating equation (F-2) numerically, one can compute C_d as a function of ϵ . The results are listed below:

$\epsilon (= \bar{r}_d /c)$	0.1	0.2	0.3	0.4	0.5	0.6	0.7	0.8	0.9
C_d (lb-sec/in)	0.109	0.114	0.123	0.139	0.165	0.21	0.295	0.497	1.3

APPENDIX G

COMPUTER PROGRAM DOCUMENTATION AND LISTING

The numerical computations for the present investigation were carried out by means of a specially written digital computer program. The program was written in FORTRAN IV language and was run on the IBM System 370/158J at the University's Merrick Computing Center.

The program consisted of two parts. The first part was used to investigate the free whirling and stability. The second part was used to study the forced whirling. Several subroutines were used in addition to the main program. Major variables were defined by using comment statements in the computer program itself. The following is a list of the subroutines and their functions.

COMPLI	computing the compliance coefficients
EIGCC*	computing the complex eigenvalues of a general complex matrix
KBAND	computing the total band stiffnesses
LEQT2C*	solving the simultaneous linear complex equations or inverting a general complex matrix
MULTYC	performing multiplication of two complex matrices

* This is a standard subroutine found in IMSL Library 1, 6th ed., International Mathematical and Statistical Libraries, Inc., 1977, and thus, it is not listed herein.


```

C
C      F R E E   V I B R A T I O N   &   S T A B I L I T Y
C
      IMPLICIT REAL*8(A-H,C-Z)
      REAL*8 MR,IR,JR,MH,IH,JH,MT,IT,JD,MD,CD,WK(32),ID,JD,AMP(8)
      COMPLEX*16 MI(8,8),N(8,8),ALPH(8,8),K(8,8),WA(88),B1(8,8)
      COMPLEX*16 E2(8,8),C(16,16),W(16),Z(16,16),F(8),A(8,8)
      COMPLEX*16 AKBIP,AKBOP,A1,A2,DCMPLX,CPM
      DATA NDEG,NDEGD/8,16/

C
C      INPUT DAMPER MASS AND MASS MOMENTS OF INERTIA
C      INPUT RIM MASS AND MASS MOMENTS OF INERTIA
C      INPUT HUB MASS AND MASS MOMENTS OF INERTIA
C      INPUT TURBINE MASS AND MASS MOMENTS OF INERTIA
C
      DATA MD,ID,JD/0.008400,0.005900,0.009500/
      DATA MR,IR,JR/0.043000,1.036000,3.215000/
      DATA MH,IH,JH/0.0235000,0.247000,0.054000/
      DATA MT,IT,JT/0.02000,0.04000,0.067000/

C
C      IDAMP=0   INTERNAL DAMPING NOT INCLUDED
C      IDAMP=1   INTERNAL DAMPING INCLUDED
C
      IDAMP=0

C
C      CD=VISCOS DAMPING COEFFICIENT
C
      CD=0.
      DO 100 IM=1,NDEG
      DO 100 IN=1,NDEG
      N(IM,IN)=(0.00,0.00)
100  MI(IM,IN)=(0.00,0.00)

C
C      INVERT THE M MATRIX
C
      MI(1,1)=1./MR
      MI(2,2)=1./IR
      MI(3,3)=1./MH
      MI(4,4)=1./IH
      MI(5,5)=1./MT
      MI(6,6)=1./IT
      MI(7,7)=1./MD
      MI(8,8)=1./ID
      N(7,7)=DCMPLX(0.0000,CD)
      CALL COMPLI(ALPH,IDAMP)
      A1=ALPH(1,1)
      A2=ALPH(2,2)
      DO 900 I=1,4
      DO 900 J=1,9
      RPM=J*10.**I

```



```
RAD=RPM*3.141592654/30.
N(2,2)=JR*RAD
N(4,4)=JH*RAD
N(6,6)=JT*RAD
N(8,8)=JD*RAD
```

C
C
C

CALL KBAND TO COMPUTE INTEGRATED BAND STIFFNESSES

```
CALL KBAND(AK8IP,AKBCP,RAD,IDAMP)
ALPH(1,1)=A1+1./AK8IP
ALPH(2,2)=A2+1./AKBCP
DO 102 IK=1,NDEG
DO 102 JK=1,NDEG
IF(IK.EQ.JK) GO TO 101
K(IK,JK)=(0.00,0.00)
GO TO 102
101 K(IK,JK)=(1.00,0.00)
102 CONTINUE
DO 103 IA=1,NDEG
DO 103 JA=1,NDEG
103 A(IA,JA)=ALPH(IA,JA)
```

C
C
C
C

CALL LEGT2C TO INVERT COMPLIANCE MATRIX
LEGT2C IS A ROUTINE IN IMSL PACKET

```
CALL LEGT2C(A,NDEG,NDEG,K,NDEG,NDEG,0.0,WA,IER)
CALL MULTYC(MI,N,81,NDEG)
CALL MULTYC(MI,K,22,NDEG)
DO 10 KD=1,NDEG
DO 10 LD=1,NDEG
10 D(KD,LD)=(0.00,0.00)
DO 20 KD=1,NDEG
KCD=KD+NDEG
20 D(KC,KDD)=(1.00,0.00)
DO 30 KD=1,NDEG
KCD=KD+NDEG
DO 30 LD=1,NDEG
30 D(KCD,LD)= 82(KD,LD)
DO 40 KD=1,NDEG
KCD=KD+NDEG
DO 40 LD=1,NDEG
LDD=LD+NDEG
40 D(KCD,LDD)= 81(KD,LD)
PRINT 1000,RPM
PRINT 4000
PRINT 5000
```

C
C
C
C

CALL EIGCC TO SOLVE EIGEN VALUE PROBLEM
EIGCC IS A ROUTINE LISTED IN IMSL PACKET


```

CALL EIGCC(D,NDEGC,NDEGD,0.,W,Z,NDEGD,WK,IER)
DO 60 IP=1,NDEGD
CPM=W(IP)*30./3.141592654
60 PRINT 2000,CPM
900 CONTINUE
1000 FORMAT(5X,'ROT SPEED(RPM)=' ,D15.5,/)
2000 FORMAT(10X,2D15.5)
4000 FORMAT('          RE(WHIR FRE)      IM(WHIR FRE)')
5000 FORMAT('          (CPM)              (CPM)')
STOP
END
SUBROUTINE COMPLI(ALPH,IDAMP)
IMPLICIT COMPLEX*16(A-D)
COMPLEX*16 ALPH(6,8)
REAL*8 ES,IS,ITS,IES,LT,LB,LE,LH,LD,LS,GAMAES,EIS
REAL*8 GS,A0,A1,GAMAGS,GIS,KT,AT,AB,KB,LU,IU,IL
C
C      INPUT SHAFT AREA MOMENTS OF INERTIA
C
DATA IS,ITS,IBS/0.00485000,0.2375000,0.08665000/
C
C      INPUT SHAFT LENGTHS DEFINED IN FIG. 1.1
C
DATA LT,LB,LE,LH/1.63000,3.37000,1.94000,4.06000/
C
C      INPUT MATERIAL PROPERTIES
C
DATA ES,GS/29.500,11.500/
DATA GAMAES,GAMAGS/0.00500,0.00500/
C
C      INPUT LENGTHS OF A0,A1 DEFINED IN FIG. E1
C
DATA A0,A1/0.5700,1.37500/
C
C      INPUT AREAS OF SHAFT
C      INPUT SHEAR CORRECTION FACTOR
C
DATA KT,AT,KB,AB/0.638800,1.39600,0.587500,0.736300/
DATA LU,IU,IL/10.00,0.0048500,0.00242500/
LE=LT+LB+LE
LS=LD+LH
C.....IDAMP=0.....INTERNAL DAMPING IS NOT INCLUDED
C.....IDAMP=1.....INTERNAL DAMPING IS INCLUDED
IF(IDAMP.EQ.0) GO TO 10
EIS=-GAMAES*ES
AES=DCMPLX(ES,EIS)
GIS=-GAMAGS*GS
AGS=DCMPLX(GS,GIS)
GO TO 20
10 AES=ES

```



```

AGS=GS
20 ALPH1=(A1**3-A0**3)/3./AES/ITS+(LT**3-A1**3+LT**2*LB)/3.
1 /AES/IBS+(A1-A0)/KT/AT/AGS+(LT-A1+LT**2/LB)/KB/AB/AGS
ALPH2=-(A1**2-A0**2)/2./AES/ITS-(LT**2-A1**2)/2./AES/IBS
1-LT*LB/3./AES/IBS-LT/LB/KB/AB/AGS
ALPH3=(A1-A0)/AES/ITS+(LT-A1)/AES/IES+LB/3./AES/IBS+1./LB/KB/AB
1/AGS
ALPH4=((LU**3/IU)+(LS**3-LU**3)/IL)/3./AES
ALPH5=((LU**2/IU)+(LS**2-LU**2)/IL)/2./AES
ALPH6=(LU/IU+(LS-LU)/IL)/AES
ALPH(1,1)=ALPH4+ALPH1+2.*ALPH2*LS+ALPH3*LS**2
ALPH(1,2)=ALPH5+ALPH2+ALPH3*LS
ALPH(1,3)=ALPH(1,1)
ALPH(1,4)=ALPH(1,2)
ALPH(1,5)=ALPH1+ALPH2*LS
ALPH(1,6)=ALPH2+ALPH3*LS
ALPH(1,7)=LD**3/3./AES/IU+ALPH1+ALPH2*LD+(ALPH2+ALPH3*LD)
1*LD+LH*(LD**2/2./AES/IU+ALPH2+ALPH3*LD)
ALPH(2,2)=ALPH6+ALPH3
ALPH(2,3)=ALPH(1,2)
ALPH(2,4)=ALPH(2,2)
ALPH(2,5)=ALPH2
ALPH(2,6)=ALPH3
ALPH(2,7)=(LD**2/2./AES/IU+ALPH2+ALPH3*LD)
ALPH(3,3)=ALPH(1,1)
ALPH(3,4)=ALPH(1,2)
ALPH(3,5)=ALPH(1,5)
ALPH(3,6)=ALPH(1,6)
ALPH(3,7)=ALPH(1,7)
ALPH(4,4)=ALPH(2,2)
ALPH(4,5)=ALPH(2,5)
ALPH(4,6)=ALPH(2,6)
ALPH(4,7)=ALPH(2,7)
ALPH(5,5)=ALPH1
ALPH(5,6)=ALPH(2,5)
ALPH(5,7)=ALPH1+ALPH2*LD
ALPH(6,6)=ALPH(2,6)
ALPH(6,7)=ALPH2+ALPH3*LD
ALPH(7,7)=LD**3/3./AES/IU+ALPH1+ALPH2*LD+(ALPH2+ALPH3*LD)*LD
ALPH(1,8)=ALPH2+LD**2/2./AES/IU+(ALPH3+LD/AES/IU)*LH
ALPH(2,8)=ALPH3+LD/AES/IU
ALPH(3,8)=ALPH(1,8)
ALPH(4,8)=ALPH(2,8)
ALPH(5,8)=ALPH2
ALPH(6,8)=ALPH3
ALPH(7,8)=ALPH2+LD**2/2./AES/IU
ALPH(8,8)=ALPH3+LD/AES/IU
DO 30 I=2,8
K=I-1
DO 30 J=1,K

```



```

30 ALPH(I,J)=ALPH(J,I)
   RETURN
   END
   SUBROUTINE KBAND(AKBIP,AKJCP,RAD,IDAMP)
C.....IDAMP=0.....INTERNAL DAMPING IS NOT INCLUDED
C.....IDAMP=1.....INTERNAL DAMPING IS INCLUDED
   IMPLICIT REAL*8(A-H,C-Z)
   COMPLEX*16 CDSQRT,CDEXP,DCMPLX
   COMPLEX*16 AEBAND,DI,UO,UO0,FBCPRI,P,AK,AKL,AKB,AKA,AKAL,G,AM
   COMPLEX*16 HYSIN,HYCOS,AKBIP,AKJCP
   REAL*8 LBAND
   DATA RORIM,ARIM,RRIM,ERIM/1.399D-4,5.596D0,8.633D0,18.D6/

C
C      2.66 IS THE BAND ANGLE
C
   PHWAVE=2.66*3.141592654/180.

C
C      TENSIO IS THE BAND INITIAL WINDING TENSION
   TENSIC=360.D0

C
C.....ND=# OF BAND SETS
   ND=12
   T0=360./ND/2.*3.141592654/180.
   DATA RH,RI/2.25D0,7.625D0/
   LBAND=(RI-RH)/DCOS(PHWAVE)

C
C      BB,TB ARE BAND WIDTH AND THICKNESS RESPECTIVELY
C      ROBAND, EBAND ARE BAND MATERIAL DENSITY AND YOUNG'S MODULUS
C      GABAND= BAND LOSS TANGENT
C
   DATA BB,TB,ROBAND,EBAND/0.5D0,0.1D0,1.295D-4,11.D6/
   DATA GABAND/3.3172D0/
   ABAND=BB*TB
   AIIP=TB*BB**3/12.
   AICP=TB**3*EB/12.
   IF(IDAMP.EQ.0) GO TO 1
   EIBAND=-GABAND*EBAND
   AEBAND=DCMPLX(EBAND,EIBAND)
   GO TO 2
1 AEBAND=EBAND
2 UO0=ROBAND*RAD**2/AEBAND*(RI**3/3-RI**2*RH/2.+RH**3/6.)
   UP=RAD**2*(RORIM*ARIM*RRIM**2*DTAN(T0)+ROBAND*ABAND*DCOS(PHWAVE)
   I**3*(RI**3/3.-RI**2*RH/2.+RH**3/6.)/2./LBAND)
   DR=ARIM*ERIM/RRIM*DTAN(T0)
   DI=ABAND*EBAND/2./LBAND*UCOS(PHWAVE)**2
   UO=UP/(DR+DI)
   FBCPRI=ABAND*AEBAND/LBAND*(UO-UO0*DCOS(PHWAVE))*DCOS(PHWAVE)
   FBC=ROBAND*ABAND*RAD**2*(2.*RI**J-3.*RI**2*RH+RH**3)/6./((RI-RH)
   P=TENSIC+FBC+FBCPRI
   AK=CDSQRT(P/AEBAND/AIIP)

```



```
AKL=AK*LBAND
HYSIN=(CDEXP(AKL)-CDEXP(-AKL))/2.
HYCOS=(CDEXP(AKL)+CDEXP(-AKL))/2.
AKB=AK*P*HYSIN/(2.*(1.-HYCOS)+AKL*HYSIN)
AKBIP=12.*(ABAND*AEBAND/LBAND*DCOS(PH*AVE)**2+AKB)
AKA=CDSQRT(P/AEBAND/AICP)
AKAL=AKA*LBAND
HYSIN=(CDEXP(AKAL)-CDEXP(-AKAL))/2.
HYCOS=(CDEXP(AKAL)+CDEXP(-AKAL))/2.
RP=RI*DCOS(PH*AVE)-1.5*DSIN(PH*AVE)
G=(HYCOS-HYSIN/AKAL)*LBAND+(1.-HYCOS)*RP
AM=AEBAND*AICP*AKA**2*G/(2.*(HYCOS-1.)-AKAL*HYSIN)
AKB=2.*ABAND*AEBAND*1.5*(1.5*DCOS(PH*AVE)+RI*DSIN(PH*AVE))/LBAND
1+2.*AM
AKECP=6.*AKE
RETURN
END
SUBROUTINE MULTYC(A,B,C,N)
COMPLEX*16 A(N,N),B(N,N),C(N,N)
DO 5 I=1,N
DO 5 J=1,N
C(I,J)=(0.D0,0.D0)
DO 5 K=1,N
5 C(I,J)=C(I,J)+A(I,K)*B(K,J)
RETURN
END
```



```

C
C      F O R C E D      V I B R A T I O N
C
      IMPLICIT REAL*8(A-H,C-Z)
      REAL*8 MR,IR,JR,MH,IF,JH,MT,IT,JT,MD,CD,WK(32),ID,JD,AMP(8)
      COMPLEX*16 ALPH(8,8),K(8,8),F(8),WA(88),A(8,8)
      COMPLEX*16 DCMPLX,AKBIP,AKBCP,A1,A2,CPM

C
C      IDAMP=0      INTERNAL DAMPING NOT INCLUDED
C      IDAMP=1      INTERNAL DAMPING INCLUDED
C
      IDAMP=1
      DATA NDEG,NDEGO/8,16/

C
C      INPUT DAMPER MASS AND MASS MOMENTS OF INERTIA
C      INPUT RIM MASS AND MASS MOMENTS OF INERTIA
C      INPUT HUB MASS AND MASS MOMENTS OF INERTIA
C      INPUT TURBINE MASS AND MASS MOMENTS OF INERTIA
C
      DATA MD,ID,JD/0.008400,0.005900,0.009500/
      DATA MR,IR,JR/0.043000,1.636000,3.215000/
      DATA MH,IF,JH/0.023500,0.247000,0.054000/
      DATA MT,IT,JT/0.02000,0.04000,0.067000/

C
C      I C A S E = 1      INITIAL UNBALANCE
C      I C A S E = 2      INITIAL TILT
C      I C A S E = 3      COMBINATION
C
      ICASE=1
      DO 900 ICD=1,10

C
C      CD=VISCOUS DAMPING COEFFICIENT
C
      CD=ICD*0.1
      PRINT 7000, CD
      IF(ICASE-2) 5,6,7
5 PRINT 4000
GO TO 8
6 PRINT 5000
GO TO 8
7 PRINT 6000
8 CONTINUE

C
C      CALL COMPLI TO COMPUTE COMPLIANCE COEFFICIENTS
C
      CALL COMPLI(ALPH,IDAMP)
      A1=ALPH(1,1)
      A2=ALPH(2,2)
      DO 900 I=1,4
      DO 900 J=1,9

```



```

RPM=J*10.**1
RAD=RPM*3.141592654/30.
RAD=RPM*3.141592654/30.

C
C      CALL KBAND TO COMPUTE INTEGRATED BAND STIFFNESSES
C
      CALL KBAND(AK8IP,AKECP,RAD,ICAMP)
      ALPH(1,1)=A1+1./AK8IP
      ALPH(2,2)=A2+1./AK8CP
      DO 102 IK=1,NDEG
      DO 102 JK=1,NDEG
      IF(IK.EQ.JK) GO TO 101
      K(IK,JK)=(0.D0,0.D0)
      GO TO 102
101 K(IK,JK)=(1.D0,0.D0)
102 CONTINUE
      DO 103 IA=1,NDEG
      DO 103 JA=1,NDEG
103 A(IA,JA)=ALPH(IA,JA)

C
C      CALL LEQT2C TO INVERT COMPLIANCE MATRIX
C      LEQT2C IS A ROUTINE IN IMSL PACKET
C
      CALL LEQT2C(A,NDEG,NDEG,K,NDEG,NDEG,0,WA,IER)
      DO 104 IF=1,NDEG
104 F(IF)=(0.D0,0.D0)
      IF(ICASE-2) 105,106,107
105 F(1)=MR*RAD**2
      GO TO 108
106 F(2)=(IR-JR)*RAD**2
      GO TO 108
107 F(1)= MR*RAD**2 *0.028
      F(2)= (IR-JR)*RAD**2*0.0023
108 K(1,1)=K(1,1)-MR*RAD**2
      K(2,2)=K(2,2)-(IR+JR)*RAD**2
      K(3,3)=K(3,3)-MH*RAD**2
      K(4,4)=K(4,4)-(IH+JH)*RAD**2
      K(5,5)=K(5,5)-MT*RAD**2
      K(6,6)=K(6,6)-(IT+JT)*RAD**2
      K(7,7)=K(7,7)-MD*RAD**2-DCMPLX(0.0D00,CD)*RAD
      K(8,8)=K(8,8)-(IC+JD)*RAD**2

C
C      CALL LEQT2C TO SOLVE LINEAR SIMULTANECUS EGS
C
      CALL LEQT2C(K,NDEG,NDEG,F,1,NDEG,0,WA,IER)
      DO 201 IP=1,NDEG
201 AMP(IP)=CDABS(F(IP))
      PRINT 3000,RPM,(AMP(L),L=1,NDEG)
900 CONTINUE
3000 FORMAT(10X,G012.4)

```



```

4000 FORMAT('          RCT SPEED  ABS RR/ER  ABS PR/ER  ABS RH/ER
1  ABS PH/ER  ABS RT/ER  ABS PT/ER  ABS RD/ER  ABS PD/ER',/)
5000 FORMAT('          RCT SPEED  ABSRR/PCR  ABSPR/PCR  ABSRH/PCR
1  ABSPH/POR  ABSRT/PCR  ABSPT/POR  ABSRD/PCR  ABSPD/POR',/)
6000 FORMAT('          RCT SPEED  ABSRR  ABSPR  ABSRH
1  ABSPH  ABSRT  ABSPT  ABSRC  ABSPD',/)
7000 FORMAT(SX,'CD=',FS.2,/)
      STCP
      END
      SUBROUTINE COMPLI(ALPH,IDAMP)
      IMPLICIT COMPLEX*16(A-D)
      COMPLEX*16 ALPH(8,8)
      REAL*8 ES,IS,ITS,IBS,LT,LB,LE,LH,LD,LS,GAMAES,EIS
      REAL*8 GS,A0,A1,GAMAGS,GIS,KT,AT,AB,KB,LU,IU,IL

C      INPUT SHAFT AREA MOMENTS OF INERTIA
C
C      DATA IS,ITS,IBS/0.00465000,0.2375000,0.02665000/
C
C      INPUT SHAFT LENGTHS DEFINED IN FIG. 1.1
C
C      DATA LT,LB,LE,LH/1.63000,3.37000,1.94000,4.06000/
C
C      INPUT MATERIAL PROPERTIES
C
C      DATA ES,GAMAES/29.5000,0.005000/
C      DATA US,GAMAGS/11.5000,0.005000/
C
C      INPUT LENGTHS OF A0,A1 DEFINED IN FIG. E1
C
C      DATA A0,A1/0.5700,1.37500/
C
C      INPUT AREAS OF SHAFT
C      INPUT SHEAR CORRECTION FACTOR
C
C      DATA KT,AT,KB,AB/0.633800,1.39600,0.587500,0.736300/
C      DATA LU,IU,IL/10.00,0.0046500,0.00242500/
C      LD=LT+LB+LE
C      LS=LD+LH
C.....IDAMP=0.....INTERNAL DAMPING IS NOT INCLUDED
C.....IDAMP=1.....INTERNAL DAMPING IS INCLUDED
      IF(IDAMP.EQ.0) GO TO 10
      EIS=-GAMAES*ES
      AES=DCMPLX(ES,EIS)
      GIS=-GAMAGS*GS
      AGS=DCMPLX(GS,GIS)
      GO TO 20
10  AES=ES
    AGS=GS
20  ALPH1=(A1**3-A0**3)/3./AES/ITS+(LT**3-A1**3+LT**2*LB)/3.

```



```

1 /AES/IBS+(A1-A0)/KT/AT/AGS+(LT-A1+LT**2/LB)/KE/AB/AGS
  ALPH2=-(A1**2-A0**2)/2./AES/ITS-(LT**2-A1**2)/2./AES/IBS
1-LT*LB/3./AES/IBS-LT/LB/KB/AB/AGS
  ALPH3=(A1-A0)/AES/ITS+(LT-A1)/AES/IBS+LB/3./AES/IBS+1./LB/KB/AB
1/AGS
  ALPH4=((LU**3/IU)+(LS**3-LU**3)/IL)/3./AES
  ALPH5=((LU**2/IU)+(LS**2-LU**2)/IL)/2./AES
  ALPH6=(LU/IU+(LS-LU)/IL)/AES
  ALPH(1,1)=ALPH4+ALPH1+2.*ALPH2*LS+ALPH3*LS**2
  ALPH(1,2)=ALPH5+ALPH2+ALPH3*LS
  ALPH(1,3)=ALPH(1,1)
  ALPH(1,4)=ALPH(1,2)
  ALPH(1,5)=ALPH1+ALPH2*LS
  ALPH(1,6)=ALPH2+ALPH3*LS
  ALPH(1,7)=LD**3/3./AES/IU+ALPH1+ALPH2*LD+(ALPH2+ALPH3*LD)
1*LD+LH*(LD**2/2./AES/IU+ALPH2+ALPH3*LD)
  ALPH(2,2)=ALPH6+ALPH3
  ALPH(2,3)=ALPH(1,2)
  ALPH(2,4)=ALPH(2,2)
  ALPH(2,5)=ALPH2
  ALPH(2,6)=ALPH3
  ALPH(2,7)=(LD**2/2./AES/IU+ALPH2+ALPH3*LD)
  ALPH(3,3)=ALPH(1,1)
  ALPH(3,4)=ALPH(1,2)
  ALPH(3,5)=ALPH(1,5)
  ALPH(3,6)=ALPH(1,6)
  ALPH(3,7)=ALPH(1,7)
  ALPH(4,4)=ALPH(2,2)
  ALPH(4,5)=ALPH(2,5)
  ALPH(4,6)=ALPH(2,6)
  ALPH(4,7)=ALPH(2,7)
  ALPH(5,5)=ALPH1
  ALPH(5,6)=ALPH(2,5)
  ALPH(5,7)=ALPH1+ALPH2*LD
  ALPH(6,6)=ALPH(2,6)
  ALPH(6,7)=ALPH2+ALPH3*LD
  ALPH(7,7)=LD**3/3./AES/IU+ALPH1+ALPH2*LD+(ALPH2+ALPH3*LD)*LC
  ALPH(1,8)=ALPH2+LD**2/2./AES/IU+(ALPH3+LD/AES/IU)*LH
  ALPH(2,8)=ALPH3+LD/AES/IU
  ALPH(3,8)=ALPH(1,8)
  ALPH(4,8)=ALPH(2,8)
  ALPH(5,8)=ALPH2
  ALPH(6,8)=ALPH3
  ALPH(7,8)=ALPH2+LD**2/2./AES/IU
  ALPH(8,8)=ALPH3+LD/AES/IU
  DO 30 I=2,8
  K=I-1
  DO 30 J=1,K
30 ALPH(I,J)=ALPH(J,I)
  RETURN

```



```

END
SUBROUTINE KBAND(AKBP,AKBCP,RAD,IDAMP)
C.....IDAMP=0.....INTERNAL DAMPING IS NOT INCLUDED
C.....IDAMP=1.....INTERNAL DAMPING IS INCLUDED
IMPLICIT REAL*8(A-H,C-Z)
COMPLEX*16 CDSQRT,CDEXP,DCMPLX
COMPLEX*16 AEBAND,DI,UO,UO0,FBCPRI,P,AK,AKL,AKB,AKA,AKAL,G,AM
COMPLEX*16 HYSIN,HYCCS,AKBP,AKBCP
REAL*8 LBAND

C
C      2.66 IS THE BAND ANGLE
C
PHWAVE=2.66*3.141592654/180.
DATA RORIM,ARIM,RRIM,ERIM/1.399D-4,5.596D0,8.633D0,18.06/

C
C      TENSIO IS THE BAND INITIAL WINDING TENSION
C
TENSIO=360.00
C.....NB=# OF BAND SETS
NB=12
T0=360./NB/2.*3.141592654/180.
DATA RH,RI/2.25D0,7.625D0/
LBAND=(RI-RH)/DCOS(PHWAVE)

C
C      BB,TB ARE BAND WIDTH AND THICKNESS RESPECTIVELY
C      RCBAND, EBAND ARE BAND MATERIAL DENSITY AND YOUNG'S MODULUS
C
DATA EB,TB,RCBAND,EBAND/0.5D0,0.1D0,1.295D-4,11.06/

C
C      GABAND= BAND LESS TANGENT
C
DATA GABAND/0.0172D0/
ABAND=BB*TB
AIIP=T0*BB**3/12.
AICP=TB**3*EB/12.
IF(IDAMP.EQ.0) GO TO 1
EIBAND=-GABAND*EBAND
AEBAND=DCMPLX(EBAND,EIBAND)
GO TO 2
1 AEBAND=EBAND
2 UO0=RCBAND*RAD**2/AEBAND*(RI**3/3-RI**2*RH/2.+RH**3/6.)
UP=RAD**2*(RORIM*ARIM*RRIM**2*DTAN(T0)+RCBAND*ABAND*DCOS(PHWAVE)
1**3*(RI**3/3.-RI**2*RH/2.+RH**3/6.)/2./LBAND)
DR=ARIM*ERIM/RRIM*DTAN(T0)
DI=ABAND*EBAND/2./LBAND*DCOS(PHWAVE)**2
UO=UP/(DR+DI)
FBCPRI=ABAND*AEBAND/LBAND*(UO-UO0*DCOS(PHWAVE))*DCOS(PHWAVE)
FBC=RCBAND*ABAND*RAD**2*(2.*RI**3-3.*RI**2*RH+RH**3)/6./((RI-RH)
P=TENSIO+FEC+FBCPRI
AK=CDSQRT(P/AEBAND/AIIP)

```



```
AKL=AK*LBAND
HYSIN=(CDEXP(AKL)-CDEXP(-AKL))/2.
HYCOS=(CDEXP(AKL)+CDEXP(-AKL))/2.
AKB=AK*P*HYSIN/(2.*(1.-HYCOS)+AKL*HYSIN)
AKBIP=12.*(ABAND*AEBAND/LBAND*DCOS(PHWAWE)**2+AKB)
AKA=CDSQRT(P/AEBAND/AICP)
AKAL=AKA*LBAND
HYSIN=(CDEXP(AKAL)-CDEXP(-AKAL))/2.
HYCOS=(CDEXP(AKAL)+CDEXP(-AKAL))/2.
RP=R*(DCOS(PHWAWE)-1.5*DSIN(PHWAWE))
G=(HYCOS-HYSIN/AKAL)*LBAND+(1.-HYCOS)*RP
AM=AEBAND*AICP*AKA**2*G/(2.*(HYCOS-1.)-AKAL*HYSIN)
AKB=2.*ABAND*AEBAND*1.5*(1.5*DCOS(PHWAWE)+R*(DSIN(PHWAWE)))/LBAND
1+2.*AM
AKBCP=6.*AKE
RETURN
END
```